Emergence of Riemannian manifolds from graphs and aspects of Chern-Simons theory

by

Si Chen

B.Sc., Peking University, 2006

A THESIS SUBMITTED IN PARTIAL FULFILLMENT OF
THE REQUIREMENTS FOR THE DEGREE OF

DOCTOR OF PHILOSOPHY

in

The Faculty of Graduate and Postdoctoral Studies

(Physics)

THE UNIVERSITY OF BRITISH COLUMBIA

(Vancouver)

August 2013

© Si Chen 2013

Abstract

This thesis is divided into three chapters. Chapter 1 is a study of statistical models of graphs, in order to explore possible realizations of emergent manifolds. Graphs with given numbers of vertices and edges are considered, governed by a Hamiltonian that favors graphs with near-constant valency and local rotational symmetry. The model is simulated numerically in the canonical ensemble. It is found that the model exhibits a first-order phase transition,and that the low energy states are almost triangulations of two dimensional manifolds. The resulting manifold shows topological "handles" and surface intersections in a higher embedding space as well as non-trivial fractal dimension. The model exhibits a phase transition temperature of zero in the bulk limit. We explore the effects of adding long-range interactions to the model, which restore a finite transition temperature in the bulk limit.

In Chapter 2, aspects of Chern-Simons theory are studied. The relations between Chern-Simons theory, a model known as BF theory named after the fields that appear in the actions, and 3D gravity, are explored and generalized to the case of non-orientable spacetime manifolds. U(1) Chern-Simons theory is quantized canonically on orientable manifolds, and U(1) BF theory is similarly quantized on non-orientable manifolds. By requiring the quantum states to form a representation of the deformed holonomy group and the deformed large gauge transformation group, we find that the mapping class group of the spacetime manifold can be consistently represented, provided the prefactor k of the Chern-Simon action satisfies quantization conditions which in general are non-trivial. We also find a $k \leftrightarrow 1/k$ duality for the representations.

Motivated by open questions about interpreting the finite size results from Chapter 1,

models of finite size scaling for systems with a first-order phase transition are discussed in Chapter 3. Three physics models — the Potts model, the Gō model for protein folding, and the graph model in Chapter 1 — are simulated. Several finite size scaling models, including three functional forms to fit the energy distributions, and a capillarity model, are compared with simulations of the corresponding physics models.

Preface

A version of Chapter 2 has been published in S. Chen and S. S. Plotkin, *Phys. Rev.* **D87** (2013) 084011, `arXiv:1210.3372 [gr-qc]` [1]. The model was constructed by my supervisor Dr. Steven S. Plotkin and me together, the simulation was performed by me, and the result analysis and interpretation were conducted by Dr. S. S. Plotkin and me in collaboration.

A version of Section 2.5 has been published in S. Chen, *Mod. Phys. Lett.* **A27** (2012) 1250087, `arXiv:1103.2820 [hep-th]` [2]. All the related work was carried out by me, in consultation with Dr. Gordon Semenoff, Dr. Donald Witt and Dr. Kristin Schleich.

A manuscript in preparation contains material from Section 2.3 and Section 2.6. Another manuscript containing material from Chapter 3 is also in preparation.

The material contained in this thesis is the result of two studentships. From September 2007 to August 2011, S. Chen was supervised by Dr. G. Semenoff, Dr. D. Witt and Dr. K. Schleich. In 2011, S. Chen switched supervisors to Dr. S. S. Plotkin.

Table of Contents

List of Figures

List of Symbols

Frequently used symbols in Chapter 2 are listed as follows:

Symbol	**Standing for**	**First appearance**
$\wedge$	wedge product operator	eq.(2.1)
$\otimes$	tensor product	eq.(2.11)
A	one-form field	eq.(2.1)
B	one-form density field	eq.(2.15)
Diff(M)	diffeomorphism group of M	p.68
d	exterior derivative	eq.(2.1)
$e_{\mu}^{\ a}$	local frame of a Riemannian manifold	eq.(2.19)
F	$F = dA + A \wedge A$, curvature of a connection A	eq.(2.2)
f^*	pullback of f	p.57
G	depending on the context, Lie group, or	eq.(2.3)
	gravitational constant	eq.(2.7)
$\mathfrak{g}$	Lie algebra	eq.(2.1)
g	depending on the context, Lie group valued field, or	eq.(2.3)
	genus of a surface	p.68
$g^{\mu\nu}$	metric tensor	eq.(2.2)
H^p	de Rham cohomology group of degree p	eq.(2.12)
I_d	identity matrix of degree d	eq.(2.60)
$J_{\alpha\beta}$	Jacobian of transition function	p.58
k	coupling constant in CST and in BF theory	p.72

Symbol	**Standing for**	**First appearance**
$[M]$	orientation on the manifold M	p.57
$\tilde{M}$	orientable double cover of M	p.58
∂M	boundary of M	eq.(2.4)
N_g	non-orientable surface whose orientable double cover is Σ_g	p.92
O	orientation bundle	p.58
p	numerator of k	p.72
q	denominator of k	p.72
$\mathfrak{sl}(2,\mathbb{R})$	Lie algebra of the special linear group of degree 2 on $\mathbb{R}$	p.65
$\mathrm{SL}(2,\mathbb{Z})$	special linear group of degree 2 on $\mathbb{Z}$	p.76
$\mathrm{U}(1)$	unitary group of degree 1	p.ii
$\mathrm{u}(1)$	Lie algebra of U(1)	p.93
$\mathbb{Z}_2$	multiplicative group composed of 1 and -1	p.58
Δ	0 or 1 depending on the parities of p and q	eq.(2.51)
Λ	cosmological constant	eq.(2.7)
π_1	fundamental group	eq.(2.6)
Σ	compact two-dimensional manifold without boundary	p.54
Σ_g	orientable surface of genus g	p.68
σ	an involution defined on an orientable double cover	p.59
Ω^p	bundle of smooth p-forms	p.58
ω	$\exp\left(\frac{\mathrm{i}2\pi}{k}\right)$	p.77
$\omega_{\mu\ b}^{\ a}$	spin connection of a Riemannian manifold	eq.(2.20)

The notation conventions employed in Section 2.5 and Section 2.6 are listed as follows:

Notation	**Standing for**
$A, B, \ldots$	u(1)-valued fields, or closed curves corresponding to MCG generators
$a, b, \ldots$	U(1)-valued numbers
$\bar{\alpha}, \bar{\beta}, \ldots$	closed curves corresponding to homotopy group generators
$\alpha, \beta, \ldots$	homotopy group generators
$\rho, \sigma, \ldots$	LGT group generators
$\tilde{\alpha}, \tilde{\beta}, \ldots$	irreducible blocks of homotopy group generators
$\mathsf{A}, \mathsf{B}, \mathsf{Y}, \ldots$	MCG generators
$\tilde{\mathsf{A}}, \tilde{\mathsf{B}}, \ldots$	irreducible blocks of MCG generators
i, j, k	indices within an irreducible block
m, n	indices of irreducible blocks

List of Abbreviations

The following abbreviations are used in this thesis:

Abbreviation	**Complete phrase**	**First appearance**
WHAM	weighted histogram analysis method	p.19
CST	Chern-Simons theory	p.50
MCG	mapping class group	p.51
LGT	large group transformation	p.72
FSS	finite size scaling	p.99

Acknowledgements

First and foremost, I would like to thank my supervisor Dr. Steven S. Plotkin, for his constant guidance and support, ever since I joined his research group. I am grateful to my PhD committee members Dr. Mark Van Raamsdonk, Dr. Moshe Rozali and Dr. Colin Gay, for their helpful suggestions in and after the committee meetings, and their support when I was going through the process of changing supervisor.

I wish to thank other group members in the Plotkin Group. Eric Mills, Ali R. Mohazab and Atanu Das have raised interesting questions, and offered insights about my projects. Atanu Das also helped me with the numerical work involved in the protein folding model.

Finally, I like to thank the professors of the courses that I have taken and learned so much from, and thank my officemates for all the enjoyable discussions throughout the years.

Chapter 1

Statistical mechanics of graph models and their implications for emergent manifolds

1.1 Introduction

Since the first systematic studies of random graph models by Erdős and Rényi [3], the relation between graph theory models and physics models, in particular statistical physics models, has attracted much interest. Concepts and tools in graph theory have been applied to problems in physics, computer science, and biology to produce remarkable results. For example, Feynman diagrams that are planar have special roles in the large N QCD model [4]; in causal dynamical triangulation, four-dimensional triangulated manifolds with fixed edge lengths, which can be viewed as a class of graphs, are used to construct spacetime on the Planck scale to regularize the quantum gravitational path integral [5, 6]; statistical mechanical models of network growth can explain the connectivity of systems such as the Internet [7]; structures of amorphous solids can be quantified using graph theory properties [8]; intracellular signalling networks can exhibit emergent behavior stored within biochemical reactions, including integration of signals across multiple time scales and self-sustaining feedback loops [9]; neural networks can collectively and robustly produce content-addressable memories from partial cues [10], indicating capacity for generalization, familiarity recognition, and categorization. Added to these discoveries, a new collection of

graph models has been proposed as candidates for emergent spacetime, as described below.

A manifold can be approximated by a triangulation, which in turn can be viewed as a graph filled with simplices. From this observation, one can consider how a graph may give rise to a manifold; i.e. from a family of graphs, following some constraints and obeying some set of rules for dynamical processes, is it possible that a manifold-like structure can emerge? To be more precise, consider the possibility that a graph G gives rise to a smooth manifold M. A vertex in G corresponds to a point in M; when a pair of vertices in G are connected by an edge, the corresponding pair of points in M have a certain distance ϵ. When the length scale under consideration is much larger than ϵ, G resembles the smooth manifold M. In such cases, one can say that the manifold M, including its dimensionality, topology, and metric, emerges from the graph G in the continuous limit.

From this general idea, in references [11, 12], a graph model was constructed from a given graph Hamiltonian, where it was proposed that the low-energy phase of the model may be interpreted as an emergent spacetime. In addition, it was found that when the edges of the graph possess a spin degree of freedom, the model could give rise to a U(1) gauge theory [12]. In [13], Konopka has analytically and numerically studied the above graph model as a statistical model. A phase transition was found, where it was argued that the low-temperature phase can be related to spacetime only if the graph can interact with some matter degrees of freedom. In [14, 15], a related model, which in addition to graphs corresponding to spacetimes, also incorporates a matter field that resides on the vertices, was proposed to study the role of matter in the emergence of spacetime from graphs. In [16], Conrady has constructed a Hamiltonian favoring low-temperature, two-dimensional manifolds through terms that explicitly favor two-dimensional triangulations; for example, each vertex is favored to have 6 edges as in a triangular lattice, and tetrahedra are penalized. The model was simulated for small system sizes ($N \leq 180$ edges), which showed a heat capacity peak, and a transition temperature that decreased with system size.

In this chapter, we also investigate a statistical model of graphs, in that the objects under consideration are merely abstract graphs, without any information on the positions

of the vertices, or the lengths of the edges. A graph can randomly transform into another graph according to a set of transformation rules. Graphs with given numbers of vertices and edges are considered, and they are governed by a Hamiltonian that favors graphs with a set of local symmetries. If these local symmetries are preserved, the resulting graphs should be nearly triangulations of manifolds with a certain dimensionality, where the dimensionality is controlled by the ratio of vertices to edges. We are interested in whether any global structure of the graphs arises as a consequence.

Because every edge in this model corresponds to a positive length ϵ, only real positive distances can arise, so this model can only be used to describe Riemannian manifolds (i.e., with positive definite metric). The metric of a Riemannian manifold can be alternatively viewed as a distance function between any pair of points, which satisfies the triangle inequality. On a graph, there is also a natural notion of distance, namely the length of the shortest path between a pair of vertices. This distance is also positive-definite and satisfies the triangle inequality. Thus on any graph, there is a well-defined distance function, as well as a corresponding geodesic. Graph geodesics between two vertices are often highly degenerate, however, unlike the case for manifolds. If a manifold is to emerge from a graph, one expects that in the continuous limit all degenerate geodesics are close by, and the differences of their paths are only of order ϵ. After establishing this distance function between vertices, mapping the graph to a Riemannian manifold is still a non-trivial problem. If we enforce that every edge is identical in that they have the same length when mapped to the Riemannian manifold, then only for certain graph configurations will a Riemannian manifold emerge from the graph. Otherwise the system will be frustrated and unable to meet the condition of constant edge length, without increasing the dimension above that of the manifold that would emerge from the graph.

In this chapter, after reviewing the relevant graph theory preliminaries, we introduce a graph Hamiltonian based only upon local symmetries. We evolve the graph under the Monte Carlo rules obeying statistical mechanical equilibrium, and we investigate whether a low-temperature manifold state emerges. We investigate the sharpness of the phase transi-

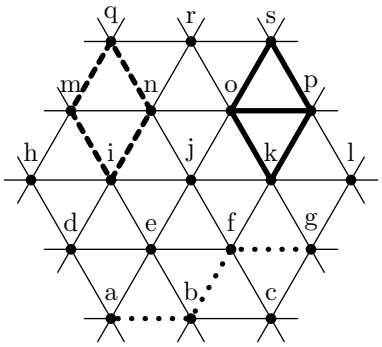

Figure 1.1: Examples for the graph theory concepts.

tion using energy as an order parameter for different size systems, and we discuss the likely first-order nature of the transition. We construct heat capacity curves as a function of temperature and investigate the transition temperature as a function of system size, which points toward a zero-temperature phase transition in the bulk limit. The Haussdorf dimensionality of the emergent manifold is investigated and found to be an increasing function of system size, and approximately 3 for the largest system sizes we investigated (2000 vertices). Correlation functions between defect-carrying vertices and edges are investigated to determine whether the effective potential between defects is attractive or repulsive. Finally, we argue in analogy to condensed-matter systems that a nonzero phase transition temperature requires long-range interactions, and shows that a Coulombic-like term between graph vertices yields an apparently finite-phase transition temperature, but with a highly ramified manifold.

1.2 Graph theory preliminaries

Before motivating for details of the model, we shall remind the reader about some graph theory concepts, which will be needed later in constructing the model.

A **graph** G is composed of a set of vertices $V(G)$ and a set of edges $E(G)$, where every edge is a subset of $V(G)$ with two elements. Note that by this definition, the two vertices in an edge set cannot be the same vertex, and two edges cannot connect the same two

vertices. Such graphs are sometimes called "simple graphs," as opposed to "multigraphs." Because we will only consider graphs of this definition, they will be simply referred to as "graphs."

A vertex v is **incident** with an edge e if $v \in e$. We denote an edge e by its vertices, or **ends**, say u and v, as $e = \{u, v\}$, or simply $e = uv$. A vertex u is a **neighbor** of, or is **adjacent** to, a vertex v if uv is an edge. The **valency** or **degree** of a vertex is the number of edges incident to that vertex.

A graph in which every vertex has the same valency is **regular**. It is k-regular if every vertex has valency k.

A graph in which every pair of vertices is connected by an edge is **complete**. It is denoted by K_n if it has n vertices.

G' is a **subgraph** of a graph G, if G' itself is a graph, $V(G') \subseteq V(G)$ and $E(G') \subseteq E(G)$, and this is denoted by $G' \subseteq G$.

If $U \subseteq V(G)$, the subgraph G' **induced** by U is the graph for which $V(G') = U$, and $E(G')$ contains an edge xy if and only if $x, y \in U$ and $xy \in E(G)$. This is denoted by $G' = G[U]$, and G' is called an **induced subgraph** of G. (For example, in Figure 1.1, the vertices k, o, p, s, and the five thick edges, compose an induced subgraph; the vertices i, m, n, q, and the four thick dotted edges, compose a subgraph, but not an induced subgraph.) In particular, in a graph G, the subgraph induced by the set of neighbors of a vertex v is called the **neighborhood** of v, and is denoted by $G_N(v)$.

A **path** is an alternating sequence of vertices and edges, beginning with a vertex and ending with a vertex, where each vertex is incident to both the edge that precedes it and the edge that follows it in the sequence, and where the vertices that precede and follow an edge are the end vertices of that edge. The **length** of a path is the number of edges in the path. (For example, in Figure 1.1, (a, ab, b, bf, f, fg, g) is a path with length 3, in which the edges are denoted by dotted lines, and is also one of several paths between a and g having the minimal distance.) The **distance** between two vertices is the length of shortest path between them. In a graph G, the distance between vertices u, v is denoted by $d_G(u, v)$.

A graph is **connected** if any two vertices are linked by a path.

The **eccentricity** $\epsilon_G(v)$ of a vertex v in a graph G is the maximum distance from v to any other vertex, i.e.,

$$\epsilon_G(v) = \max_{u \in V(G)} d_G(v, u),$$

where $d_G(v, u)$ is the distance between v and u in the graph G.

The **diameter** $\mathrm{diam}(G)$ of a graph G is the maximum eccentricity over all vertices in a graph, and the **radius** $\mathrm{rad}(G)$ is the minimum,

$$\mathrm{diam}(G) = \max_{v \in V(G)} \epsilon_G(v), \quad \mathrm{rad}(G) = \min_{v \in V(G)} \epsilon_G(v).$$

When G is not connected, $\mathrm{diam}(G)$ and $\mathrm{rad}(G)$ are defined to be infinite. Some examples of neighborhood subgraphs are shown in Figure 1.2. For every vertex in Figure 1.1, the neighborhood subgraph is Figure 1.2(a); for every vertex in Figure 1.4, the neighborhood subgraph is Figure 1.2(f). Figures 1.2(b)-1.2(e) are examples of neighborhood subgraphs that appear commonly in the simulation.

Given a lattice, the corresponding **lattice graph** is the graph whose vertices are the points in the lattice, and whose edges are the pairs of nearest points in the lattice. (For example, the whole graph in Figure 1.1 is an equilateral triangular lattice graph.)

1.3 The model

To gain intuition on the form of constraints and Hamiltonians that may induce manifolds, let us construct some graphs resembling some manifolds, starting with the example of a flat two-dimensional plane $\mathbb{R}^2$. Intuitively, any two-dimensional lattice graph as defined above forms a "two-dimensional" manifold, and a coordinate system of the manifold naturally inherits from the coordinates of the lattice graph. This is directly analogous to a Bravais lattice in crystallography. *A priori* there seems no decisive reason to choose any particular Bravais lattice as the preferred graph configuration; however, we shall choose the equilateral triangular lattice graph (Figure 1.1), using the following argument. On $\mathbb{R}^2$, for any point p and any distance δ, let $B_\delta(p)$ denote the geodesic ball centered at p with radius

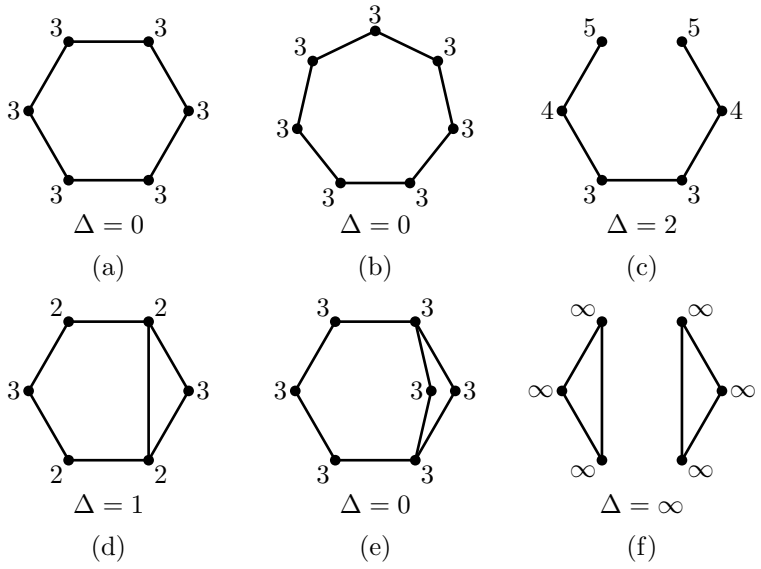

Figure 1.2: Some examples of neighborhood subgraphs. The eccentricity is labeled for each vertex, and the difference of diameter and radius of these subgraphs, which is denoted by Δ, is labeled below each graph. (a) is the neighborhood subgraph of vertices in the triangular lattice graph (Figure 1.1); (b), (c), (d) and (e) appear commonly in simulations, as parts of the defects; (f) is the neighborhood subgraph of vertices in the graph in Figure 1.4.

δ, and $B_\delta(p) - p$ has the topology of a circle S^1. For graphs, we can define the notion of "geodesic ball" similarly with that in Riemannian geometry. Let $B_n(v)$ be the set of the vertices that have distance from vertex v no greater than n, including v itself. For any two-dimensional lattice, if we denote the corresponding graph by G, for sufficiently large n, the induced subgraph $G[B_n(v) - v]$ also looks like S^1 topologically. However, for $n = 1$, namely the neighborhood subgraph $G_N(v) = G[B_1(v) - v]$, this property is no longer true for all lattices. For example, on the square lattice, $G_N(v)$ is composed of 4 disconnected vertices. Only for the equilateral triangular lattice, $G_N(v)$ looks topologically like S^1. Thus in this sense, the equilateral triangular lattice graph is the closest analog to $\mathbb{R}^2$ among all the two-dimensional lattice graphs, on all distance scales down to ϵ.

A graph can form a two-dimensional lattice for the correct ratio of edges to vertices. While a thermalized lattice in two dimensions is isotropic [17–19], the connectivity of such a lattice is still well-defined at low temperature. We thus choose to add defects in the form of extra edges or bonds, which will evolve under some Hamiltonian. This allows bonded vertices to be permuted, so that the low-temperature phase is still a "quasi-fluid" that retains a symmetry corresponding to randomized graph connectivities. The extra edges induce defects in the lattice, which may be mobile. The exact shape of the defects and the reason why the defects are unstable or meta-stable depend sensitively on the Hamiltonian. We shall construct a candidate Hamiltonian, and test the stability of the defects by numerical simulation. This construction generalizes to $\mathbb{R}^n$ straightforwardly: We can see that the defect-free lattice is the n-dimensional lattice as arising from a regular tiling of n-dimensional tetrahedra. The defect is a $(n-1)$-dimensional "foam" that divides the space into many patches of lattices with random orientations.

We seek the simplest Hamiltonian that can give rise to manifold-like triangulation graphs as classical solutions, which contain defects that facilitate graph permutation symmetry. We assume that the action is local, in the sense that it should be a sum over the vertices and/or edges, such that each term involves a finite number of vertices and/or edges within some cutoff distance. This condition is imposed because almost all physics models for which

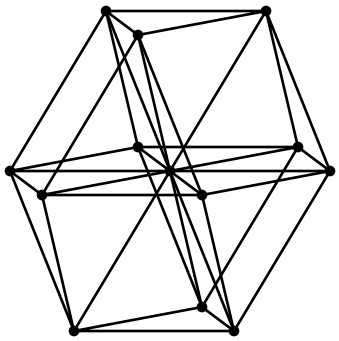

Figure 1.3: A neighborhood in the face-centered cubic lattice graph. This is the subgraph generated by a vertex in the lattice and all its neighbors.

the Hamiltonian or Lagrangian is an integral of the corresponding density are local in the same sense.

A defect manifests itself as a local structure containing vertices with anomalous valency. One obvious local property of manifold-like graphs is that all vertices not in any defects would have the same valency. Moreover it is likely that vertices in the defects have just one more or one less neighbor. These properties can be enforced by a Hamiltonian quadratic in the valency:

$$H_1 = c_1 \sum_{v \in V(G)} n_v^2, \tag{1.1}$$

where n_v is the valency of vertex v, and c_1 is a positive constant (which will be taken to be infinite as described below). The average valency of the vertices is given by

$$\alpha = \frac{2N_E}{N_V} \tag{1.2}$$

where N_E is the total number of edges and N_V the total number of vertices. Note that, for example, $\alpha = 6$ is compatible with a regular equilateral triangular lattice, which in turn implies that the emergent manifold is two dimensional, while $\alpha = 12$ is compatible with the face-centered cubic lattice (see Figure 1.3), which implies a three-dimensional emergent manifold. Thus without changing the form of the Hamiltonian, we should be able to find manifolds with different dimensionalities by adopting different *a priori* values of α. In the simulations described below, we choose α to be a non-integer, so that there exists an

"excess" number of edges, which contribute to the presence of defects. Because the total number of vertices and edges are fixed, the term in (1.1) is minimized when every vertex has valency either $\lfloor \alpha \rfloor$ or $\lceil \alpha \rceil$. In our simulations, c_1 is taken to be infinite and so is no longer an adjustable parameter of the model, and the corresponding term in (1.1) is enforced to be minimal.

To obtain manifold-like solutions consisting of patches of close-packed lattices interspersed with defects, it is not sufficient to impose only the condition that each vertex has approximately the same number of neighbors. Many regular graphs do not look like any manifold at all (see, for example, Figure 1.4). Additional terms in the Hamiltonian are thus required for manifold-like solutions.

One candidate for such a term consists of particular subgraphs that can be embedded into the graph. From this viewpoint, n_v is the number of K_2 subgraphs (two vertices connected by an edge) that go through the vertex v. It is likely however that choosing more terms of this type will affect the dimensionality of the resulting spacetime. For example, if we incorporate terms that favor more K_3 subgraphs (triangles) and fewer K_4 subgraphs (tetrahedra), then it can be expected that these terms would favor two-dimensional manifolds [16]. As we hope to find a model that does not select the dimensionality at the level of the Hamiltonian, we will not use any other term of this type besides H_1.

Another property of manifold-like graphs is that around most vertices, the graph has a local discrete rotational symmetry that reflects the local isotropy of the emergent manifold. This can be restated as for each vertex v, the subgraphs $G[B_n(v) - v]$ for most v should have a discrete rotational symmetry. To reduce the number of possible Hamiltonian terms, we impose this condition only on $G[B_1(v) - v]$, which is also $G_N(v)$. We introduce the term

$$H_2 = c_2 \sum_{v \in V(G)} \Delta(v), \tag{1.3}$$

where c_2 is a positive constant, and

$$\Delta(v) = \mathrm{diam}(G_N(v)) - \mathrm{rad}(G_N(v)), \tag{1.4}$$

in which $\mathrm{diam}(G_N(v))$ is the diameter of the subgraph $G_N(v)$, and $\mathrm{rad}(G_N(v))$ is the

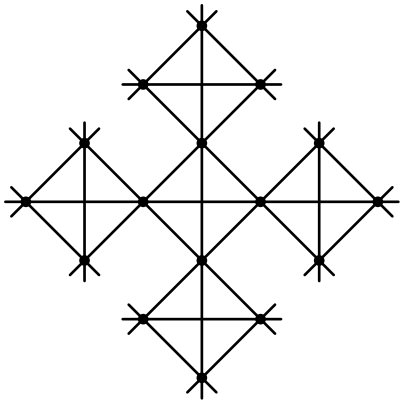

Figure 1.4: A 6-regular graph that is not similar to any manifold. This graph can be viewed as an infinite rooted "tree" graph, in which each node has three children (except the root node has four children), and every node of the "tree" is actually a tetrahedron.

radius of the subgraph $G_N(v)$. By the definitions of diameter and radius of graphs, if the subgraph $G_N(v)$ is not connected, they are both infinite. Here, we additionally define that their difference $\mathrm{diam}(G_N(v)) - \mathrm{rad}(G_N(v))$ is also infinite when $G_N(v)$ is not connected. The term H_2 then enforces that all neighborhood subgraphs are always connected. When $G_N(v)$ is connected, the difference between its diameter and its radius is a measure of its asymmetry. Figure 1.2 shows several examples of neighborhood subgraphs. The eccentricity of every vertex in the subgraphs is labeled, along with the value of $\Delta(v)$ for each subgraph. For Figures 1.2(a) and (b), the $G_N(v)$'s have a rotation symmetry of $\mathbb{D}_6$ and $\mathbb{D}_7$, respectively, while Figures 1.2(c)-(e) are not rotationally symmetric.

In two dimensions, a graph forms a triangulation of a surface if and only if all the neighborhood subgraphs are cycles [20]. When the degrees of the subgraphs are either 6 or 7, which is imposed by the H_1 term, one can see from the examples in Figure 1.2 that the H_2 term indeed favors cyclic neighborhood subgraphs, with only one exception shown in Figure 1.2(e). We thus expect that, in this model, a graph with low energy is almost a triangulation of a surface.

Because metrics in General Relativity are covariant, the coordinates of a spacetime point have no absolute meaning. Analogously, in the graph model, the labeling of vertices should

also be irrelevant, and isomorphic configurations with different labeling should be considered the same. The numerical implementation of the graph model described in the next section contains a labeling of vertices. The relation between labeled graphs and unlabeled graphs is the following. Given an unlabeled graph, there are $N_V!$ ways to label it. However, if this unlabeled graph has some symmetry, some of the labeled graphs can still be isomorphic when the labels are considered. For example, consider the line graph with three vertices. The labeled graph 1-2-3 is different from the labeled graph 1-3-2, but it is still isomorphic to the labeled graph 3-2-1: Due to the two-fold reflection symmetry of the line graph, graphs 1-2-3 and 3-2-1 have the same edge-set. Thus for a given labeled graph G, its contribution to the partition function should be re-weighted by the factor $S(G)/N_V!$, where $S(G)$ is the symmetry factor of the unlabeled graph corresponding to G. (For the line graph with three vertices, $S(G) = 2$ for configurations 1-2-3 and 3-2-1.) The factor $N_V!$ can be ignored because it is the same for all samples in a simulation, while the factor $S(G)$ depends on the graph G, and could in principle be calculated. However, calculating $S(G)$ is a computationally difficult problem. We choose to ignore this factor in the numerical simulations, and expect to find qualitatively the same result as the more realistic model with unlabeled vertices. A systematic calculation of $S(G)$ is an interesting topic for future work.

Thus we propose the following model: Consider a simple graph with N_V vertices and N_E edges. The vertices are labeled, while the edges are not labeled. The Hamiltonian is composed of two terms, as motivated previously:

$$H = H_1 + H_2. \tag{1.5}$$

Because the Hamiltonian is prohibitive to analytical solution, we implement a numerical simulation, as described in the next section, to study the equilibrium states of this model in the canonical ensemble, i.e. at a given temperature. In particular, we will be interested in the structures of the states with low energies, and the nature of the phase transition, if one exists, to these low-energy states.

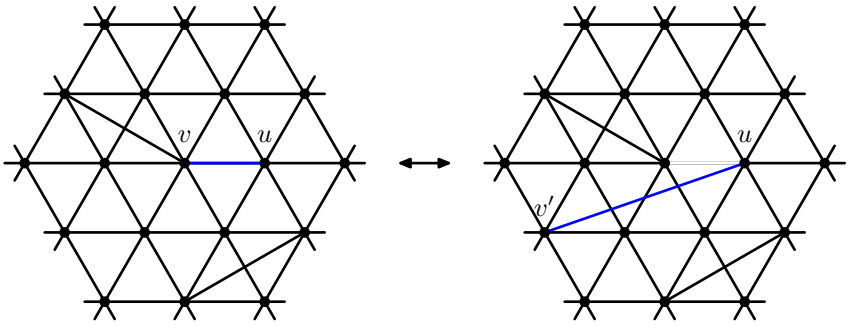

Figure 1.5: An example of the Monte Carlo trial moves. The blue edge can from uv to uv' or *vice versa* in a trial move.

1.4 Numerical simulation

We sample equilibrium states in the model using a Monte Carlo simulation [21]. The parameter α defined in (1.2) as giving the mean number of edges per vertex is taken to be slightly larger than 6, which we expect will induce two-dimensional structures dictated by triangulations as described above. There is no fixed boundary on the graphs. The size of the graphs is specified by the number of vertices N_V, and the number of edges N_E. For convenience, in the following we use N_V and the number of extra edges $X \equiv N_E - 3N_V$, to specify the size of the graphs. Given the graph size, the initial configuration is taken to be a randomly generated, connected graph.

The graph is evolved in the canonical ensemble with temperature $1/\beta$. In each Monte Carlo step, one end of an edge can jump from one vertex to another. We randomly pick an edge, and randomly label its ends by u and v. To find the new location of the edge uv, we perform a random walk starting from v as the origin, which does not pass through the edge uv (this condition guarantees that a connected graph remains connected after such a move). The number of steps ℓ of the walk is a random positive integer chosen from the probability distribution $P(\ell) = \gamma^{\ell-1} - \gamma^{\ell}$, where γ is a parameter between 0 and 1 (we take $\gamma = 0.5$ below). Denote the ending vertex of the random walk as v'. The edge is then moved from uv to uv'. See Figure 1.5 for a schematic example of possible Monte Carlo trial moves. If the new graph is still simple, its energy is compared with that of the old graph, and this move

is accepted or rejected according to the Metropolis algorithm [21]. See Appendix 1.8 for the algorithm used in calculating the radius and diameter of the neighborhood subgraphs. Each "sweep" through the system contains N_E Monte Carlo steps, so on average each edge has one chance to jump in one sweep. Such a method is ergodic; moreover with this jumping scheme, the energy of only a few vertices is affected after each Monte Carlo step, and the energy of only these vertices needs to be updated.

Simulations are performed with $c_1 = \infty$, $c_2 = 1.0$, $\gamma = 0.5$, and various values of N_V, X and β. Before showing the thermodynamics results from the simulations, let us first describe the method that we used to render a graph from the simulations, in order to interpret its evolution.

1.4.1 Rendering graphs

To render a graph such that its structure can be best visualized, we need to devise an appropriate drawing scheme. A drawing of a graph maps vertices to points in $\mathbb{R}^n$ with line segments connecting adjacent points. The following method is used to generate drawings in $\mathbb{R}^3$. For any drawing of a graph G, we seek to minimize the function

$$H_{\text{draw}} = \sum_{e \in E(G)} \left(a_1 l_e^2 + \frac{a_2}{l_e^2} \right) + \sum_{\substack{i,j \in V(G),\ i \neq j, \\ i,j \text{ not adjacent}}} \frac{a_3}{l_{ij}^2}, \tag{1.6}$$

where l_e is the length of the drawing of edge e, l_{ij} is the distance of the drawing between vertices i, j, and $a_1 = 1.0, a_2 = 1.0, a_3 = 5.0$. The first term gives a preferred length for every edge, and the second term gives a repelling force to every non-adjacent pair of vertices. The function H_{draw} is chosen this way in order to make every edge have approximately the same length in the drawing, and as well, to make the drawing as expanded as possible. In practice, even for moderate-sized graphs, H_{draw} has numerous local minima and is difficult to minimize. We thus use another Monte Carlo calculation to search for its near-optimal values. Initially, all the vertices are located at the origin of $\mathbb{R}^3$. In each Monte Carlo step, a randomly-chosen vertex is randomly moved to another position within the ball of radius $\delta = 2.5$, centered at the original position, and the new position has uniform

probability distribution within the ball. After the Monte Carlo calculation, because the low-temperature configurations in the model are conjectured to be similar to triangulations of surfaces, we also search for all the K_3 subgraphs (triangles) in the graph, and render (flat, solid) triangles to fill the interior of the K_3's.

Figure 1.6 shows some snapshots taken from the simulations. Figures 1.6(a)-(c) are for the system of size $N_V = 200$ and $X = 20$. Figure 1.6(a) shows the initial configuration, 1.6(b) shows a typical configuration at high temperature ($\beta = 1.0$), and 1.6(c) shows a typical configuration at low temperature ($\beta = 2.0$). Figure 1.6(d) is for the system of size $N_V = 1000$ and $X = 100$, and it is a typical configuration at low temperature ($\beta = 2.0$).

In the sample drawings in Figure 1.6, different colors are used to denote different types of vertices. The color-code is as follows:

	Degree= 6	Degree= 7
Zero contribution to H_2	black	green
Nonzero contribution to H_2	red	blue

Also, yellow lines are drawn at places where two triangles intersect, i.e., this identifies where the triangulated surface intersects with itself.

1.4.2 Topology of the manifold in the presence of defects

For the low-temperature graphs, several examples of common local defects are shown in Figure 1.7. They are called local in the sense that in the vicinities of these defects, the graph is similar to some triangulation of surfaces with trivial topology. Among these examples, the "bubble-wrap" defects (a)-(c) do not increase the total energy, and around such defects the ratio between the number of edges and vertices is larger than 3. In other words, these defects can "absorb" the extra edges without energy cost. Also note that (a) and (b) do not change the long range order of the lattice orientation, while (c) does alter the long range order. Taken together, these defects induce configurational degeneracies in all the energy levels, including the ground state energy level, and at the same time induce graph permutation symmetry by randomly breaking the lattice's long range order, at least

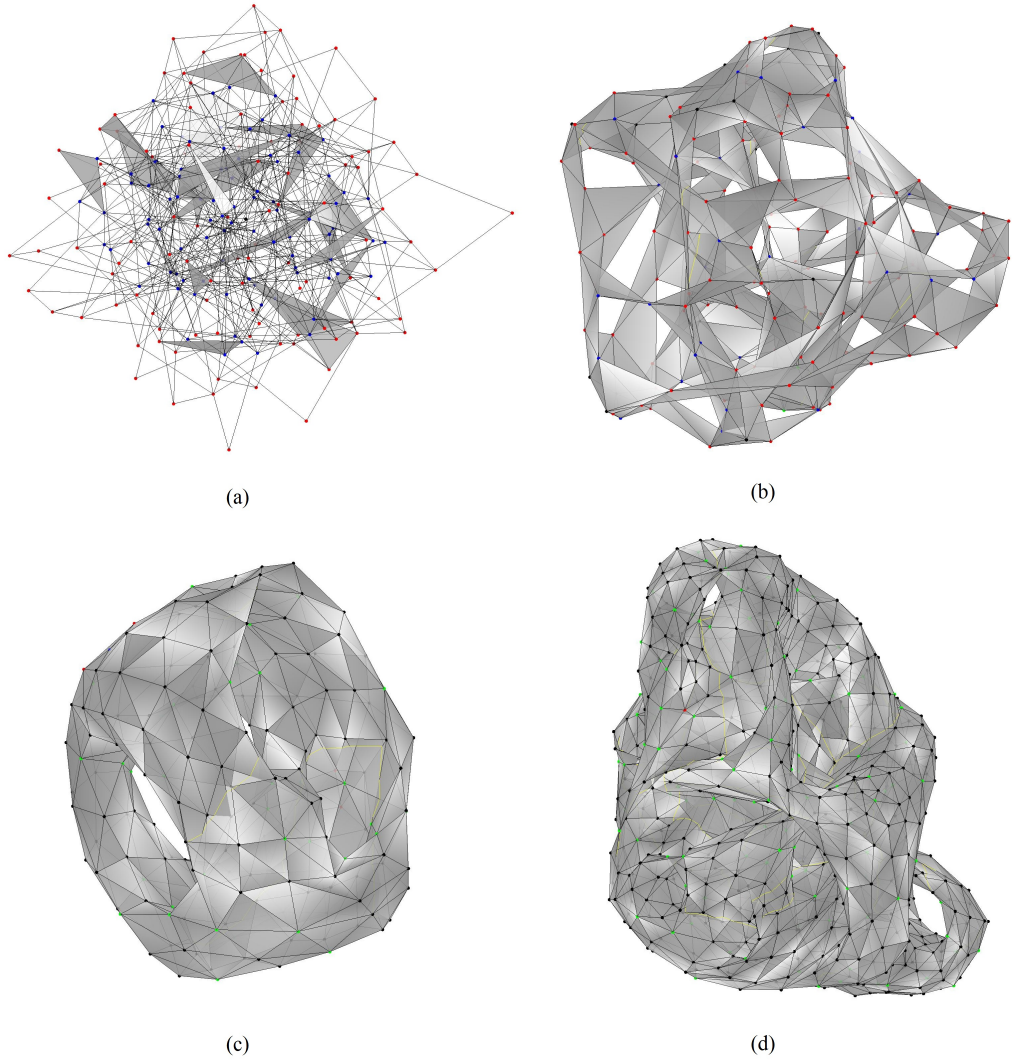

Figure 1.6: Some snapshots from the simulations, drawn in three dimensions. Panels (a)-(c) are for the system with number of vertices $N_V = 200$ and number of extra edges $X = 20$, where (a) is the initial configuration, (b) is a typical configuration at high temperature ($\beta = 1.0$), and (c) is a typical configuration at low temperature ($\beta = 2.0$). Compared with the sphere, the drawing (c) has three more handles, and the surface intersects with itself in three places, so it has a non-trivial, non-orientable topology. Panel (d) is for the system of size $N_V = 1000$ and $X = 100$, and shows a typical configuration at low temperature ($\beta = 2.0$). In these drawings, if a vertex has valency 6, it is black if its Δ value is zero, and is red if its Δ value is nonzero; if a vertex has valency 7, it is green if its Δ value is zero, and is blue if its Δ value is nonzero (see text). As well, yellow lines are drawn at places where two triangles intersect, and the manifold thus passes through itself.

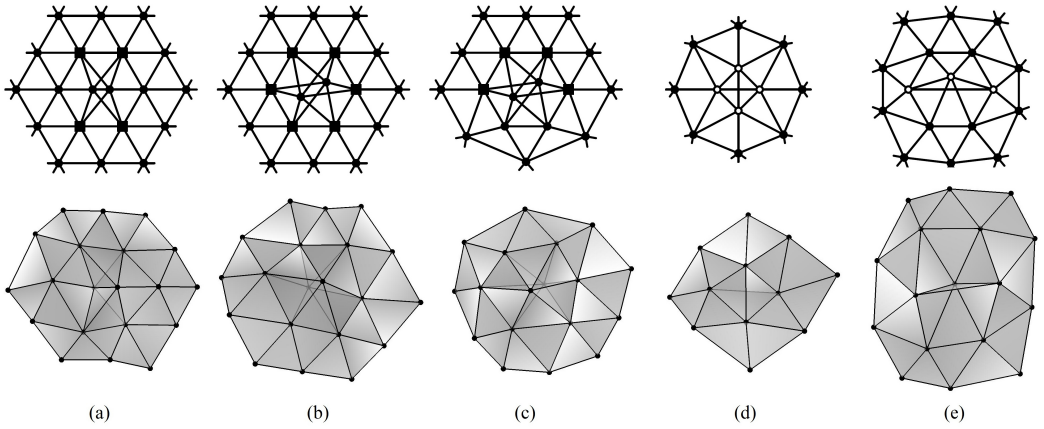

Figure 1.7: Examples of some common defects. Once the graph is triangulated to construct a surface, defects (a-d) have "bubble-wrap" morphology, while defect (e) has "frenulum" morphology. The figures in the first row are the schematic drawing of the defects, in which a vertex is marked with a square if its valency is 7, a vertex is marked with an open circle if it contributes positive energy to H_2, and otherwise a vertex is marked with a filled circle. The figures in the second row are the corresponding drawings of the defects using the method described in subsection 1.4.1. Compared with the equilateral triangular lattice, examples (a), (b), (c), (d) and (e) have 2, 3, 2, 0, 0 extra edges, respectively.

in the rendering scheme of the manifold described above. The bubble wrap defect (d) and "frenulum" defect (e) increase the total energy, and alter the lattice orientation more drastically.

As discussed above, low-temperature graphs in the model are similar to two-dimensional triangulated surfaces. However, they contain local defects, and there are overall topological features of the surfaces that emerge from the graphs. For example, in the drawing Figure 1.6(c), one can see that the emergent surface contains several handles, and the surface intersects itself in several places. In the drawing Figure 1.6(d), the topology of the emergent surface is too intricate to easily identify. The Hamiltonian does not constrain the topology in any way, so in general, emergent surfaces of low-temperature graphs in the model have complicated topologies. The emergent surfaces have potentially many handles, and are in general non-orientable, in that there is no separation between interior and exterior sides of the surface. In our simulations, we also observe that the topology of the graphs' emergent surfaces can dynamically change, even at a low energy.

We note, however, that the choice of N_V and N_E can constrain the topology. At low temperatures, the graphs are nearly triangulations, albeit with potentially complicated topologies. If a graph is strictly a triangulation, and we denote the number of triangles as N_F, then the Euler characteristic χ of the surface is given by $\chi = N_V - N_E + N_F$. For a triangulation, $3N_F = 2N_E$; and we previously defined $N_E = 3N_V + X$. Putting these three equations together, we find $\chi = -X/3$. As we showed above, defects on the graphs can absorb edges, so the relation for the nearly-triangulated graphs becomes an inequality $\chi \geq -X/3$. In addition, for any surface, $\chi \leq 2$, with $\chi = 2$ corresponding to the topology of a sphere. Thus the Euler characteristic χ of the emergent surface can take any integer value between $-X/3$ and 2. The X values used in our simulations are not very small, so this constraint still allows for many possible different topologies for the emergent surface.

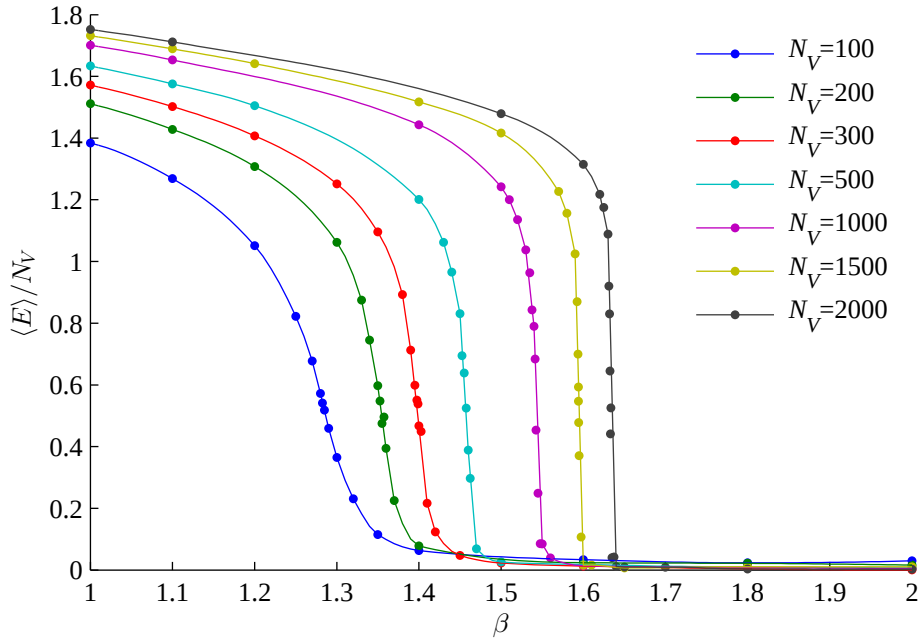

Figure 1.8: The average energy density $\langle E\rangle / N_V$ as a function of inverse temperature β for for several N_V's indicated in the legend.

1.4.3 Phase transition

In this sub-section we study the transition between the low-/high- temperature phases. For system sizes $N_V = 100, 200, 300, 500, 1000, 1500, 2000$, and number of excess edges $X = 0.1N_V$, the expectation value of energy $\langle E\rangle$, and the heat capacity $C = \beta^2\left(\langle E^2\rangle - \langle E\rangle^2\right)$ are computed for various inverse temperatures β, where the angle bracket here means averaging over all the samples in a simulation.

The results are shown in Figure 1.8 and Figure 1.9. For the three largest systems with $N_V = 1000$, $N_V = 1500$, and $N_V = 2000$, we also employ the weighted histogram analysis method (WHAM)* [22] to improve the sampling quality. The inverse transition temperature β_c is defined as the inverse temperature where the heat capacity is maximal. It can be seen that β_c increases as N_V increases, an effect also seen previously in other graph mod-

*See Appendix 1.7 for the details of our implementation of WHAM.

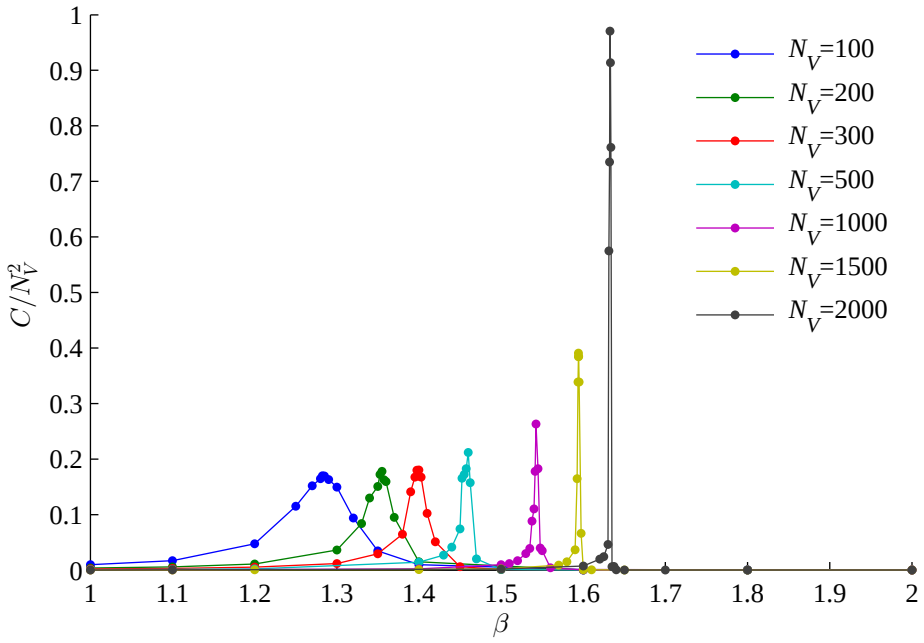

Figure 1.9: The rescaled heat capacity $C/N_V^2 = \beta^2 \left(\langle E^2 \rangle - \langle E \rangle^2 \right) / N_V^2$ as a function of inverse temperature β for several N_V's indicated in the legend.

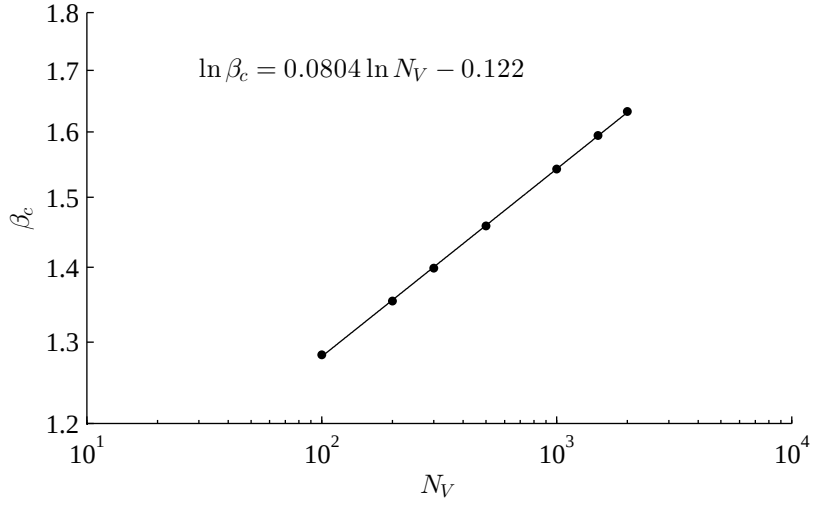

Figure 1.10: Log-log plot of the inverse transition temperature β_c in the model as a function of system size N_V, and the best fit line. The straight line fit indicates that as $N_V \to \infty$, the transition temperature $T_c \to 0$.

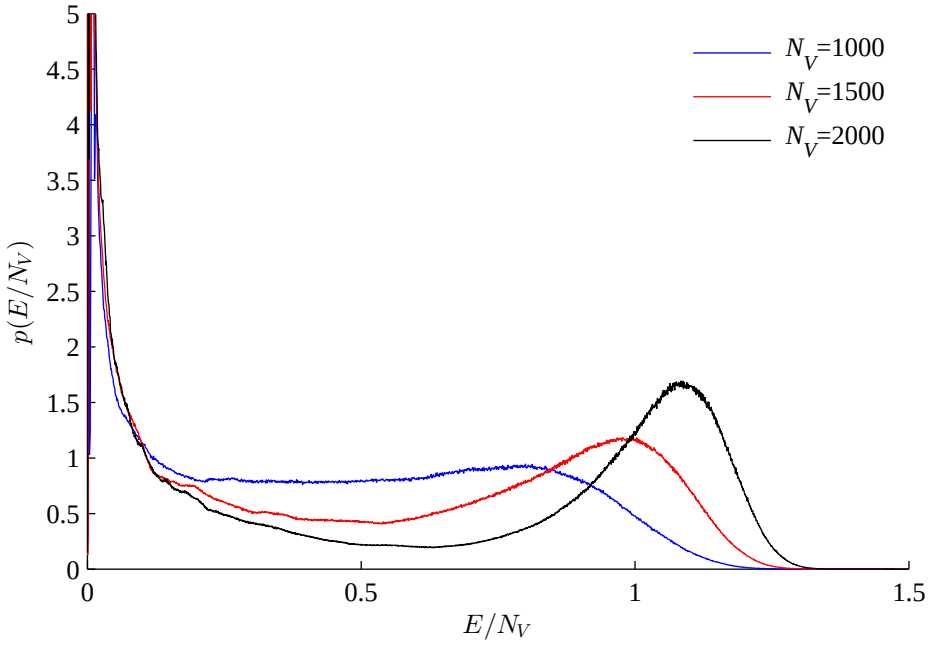

Figure 1.11: The probability density of the intensive energy E/N_V for the systems of size $N_V = 1000$, 1500 and 2000, at each system's transition temperature. The error of $p(E/N_V)$ for $E/N_V \geq 0.5$ is small ($\Delta p \leq 0.1$), the error for $0.01 < E/N_V < 0.5$ is $\Delta p \leq 0.6$, and the error for the smallest values of energy $E/N_V \leq 0.01$ is $\Delta p \leq 2.5$.

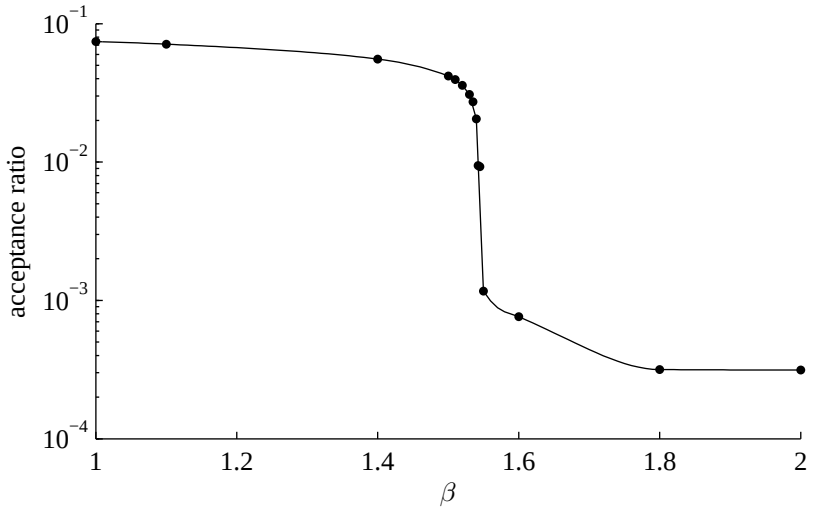

Figure 1.12: For the system of size $N_V = 1000$, the acceptance ratio of Monte Carlo moves in the simulations as a function of inverse temperature β.

els [13, 16] Near the transition temperature β_c, $|d\langle E\rangle/d\beta|$ also increases as N_V increases, and thus the widths of the heat capacity peaks decrease as N_V increases, indicating the transition becomes more cooperative. Figure 1.10 shows a log-log plot of the inverse transition temperature as a function of N_V. The linear relation in the plot indicates that as N_V goes to infinity, the transition temperature would go to zero. In addition, Figure 1.11 shows the probability density distribution of E/N_V, for the systems of size $N_V = 1000$, 1500, and 2000, at each system's transition temperature. As N_V increases, the energy distribution of the two phases become more bimodal, and the temperature-dependence of the heat capacity in Figure 1.8 becomes sharper, indicating a more cooperative transition with increasing system size [23, 24]. Together this implies that the transition is first order in the bulk limit, with a corresponding nucleation barrier [25]. That is, a Landau functional using system energy as an effective order parameter has a double-well structure with corresponding barrier separating the low- and high-energy phases [26].

The acceptance ratio as a function of β for $N_V = 1000$ is plotted in Figure 1.12. The low energy phase occupied at large values of β has a much lower acceptance ratio than

the high energy phase, both because of the lower temperature and because the low energy graphs have much more structural constraints, and thus have more rigidity with respect to the local moves. However, because some the local defects cost little or no energy, low energy graphs still have non-zero acceptance ratio, and so are able to undergo dynamics during the simulations.

A transition temperature of zero for infinitely large graphs is actually not very surprising on entropic grounds. Consider a first order phase transition of an extended physics model. Denote the size of the system by N, and denote the number of states in the high- and low-temperature phases by Ω_{H} and Ω_{L}, respectively. Because the energy difference between these two phases is proportional to N, the phase transition temperature T_c is given approximately by $\Omega_{\mathrm{H}} e^{-\kappa N/T_c} = \Omega_{\mathrm{L}}$, where κ is a positive number. As N increases, for a "typical" physics system with short-ranged interactions, the ratio between Ω_{H} and Ω_{L} increases as $e^{\gamma N}$, where γ is a positive number. This behavior results in a finite, non-zero transition temperature in the infinite size limit. On the other hand, the number of inequivalent graphs with N_V vertices is typically $N_V^{\gamma' N_V}$, (see, e.g., [3,13,27], also see Appendix 1.9 for more examples) where γ' is a positive number that depends on the constraints of the allowed graphs. In our case, the allowed graphs should have every vertex valency equal to six or seven, and every vertex neighborhood should be connected. While we do not have an algorithm to count the exact number of allowed graphs, it is reasonable to assume for our system that the ratio between Ω_{H} and Ω_{L} has the typical asymptotic behavior of graphs, which explains a transition temperature of zero, i.e., the transition temperature T_c is given by $N_V^{\gamma' N_V} e^{-\kappa N_V/T_c} \approx 1$.

To validate the above argument, we can calculate the entropy difference across the transition as given by

$$\Delta S = \int_{T_2}^{T_1} \frac{C(T)}{T} dT = \int_{\beta_1}^{\beta_2} \frac{C(\beta)}{\beta} d\beta, \tag{1.7}$$

where C is the heat capacity, and β_1 and β_2 are typical inverse temperatures in the high-temperature phase and low-temperature phase, respectively, which are taken to be $\beta_1 = \beta_c - 100/N_V$, $\beta_2 = \beta_c + 100/N_V$, i.e., we ensure that the window defining the transition

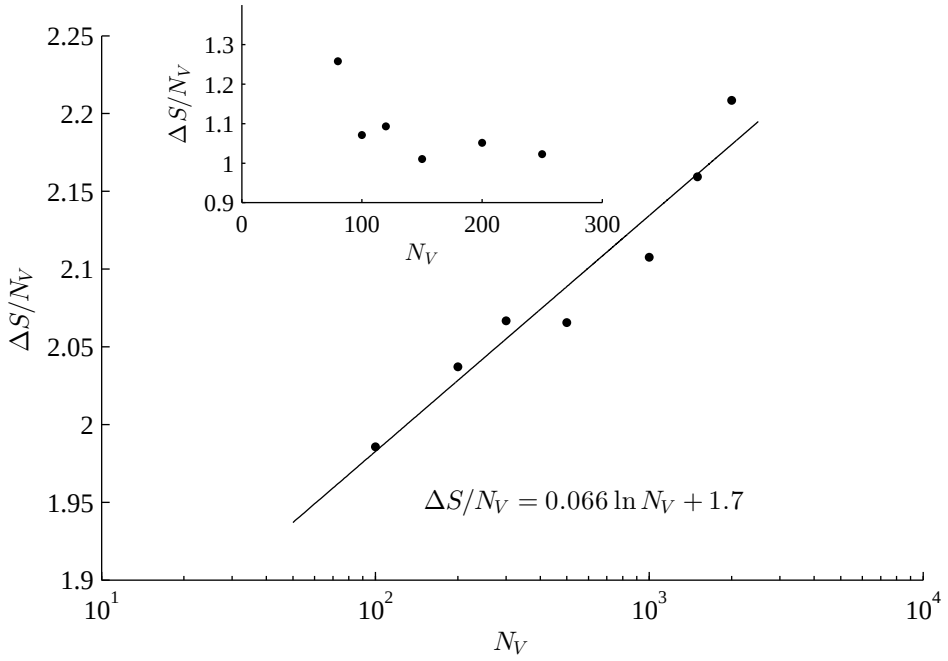

Figure 1.13: The entropy density difference across the transition $\Delta S/N_V$ as a function of N_V. The best fit line using a logarithmic function is also shown. The inset shows $\Delta S/N_V$ as a function of N_V for a model including a Coulomb potential between valency-7 vertices (see section 1.5). Including long-range interactions can remove super-extensivity of the entropy.

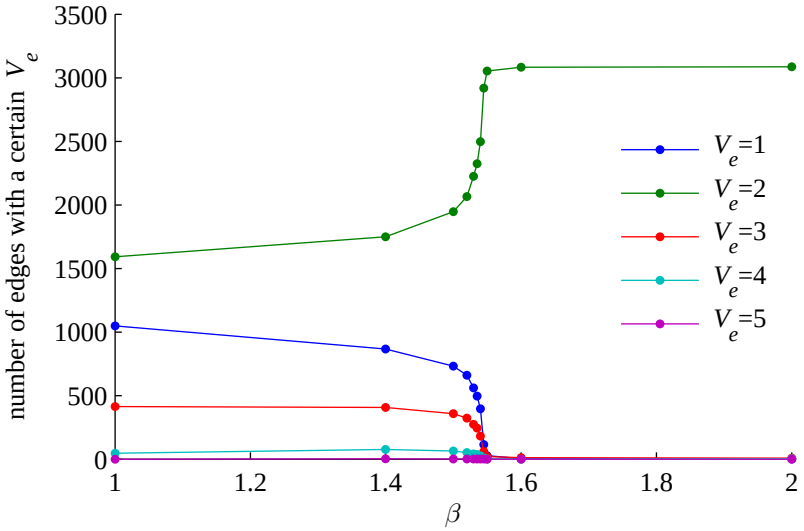

Figure 1.14: Distribution of edge valencies as a function of inverse temperature β_c, for the system of size $N_V = 1000$. There are no edges in the simulation with edge valency less than one or larger than five.

narrows as the width of the heat capacity peak narrows. Fig 1.13 shows the difference in entropy density $\Delta S/N_V$ as a function of N_V, which, rather than remaining constant, is a monotonically increasing function. Thus the entropy of the system is super-extensive. If the ratio $\Omega_{\rm H}/\Omega_{\rm L}$ of the model scales like $N_V^{\gamma' N_V}$ as argued above, $\Delta S/N_V$ will have the form $\Delta S/N_V = \gamma' \ln N_V + b$. The best fit line using this logarithmic function is also shown in Fig 1.13, which is consistent with a super-extensive entropy, with $\gamma' \simeq 0.065$.

1.4.4 Geometric properties

In this sub-section, we analyze some geometric properties of the two phases: if a geometric property is distinct in the two phases, it can serve as an order parameter that signals the phase transition.

As was mentioned before, because the low-energy graphs are nearly triangulations for our Hamiltonian, it is useful to introduce an order parameter that measures how similar graphs are to triangulations. For this purpose we can study the distribution of edge valen-

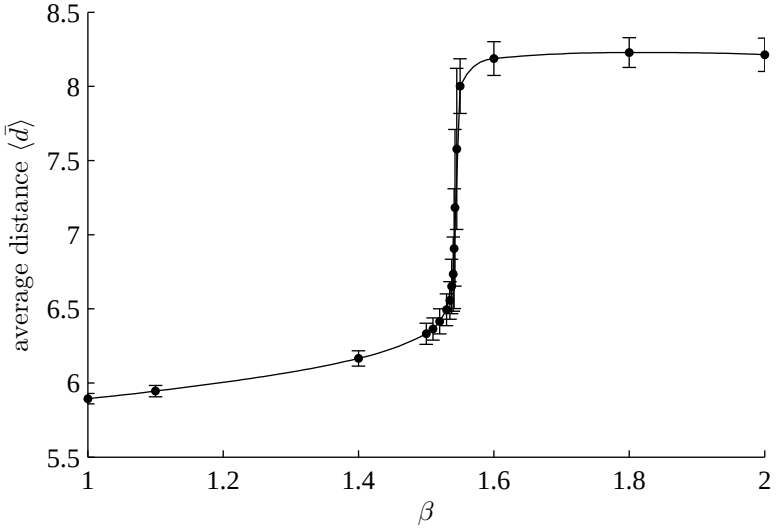

Figure 1.15: Average distance $\langle \bar{d} \rangle$ between pairs of vertices, plotted as a function of inverse temperature β, for the system of size $N_V = 1000$. $\langle \bar{d} \rangle$ is first averaged over all pairs of vertices in a given snapshot, and then averaged over all snapshots at a given temperature. The vertical bars at each data point indicate the standard deviation between snapshots: $\sqrt{\langle \bar{d}^2 \rangle - \langle \bar{d} \rangle^2}$.

cies, where the edge valency is defined as the number of triangles that an edge is part of. In a perfect triangulation of a surface without boundaries, the edge valencies are always two, so we expect that at low temperatures, the distribution of edge valency should approximate a delta function around two. The distribution of edge valencies for the system of size $N_V = 1000, X = 100$ is shown in Figure 1.14 as a function of temperature. Indeed, almost all edges have edge valency two at temperatures below the transition temperature. Near the transition temperature however, there is a sudden change in the distribution of edge valencies: above the transition temperature, edge valencies both above and less than two appear.

Another quantity that is useful as an order parameter is the average distance between all pairs of vertices, denoted by $\langle \bar{d} \rangle$, where the bar means averaging over all pairs of vertices in a graph, and the angle bracket means averaging over samples of an equilibrium simulation.

We expect that above the phase transition temperature, graphs will exhibit "small world" topologies and thus $\langle \bar{d} \rangle$ will be relativity small. The quantity $\langle \bar{d} \rangle$ gives the characteristic linear size of the graphs. Figure 1.15 plots $\langle \bar{d} \rangle$ *vs.* inverse temperature β, for $N_V = 1000$. Indeed, the low-temperature phase has a larger $\langle \bar{d} \rangle$ than the high-temperature phase; low-temperature graphs tend to have much more structure than high-temperature graphs, resulting in larger values of $\langle \bar{d} \rangle$.

In Figure 1.16, the average distance $\langle \bar{d} \rangle$ is shown as a function of the system size N_V, at $\beta = 1.0$ (above the transition) and at $\beta = 2.0$ (below the transition). The best fit lines using a logarithmic function and using a power function are also shown in Figure 1.16. The p-value for each best fit line is calculated for the null hypothesis that the residues $(d_{\text{fit}} - \langle \bar{d} \rangle)/\delta d$ come from a normal distribution with variance smaller than 1, so that a higher p-value indicates a better model. These relations between $\langle \bar{d} \rangle$ and N_V can be understood by comparing with random graphs, which generally display "small-world" connectivity, with average distances growing logarithmically with the number of vertices [3]. In our model, the Hamiltonian only constrains the graphs locally, so these graphs satisfy small-world behavior in the high temperature phase accurately, as shown by the logarithmic best fit line in Figure 1.16(a). For the low temperature phase, we can define an effective scaling dimension (see, e.g., [28])

$$D_s = \frac{d \ln N_V}{d \ln \langle \bar{d} \rangle}. \tag{1.8}$$

On a non-fractal surface, $\langle \bar{d} \rangle \sim N_v^{1/2}$, i.e., $D_s = 2$. However, it is seen from Figure 1.16(b) that the residuals with the square root function are too large. If we take D_s as a parameter in the fitting, a power-law function with $D_s \simeq 3.5$ is a much better fit to the empirical scaling. Perhaps surprisingly however, the logarithmic function is still the best fit function, indicating that the low-temperature graphs still display small-world connectivity. Enforcing a power-law fit at every system size, i.e., $\langle \bar{d} \rangle \sim N_v^{1/D_s(N_v)}$, would induce a variable dimensionality in the exponent.

Another related definition of dimensionality measures the increase in number of vertices with distance from a given vertex. On a graph, one can pick an arbitrary central vertex,

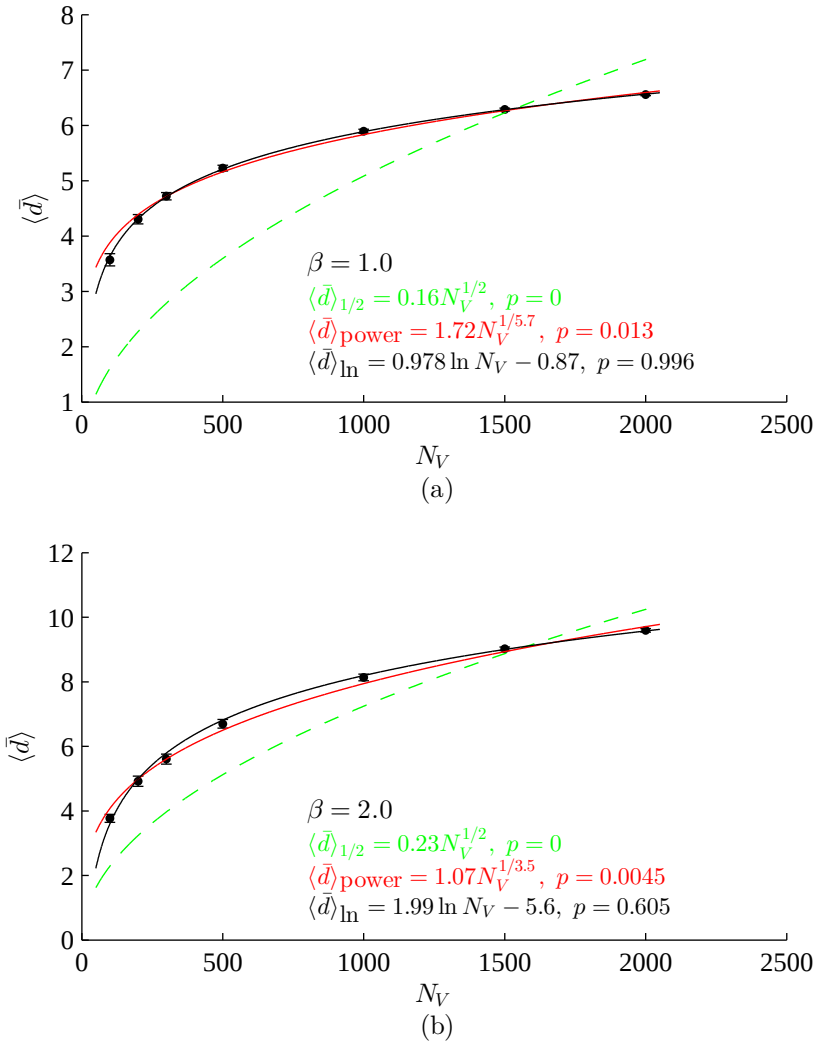

Figure 1.16: The average distance $\langle \bar{d} \rangle$ between pairs of vertices as a function of the system size N_V (discrete points), and the best fit lines using a square root function (green dashed lines), using a power function (red solid lines), and using a logarithmic function (black solid lines). Plots are shown both above the transition ($\beta = 1.0$) in panel (a), and below the transition ($\beta = 2.0$) in panel (b). For each best fit line, its expression and p-value are also shown, where the p-values are calculated for the null hypothesis that the residues $(d_{\text{fit}} - \langle \bar{d} \rangle)/\delta d$ come from a normal distribution with variance smaller than 1. For both temperatures, the logarithmic function gives the best fit to the measured data.

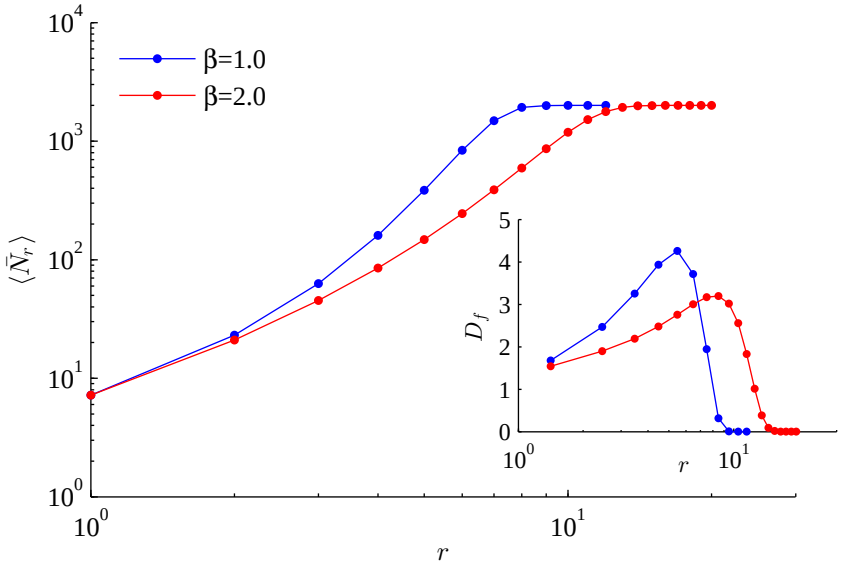

Figure 1.17: Log-log plot of $\langle \bar{N}_r \rangle$, the thermally averaged number of vertices within a distance r, as a function of r; the slope gives the dimensionality of the system, which in this case is distance-dependent. The plot shown is for the system with size $N_V = 2000$, at $\beta = 1.0$ (blue line) and at $\beta = 2.0$ (red line), which bracket the transition. For the same system, the inset shows the fractal dimension as a function of r.

and count how many vertices N_r have distance no greater than r from that center. We can then average both over all central vertices and over all equilibrium configurations at a given temperature, denoting the doubly averaged volume by $\langle \bar{N}_r \rangle$. If $\langle \bar{N}_r \rangle$ increases with r polynomially, the fractal (Haussdorf) dimension can be defined as

$$D_f = \frac{d \ln \langle \bar{N}_r \rangle}{d \ln r}. \tag{1.9}$$

In practice the dimension of the graph may itself depend on the radius r, so it makes sense to talk rigorously about the dimensionality of a graph only if D_f is essentially constant over some range of r. A log-log plot of $\langle \bar{N}_r \rangle$ vs. r is shown in Figure 1.17, for $N_V = 2000$ at $\beta = 1.0$ and $\beta = 2.0$, where the slope thus gives the dimensionality and is shown in the inset. One can see that the effective dimension D_f is smaller below the transition. Consistent with the previous analysis using (1.8), there is no well-defined dimension for the graphs, which are small-world-like. Instead there is an increasing dimensionality with increasing length scale, until boundary effects of the system are felt. The dimensionality has values around 2 for small values of r, because of the local lattice-like structure; it is also small for very large values of r, because a finite-sized graph must eventually be bounded, at which point $\langle \bar{N}_r \rangle$ will no longer increase polynomially at large r. Table 1.1 lists the maximal value of $D_f(r)$ for systems with different sizes, at inverse temperatures $\beta = 1.0$ and $\beta = 2.0$. As the table shows, $D_{f,\max}$ increases with N_V, which indicates that as N_V increases, there is no universal fractal dimensionality that can be approached by the graphs. Instead, the graphs are still small-world.

The small-worldness of the low temperature graphs in the bulk limit can be viewed as a consequence of the graph Hamiltonian in (1.5), which is a sum of local terms. The defects in the manifold are also local — in the bulk these have no effect on the large-scale structure of the resulting graphs. This is manifested for finite-size graphs by the fact that as N_V increases, the topologies of graphs become progressively more complicated, see e.g. Figure 1.6(c) and Figure 1.6(d). The manifolds contain numerous handles and surface intersections, so that a planar dimensionality does not adequately describe the system. In this sense there is already the signature in the low-temperature phase of the finite system

	$\beta = 1.0$	$\beta = 2.0$
$N_V = 1000$	3.62	2.72
$N_V = 1500$	3.99	3.11
$N_V = 2000$	4.26	3.20

Table 1.1: The maximal value of the fractal dimension D_f as defined in (1.9) for systems with $N_V = 1000$, $N_V = 1500$ and $N_V = 2000$, at inverse temperatures $\beta = 1.0$ above the transition and $\beta = 2.0$ below the transition.

that the bulk system is always disordered.

1.4.5 Correlation functions

Defects in this model such as those shown in Figure 1.7 contain irregularities that make them differ from part of a regular lattice. However, regions far away from them may not be affected by their existence; i.e., there may be no long-range correlation between such defects. In this subsection, we define and calculate correlation functions between defect pairs.

Because valency-7 vertices induce defects, we first measure the radial correlation function of valency-7 vertices. In general, the correlation between two random variables X, Y with expected values μ_X, μ_Y and standard deviations σ_X, σ_Y is defined as

$$\mathrm{corr}(X, Y) = \frac{E[(X - \mu_X)(Y - \mu_Y)]}{\sigma_X \sigma_Y}, \tag{1.10}$$

where E is the expectation value operator. In our case, we take all pairs of vertices with distance d in a graph; X is 1 if the first vertex in a pair has valency 7, and 0 otherwise, and Y is defined similarly for the second vertex. Then the correlation function is averaged over all equilibrium samples. The result for $N_V = 2000$, taken at inverse temperatures $\beta = 1.62$ and $\beta = 1.65$, which are marginally below and above β_c respectively, is shown in Figure 1.18(a). When the distance d is very small ($d = 1$ or 2), the correlation function deviates from zero, because of the local structure of of the defects (see Figure 1.7), which in this case

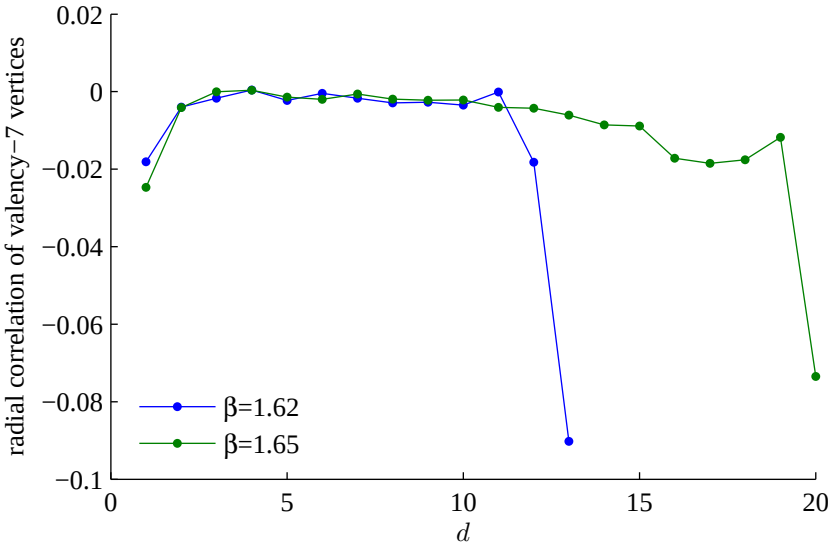

(a)

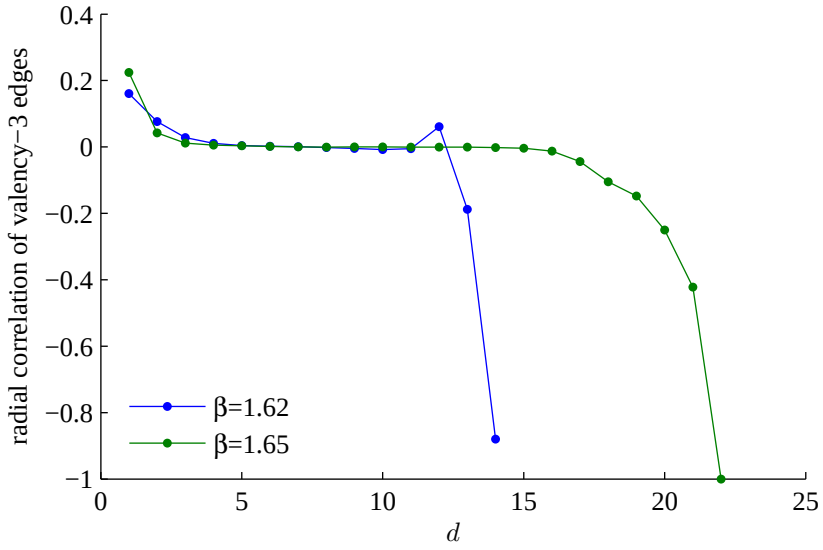

(b)

Figure 1.18: Radial correlation function defined through (1.10) of (a) valency-7 vertices and (b) valency-3 edges. Correlations are calculated for the system with size $N_V = 2000$ at $\beta = 1.62$, which is in the high-temperature phase, and at $\beta = 1.65$, which is the low-temperature phase.

induces anti-correlation. For intermediate values of d ($3 \leq d \leq 10$), the correlation is very small, indicating the defects are uncoupled. However, for large values of d, the correlation function becomes negative. This is because the valency of a vertex, and the distance from this vertex to other vertices, are not independent: compared with the valency-6 vertices, the valency-7 vertices tend to have smaller distances to other vertices. For example, for $N_V = 2000, \beta = 1.62$, the mean distance to valency 6 vertices is 7.18, while the mean distance to valency 7 vertices is 7.04. Thus it is less probable to find two valency-7 vertices with a large distance, and hence they anti-correlate at large distances. The correlation function is quite small over a range of d as one might anticipate, but the above global effect makes it difficult to quantitatively confirm that defects are decoupled at large distance.

As another measure of the correlation between defects, we can measure the radial correlation function of valency-3 edges, since their existence indicates deviation of the graph from a triangulation of surface. For example, every defect in Figure 1.7 contains valency-3 edges. The distance between two edges is defined by taking the 4 vertices defining the two edges, and finding the pair of vertices with the minimum distance between them. Since a pair of edges having a common vertex would then have a distance of zero, we add one to the above definition of edge distance. The results for $N_V = 2000$, at $\beta = 1.62$ and $\beta = 1.65$, are shown in Figure 1.18(b). At small distances ($d \leq 3$), there exists short range positive correlation between the valency-3 edges — the mean force between them is attractive, due again to the particular structure within a given low energy local defect. At large distances ($d \geq 14$ for $\beta = 1.62$, $d \geq 17$ for $\beta = 1.65$), the correlation function becomes negative, because valency-3 edges correlate with valency-7 vertices, which in turn anti-correlate at large distances for the reasons described above. However for a wide range of intermediate distances, this correlation function is also nearly zero, indicating again that the defect attraction is short-ranged.

1.5 Addition of a Coulomb potential

We found above that as the graph size N_V increased to infinity, the transition temperature T_c approached zero (Figure 1.10). This is apparently a universal property of models based on graphs, due to the super-extensive entropy of the high-temperature random phase. Similar arguments appear in the theory of phase transitions of low dimensional systems [29], wherein the non-extensive energy cost of defect formation is outweighed at any non-zero temperature by the (extensive) free energy due to translational entropic gain, so long as interactions are sufficiently short-ranged. This analogy motivated us to introduce a model with long-ranged interactions between defects, anticipating that in such a defect-filled system incurs super-extensive energetic cost, which may in turn result in a non-zero transition temperature.

Thus, in addition to the original two terms in the Hamiltonian (1.5), we introduce a nonlocal Coulomb potential term to the Hamiltonian, which gives a repulsive force between any pair of degree-7 vertices,

$$H_3 = c_3 \sum_{v,u \in V(G), v \neq u} \frac{\delta_{n_v,7}\delta_{n_u,7}}{d(v,u)}. \tag{1.11}$$

This is one of the simplest non-local Hamiltonian terms that one can add to the original Hamiltonian. The Coulomb force is chosen to be repulsive, because most of the high-temperature states are "small world", in that they have smaller average distances than those of low temperature states, so such a Coulomb potential can suppress the appearance of these "small world" graphs.

We test the effect of addition of this Coulomb term by another set of simulations, in which $c_3 = 1.0$. Figure 1.19 shows the sample drawings of graphs with $N_V = 200, X = 20$ (a) at high temperature ($\beta = 1.0$) and (b) at low temperature ($\beta = 2.0$). These temperatures bracket the heat capacity peak for the system so that the system is in the disordered and ordered phases respectively (Fig. 1.20). Because of the non-locality of H_3, simulations are much slower in practice than before and smaller systems are thus employed: simulations are performed for $N_V = 80, 100, 120, 150, 200$ and 250, and $X = 0.1N_V$. The inset of

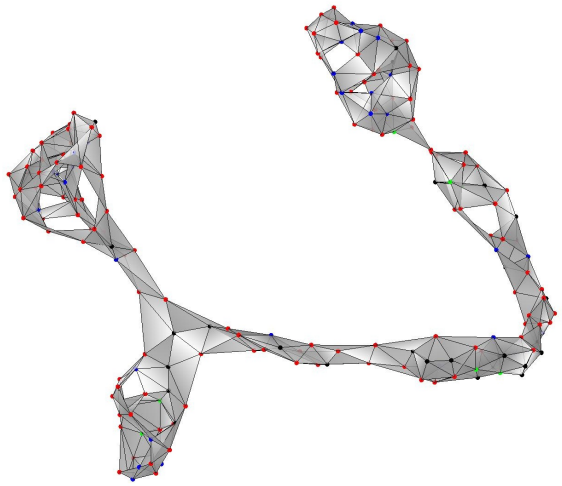

(a)

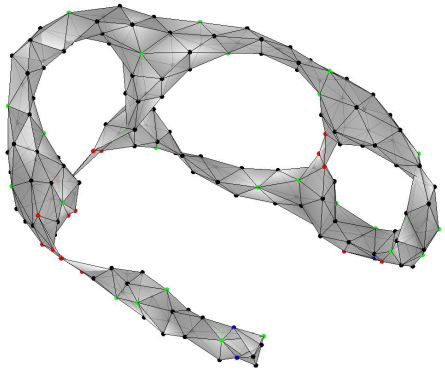

(b)

Figure 1.19: Sample configurations for the model with Coulomb potential in (1.11) with $c_3 = 1.0$, for the system with number of vertices $N_V = 200$ and number of extra edges $X = 20$, drawn in three dimensions. Panel (a) shows a typical configuration in the high-temperature phase with $\beta = 1.0$; panel (b) shows a typical configuration in the low-temperature phase with $\beta = 2.0$.

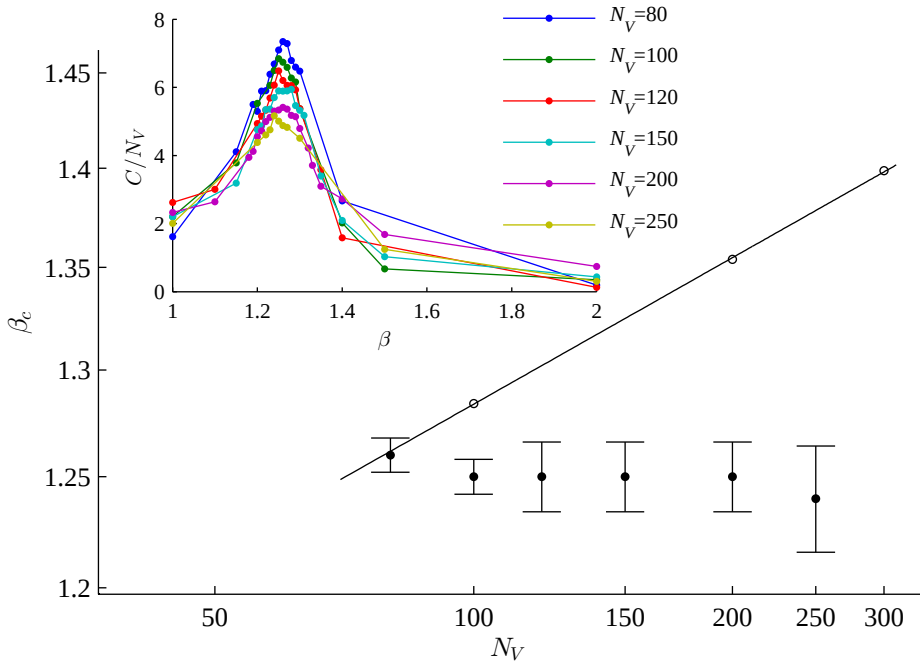

Figure 1.20: Log-log plot of transition temperatures β_c as a function of system size N_V, for the model with local Hamiltonian in (1.5) (drawn as circles, with best fit drawn as solid line), and for the model with Coulomb potential in (1.11) with $c_3 = 1.0$ added to the local Hamiltonian (discrete points with error bars). The inset shows the rescaled heat capacity C/N_V as a function of inverse temperature β for systems with the Coulomb potential added, and from which the values and uncertainties of β_c values are determined.

Figure 1.20 shows the rescaled heat capacity C/N_V as a function of β, for several system sizes. The rescaling factor is now chosen differently than in Figure 1.9, because the systems with the Coulomb potential have maximal heat capacity approximately proportional to N_V. From the maximal heat capacity, the inverse transition temperature β_c is determined, and is shown in Figure 1.20 (main panel), in comparison with the β_c values without the Coulomb potential.

From the graph drawings in Figure 1.19, we can see that because of the repulsive Coulomb force, both the high-temperature and low-temperature manifold configurations become rather extended to achieve longer average distances between defects. The characteristic linear size of the systems is much larger when the repulsive Coulomb potential is present, which penalizes the increase in complexity that was observed for a local Hamiltonian as N_V increased. This may also explain why the transition temperature does not change very much with N_V: The order of a neighborhood of a graph is not affected by a region far away from this neighborhood, regardless of whether or not the Coulomb potential is included. We can take this neighborhood to be a geodesic ball of radius r. For the model without the Coulomb potential, near the transition temperature, the fractal dimension (1.9) increases with N_V, which indicates that within a geodesic ball of radius r, the entropy of the disordered phase increases with N_V faster than that of the ordered phase, resulting in a decreasing transition temperature as N_V increases. For the model with the Coulomb potential, for graphs of size up to $N_V = 250$, the fractal dimension is nearly one, (see Figure 1.19,) so the entropies of both the disordered phase and the ordered phase within a geodesic ball of radius r remain nearly constant as N_V increases. This results in a nearly constant transition temperature.

We thus suspect that the entropy would be approximately extensive for the long-ranged interaction model. To quantify this, as a final check we plot the entropy change between disordered and ordered phases as a function of N_V in the inset of Figure 1.13, where ΔS is calculated by Equation (1.7), and $\beta_1 = 1.0$, $\beta_2 = 2.0$. As opposed to the entropy difference in the original model, $\Delta S/N_V$ of this model is approximately constant as N_V increases, i.e.

the entropy difference is no longer super-extensive, rather it is extensive or sub-extensive. It should be noted that the approximate extensivity of ΔS is a phenomenological result from the numerical simulations with limited graph sizes. We find no reason that the ΔS will continue to be extensive as N_V increases further. As indicated by the inset of Figure 1.13, ΔS may become sub-extensive when N_V increases beyond 250, which is the largest size that we have simulated. It is a subtle problem to find the appropriate form of the non-local interaction in the Hamiltonian that yields a model of graphs with finite, nonzero transition temperature in the large N_V limit.

We also simulate the model with an attractive Coulomb potential, in which $c_3 = -1.0$. Figure 1.21 shows sample drawings of graphs with $N_V = 200, X = 20$ (a) at high temperature ($\beta = 1.0$) and (b) at low temperature ($\beta = 2.0$). The effect of the attractive potential can be observed in these samples, in that the valency-7 vertices (green and blue dots) are usually located close together. In addition, because a local move must involve a valency-7 vertex, the configuration cannot evolve in the regions composed of purely valency-6 vertices, and thus the simulation is inefficient. As can be seen in Figure 1.21(b), in the region of valency-6 vertices, the configuration does not minimize the Hamiltonian (red dots have positive contribution to H_2), and is not a triangulation. Thus Figure 1.21(b) depicts a long-lived meta-stable state on an energy landscape of states characteristic of a frustrated system [23, 24]. Such a model has numerous local minima with large reconfigurational barriers between them, and consequently glassy relaxation dynamics.

1.6 Discussion

In this chapter we have constructed a graph model with a local Hamiltonian that simply enforces minimal valency subject to a given total number of graph links, along with a graph symmetry between the local graph radius and diameter. The above minimal condition along with fixed total link number gives rise to near constant valency for all vertices. This Hamiltonian gives rise to an emergent manifold at low temperature. The one free parameter in the model does not appear in the Hamiltonian but as an initial condition of the system.

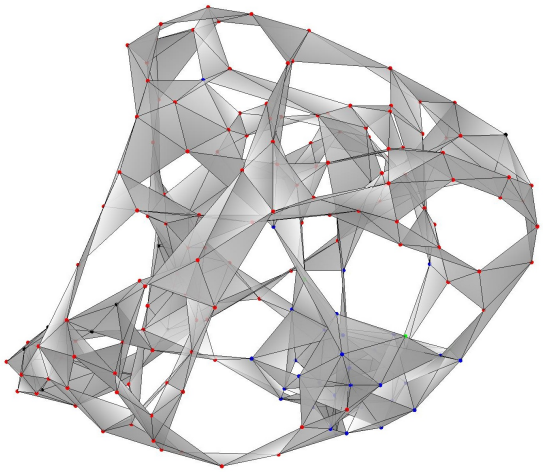

(a)

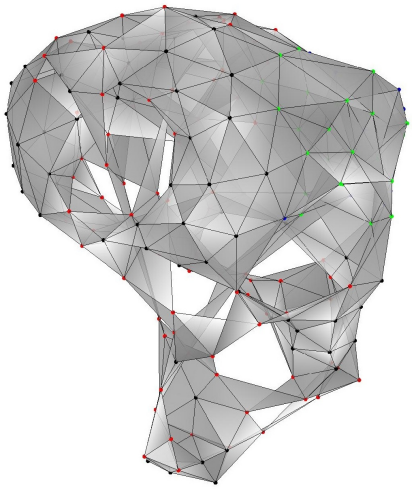

(b)

Figure 1.21: Sample configurations for the model with Coulomb potential in (1.11) with $c_3 = -1.0$, for the system of size $N_V = 200, X = 20$ drawn in three dimensions. Panel (a) shows a typical configuration in the high-temperature phase with $\beta = 1.0$; panel (b) shows a typical configuration in the low-temperature phase with $\beta = 2.0$.

This parameter α determines the edge to vertex ratio, which is conserved for the system and determines the dimensionality of the emergent manifold. When α is slightly larger than 6, the low temperature solutions have structural properties consistent with triangulations of two-dimensional surfaces. We obtained a representation of the emergent manifold by an optimization scheme, wherein adjacent vertices are brought as close as possible to a certain link distance, non-adjacent vertices are repelled from each other, and every triangular subgraph is assumed to be filled to render the manifold.

The spacetime manifold has historically been treated as a triangulation in several previous approaches, in order to regularize the partition function by constructing discrete analogs to the continuum manifold [30–34]. For example, in dynamical triangulation theory a given spacetime manifold is triangulated by simplices to calculate a discretized gravitational action [6,35,36]. In matrix models of gravity, graphs may be constructed as dual to Feynman diagrams arising from the limit of large internal symmetry group; by construction the graph constitutes a manifold. The partition function for 2-dimensional quantum gravity can be expressed as a sum over topologies of triangulated 2D surfaces, for actions of various forms describing the coupling between matter fields and spacetime [37]; this problem has connections to string theory via the Polyakov action [38]. The formalism may be extended to study higher dimensional generalizations of quantum gravity by group field theory models [39]. In this context, the emergence of a smooth "hydrodynamic" spacetime has been described as a condensation of simplicial quantum building blocks [40]. Such dual graph triangulations have widely varying vertex valency but generally represent manifold-like surfaces, at least in the condensed phase. In contrast, the emergent manifolds that we observe have near constant valency, but often bifurcating morphologies, e.g. the "bubble-wrap" or "frenulum" defects in Figure 1.7.

One can ask whether the present graph model could act as a substitute for the Feynman diagram construction in matrix models. The Feynman diagram construction has fixed valency, and is dual to a triangulated manifold, so a graph model of nearly fixed valency n_v could in principle give rise to an emergent manifold of dimensionality $n_v - 1$ as its

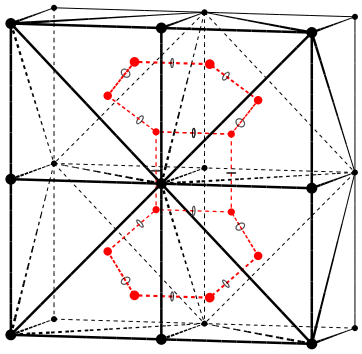

(a)

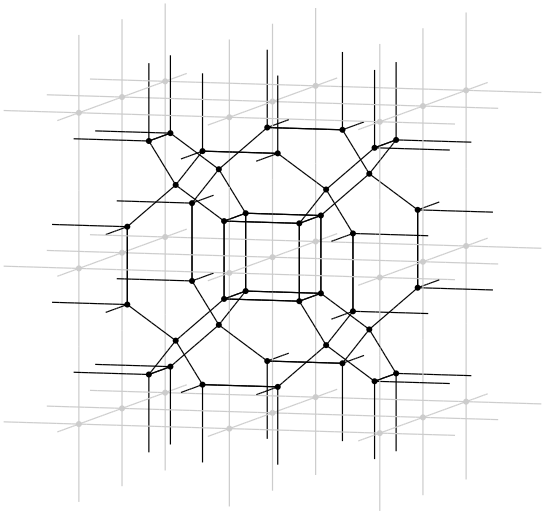

(b)

Figure 1.22: (a) A 3D cube triangulated into 5 tetrahedra [41] may be replicated by translation and reflection to tessellate the 3D space. Here, part of the dual lattice is shown as well in red. Red vertices are at the centers of the tetrahedra in the original triangulation. At the sites where the dual lattice bonds pass through the faces of tetrahedra in the original tessellation, open circles are drawn. (b) 3D Euclidean space subdivided into the cubes shown in panel (a) (grey lines); triangulation of the cubes in panel (a) is not shown explicitly here. The thicker black lines correspond to the dual graph of this triangulation.

dual. The present graph-symmetry-based Hamiltonian, and the resulting triangular lattice-like graphs in the low temperature phase, make this interpretation unlikely. The mean valency in the low temperature phase of our graph model is approximately 6, corresponding to the triangular lattice graph; we thus may consider a tessellation of a 5-dimensional Euclidean space by tetrahedra. The triangular lattice graph has smallest cycles of 3 vertices, corresponding to traversing the smallest triangles in the graph. However, a Euclidean tessellation using non-obtuse simplices will have cycles of its dual graph with no less than 4 vertices, i.e. due to the acuteness (or more precisely non-obtuseness) of the simplices, every cycle consists of a (potentially non-planar) polygon of at least 4 sides. As an illustration of this, consider the dual graph to a 3 dimensional tessellation by tetrahedra with non-obtuse dihedral angles. A section of a 3 dimensional tiling by such tetrahedra is shown in Figure 1.22(a), and the corresponding dual graph is shown in Figure 1.22(b). Here we see that the smallest cycles of the dual graph are indeed 4, corresponding to $\pi/2$ dihedral angles of the tiling tetrahedra. However a significant fraction of the cycles have length 6. Moreover, the cycles of length 4 appear as faces of 3D cubes in the dual lattice. All of this structure is incompatible with a regular planar graph of valency 4 as a potential dual to the 3 dimensional tessellation; in particular, a graph having the topology of a square lattice is ruled out.

In the model, there are no constraints on the global structure of the graph. As a consequence, the low-temperature phase can still retain complicated topologies with small-world properties, for which the corresponding manifold shows handles, self-intersections, and local defects that deviate from the manifold, in that a higher embedding dimension is necessary to represent them. Defects on the low-temperature manifold induce scattering and lensing effects on the propagation of bosonic matter fields [42], and are an interesting topic of future work for our model. As well, the presence of non-local links in the low temperature graph, and the corresponding non-locality in the emergent manifold, is consistent with the possible presence of disordered locality in loop quantum gravity [43], and might constitute a mechanism for its generation. In the context of loop quantum gravity, macroscopic ex-

pectation values of area or volume deviate from those on a flat metric by $\mathcal{O}(\ell_p^2)$ or $\mathcal{O}(\ell_p^3)$ where ℓ_p is the Planck length; nonlocal connections in the underlying metric modify the local Hamiltonian coupling a matter field to loop quantum gravity, but leave the above expectation values essentially unchanged, indicating locality may be macroscopically smooth but microscopically disordered.

As a general property of the graph model, the high-temperature phase has an entropy that grows super-extensively with system size N_V. This results in a transition temperature of zero in the limit $N_V \to \infty$, so that the infinite manifold is always disordered at any finite temperature. Aside from a finite universe or diverging coupling constraints as possible solutions, we implemented long-range interactions between vertex defects with repulsive Coulombic potential, to energetically penalize the many graph configurations with defect arrangements consistent with small-world topologies. In analogy with low-dimensional condensed matter systems, long-range potentials that couple defects induce prohibitive energetic cost to configurations that would otherwise destroy order entropically, so that an ordered phase at low temperature is restored. Here, we found that such potentials result in a nearly constant transition temperature as the size of the graph N_V increases. In addition, we found that attractive Coulombic potentials result in long-lived metastable states in the simulations.

Another interesting feature of the model is that the low lying energy levels, including the ground state level, have large configurational degeneracy. This residual entropy is due to local defects that can "absorb" extra edges without energetic cost. As well, the simulation dynamics indicates that the energy barriers between different low-energy states are not high. Thus at temperatures below the phase transition, the degrees of freedom in the system arising from this residual entropy are not frozen. The small or zero-energy barriers between degenerate states make the low-temperature graph system similar to the spin ices observed in spinel structures and pyrochlore lattices [44–46].

We have implemented here a sufficiently general Hamiltonian such that the same dynamic model can give rise to space-times of different dimensionality, i.e. spaces of different

dimensions are solutions to the same model. Exclusively from the graph theory point of view, there is no *a priori* reason to choose any particular dimensionality as a phenomenological term in the Hamiltonian. The "emergent dimensionality", then comes from initial conditions. Our motivation for this was to choose the simplest Hamiltonian possible, that was free of phenomenological parameters, so that the dimensionality of space-time was not "baked into" the energy function that governed dynamics. That said, we acknowledge that this approach effectively shifts the space-time dimension from extra phenomenological parameters in the Hamiltonian that favor or disfavor particular subgraphs [16], to special initial conditions. Our Hamiltonian is local in that it is a sum over all the vertices, and each term only depends on a small neighborhood (in our case, the neighborhood subgraph) of each vertex. This contrasts with other quantum graphity Hamiltonians, which have actions that depend on the number of loops with long lengths [12].

It is intriguing to interpret the low-temperature configurations of this graph model as an emergent spacetime — a notion other researchers have explored for similar graph models [5, 6, 11–16, 47]. In this picture, General Relativity is an effective "hydrodynamic" theory emerging from the collective dynamics of more fundamental degrees of freedom. The graph model is appealing in that both spacetime manifolds and locality emerge in the low-temperature regime of a discrete structure. The graph model introduced here gives rise to real, positive distances, so the emergent manifold can only be a Wick-rotated, Euclidean version of spacetime. Monte Carlo "time" steps in the current Hamiltonian methodology are distinct from the time evolution of the graph or manifold, and are only a mechanism to sample equilibrium states. In the present formulation, the Euclidean gravity theory undergoes a phase transition to smooth metrics below a "temperature" parameter β. Exploiting the isomorphism between the quantum propagator and the statistical mechanical partition function [48], the quantity $\mathrm{e}^{-\beta\mathcal{H}}/\int[dg]\mathrm{e}^{-\beta\mathcal{H}}$ is the equivalent to the Euclidean path integral measure that determines Green functions $\langle g_1 \dots g_n\rangle$ for the metric g in a quantum gravity model with the corresponding action. While we have seen a phase transition for the system with Euclideanized action, the identification of the appropriate thermal quantum states

that are periodic in real time, and so related to the parameter β, is not clear at present. We see this problem of mapping back to the space-time coordinates with Minkowskian signature as a general challenge for quantum graphity models. Another general issue is the absence of an underlying symmetry principle to determine the action in quantum graphity models, analogous to the role of general covariance in the action for quantum gravity.

The complex topologies of surfaces corresponding to low-temperature graphs, along with graph defects having zero energetic cost, implies that a graph model consisting solely of the current Hamiltonian does not reduce to a classical theory of Euclidean gravity in the macroscopic limit. On the other hand, other discrete models of gravity are also known to have scale-dependent spectral dimension, indicating fractal, non-smooth geometries for the emergent manifolds at least at intermediate length scales [49–51]. The set of all possible low-energy graphs in this model could potentially be identified with the phase space of a Euclidean gravity theory before imposing the equation of motion, i.e., the space of all possible metrics modulo diffeomorphisms. Because the low-temperature graphs of our model are nearly triangulations, and random triangulations form the phase space of many other discrete gravity models [6,35–37,39], it may be interesting to investigate whether the graph model's action may be extended to include terms in dynamical triangulation theory, which do reduce to the gravitational action in the continuous limit.

The transition from disordered to ordered manifolds is first-order in the present graph model. However, the order of the transition, and its potential relevance to universality or independence of underlying lattice specifics, is a non-issue for the investigation of ordered phases below the transition, where correlation lengths are finite. Power-law correlations calculated in causal dynamical triangulation are between graphical elements analogous to graviton fields, so that graviton coupling is power law as in the classical limit. Space to time ratios of simplices have second order transition in this model, while the transition involving gravitational coupling is first order [52]. In any event, a graph model at a critical point would have wildly fluctuating connectivity and resemble more a fractal mix of ordered and disordered states, which is not consistent with an emergent manifold. The issue of the

universality classes and corresponding exponents of a transition is a separate one from the properties of an emergent manifold as a low-temperature phase below a phase transition. Retention of microscopic structure in the disorder to order transition is a prediction of the graph model, and may enable future experimental tests.

Finally, it is intriguing to speculate on the utility of a such a graph theoretical transition to describe a transition involving non-local to local causality, as might occur in a pre-inflationary universe. Such models may address the low-entropy initial condition problems that occur in inflationary models [53, 54].

1.7 Appendix: The weighted histogram analysis method

The weighted histogram analysis method (WHAM) is a method used to combine the samples from several Monte Carlo simulations taken under conditions of different temperature and added potential. We employ WHAM to generate optimal estimates of energy distributions of the graph model. In this model, the energy takes only integer values between 0 and $M = 1.5N_V$. Assume that S simulations are performed (in our cases, $S = 4$ for $N_V = 1000$, $S = 10$ for $N_V = 2000$), with inverse temperature β_i, and biasing potential $V_i(E)$, i.e., in the i-th simulation, the system is sampled with energy distribution $\Omega(E)\exp(-\beta_i(E + V_i(E)))$, where $\Omega(E)$ is the yet-unknown number of states with energy E. The inverse temperature β_i's are taken to be near the inverse transition temperature. Because there is a large free energy barrier between the low and high energy phases near the transition temperature, a biasing potential is used to obtain better sampling in the barrier region. The form of the biasing potential is taken to be parabolic:

$$V_i(E) = \begin{cases} v_i \left[\dfrac{\left(E - \frac{E_i^l + E_i^h}{2}\right)^2}{\left(\frac{E_i^h - E_i^l}{2}\right)^2} - 1 \right], & E_i^l \le E \le E_i^h, \\ 0, & E < E_i^l, \\ 0, & E > E_i^h, \end{cases}$$

where the parameters v_i, E_i^l and E_i^h are chosen by trial-and-error to make the energy distribution of each simulation as flat as possible.

After performing the simulations, let $n_i(E)$ be the number of counts of energy E from the i-th simulation, and N_i the total number of samples from the i-th simulation. From this information, the optimal estimate of the probability $p^0(E)$ of energy level E at inverse temperature β^0 without any biasing potential is given by

$$p^0(E) = \frac{\sum_{i=1}^{S} n_i(E)}{\sum_{i=1}^{S} N_i f_i c_i(E)}, \tag{1.12}$$

where $c_i(E)$ is the biasing factor $c_i(E) = \exp[-(\beta_i - \beta^0)E - \beta_i V(E)]$, and f_i is a normalization constant satisfying

$$f_i^{-1} = \sum_{E=0}^{M} c_i(E) p^0(E). \tag{1.13}$$

To solve these equations, we take an arbitrary set of initial values for f_i (namely $f_i^0 = 1$), and apply (1.12) and (1.13) iteratively to find the solution to these equations. After finding $p^0(E)$, it is then straightforward to calculate the average energy and heat capacity at inverse temperature β^0.

1.8 Appendix: The Floyd-Warshall algorithm

The most time-consuming step in the simulation is to compute the diameter and radius of the neighborhood subgraphs. A straightforward method is to find the length of shortest path for every pair of vertices in a neighborhood subgraph, using the Dijkstra's algorithm [55]. If a vertex v have valency d, which is also the order of its neighborhood subgraph, the running time of one implementation of the Dijkstra's algorithm is $O(d^2)$, so the running time for computing the diameter and radius of $G_N(v)$ is $O(d^4)$.

Instead of the Dijkstra's algorithm, the Floyd-Warshall algorithm [56, 57] is used in the simulation, which computes the distances of all pairs of vertices in a graph in one implementation. Denote the vertices of a neighborhood subgraph as $\{v_1, v_2, \ldots, v_d\}$. In this algorithm, a function $s(i, j, k)$ is defined to be the length of shortest path between v_i

and v_j, using only the set of vertices $\{v_1, v_2, \ldots, v_k\}$ as intermediate points along the path. $s(i, j, k)$ is computed by induction. The base case is

$$s(i,j,0) = \begin{cases} 1, & \text{if } v_i, v_j \text{ are adjacent,} \\ \infty, & \text{otherwise.} \end{cases} \tag{1.14}$$

Assume that $s(i, j, k-1)$ is known for all i, j. The are two possibilities for computing $s(i, j, k)$: either the shortest path between i and j using intermediate vertices in $\{v_1, v_2, \ldots, v_{k-1}\}$ is the shortest path between i and j using intermediate vertices in $\{v_1, v_2, \ldots, v_k\}$, or there is a shorter path that goes from v_i to v_k, using intermediate vertices in $\{v_1, v_2, \ldots, v_{k-1}\}$, and then from v_k to v_j, using intermediate vertices in $\{v_1, v_2, \ldots, v_{k-1}\}$. This can be summarized as the relation

$$s(i,j,k) = \min(s(i,j,k-1), s(i,k,k-1) + s(k,j,k-1)). \tag{1.15}$$

Thus for all i and j, $s(i, j, k)$ can be computed from $s(i, j, k-1)$ in running time $O(d^2)$. By definition, $s(i, j, d)$ gives the length of shortest path between v_i and v_j, and the total running time is $O(d^3)$. The operations inside the 3-fold loops is (1.15), which is composed of only an addition and a comparison, so this algorithm has better performance than the Dijkstra's algorithm even for small d's (in our case, 6 or 7).

1.9 Appendix: The number of random graphs and random semi-regular graphs

In this section, we give two examples of graph counting, to support the statement that when N_V is large, the number of inequivalent graphs with N_V vertices is typically $N_V^{\gamma' N_V}$, with γ' being a positive constant number. For this statement about the number of inequivalent graphs to hold, we actually allow for other multiplicative factors in the number of graphs, so long as they increase slower with N_V than $N_V^{\gamma' N_V}$. More formally, denote the number of inequivalent graphs by $\mathcal{N}$, we like to show that

$$\frac{\ln \mathcal{N}}{N_V \ln N_V} = \gamma' + O\left(\frac{1}{N_V}\right). \tag{1.16}$$

In the following, the Stirling's formula will be used,

$$n! = \sqrt{2\pi n}\left(\frac{n}{e}\right)^n\left(1+O\left(\frac{1}{n}\right)\right). \tag{1.17}$$

As a simplification of the simulated case, we first count the number of graphs with N_V labeled vertices, and N_E unlabeled edges. Define $n = \binom{N_V}{2}$, and the number is given by

$$\begin{aligned}
\mathcal{N} = \binom{\binom{N_V}{2}}{N_E} &= \frac{\binom{N_V}{2}!}{\left[\binom{N_V}{2}-N_E\right]!N_E!} \\
&= \frac{\sqrt{2\pi n}\left(\frac{n}{e}\right)^n\left(1+O\left(\frac{1}{n}\right)\right)}{\sqrt{2\pi(n-N_E)}\left(\frac{n-N_E}{e}\right)^{n-N_E}\left(1+O\left(\frac{1}{n}\right)\right)\sqrt{2\pi N_E}\left(\frac{N_E}{e}\right)^{N_E}\left(1+O\left(\frac{1}{N_E}\right)\right)} \\
&= \sqrt{\frac{n}{2\pi(n-N_E)N_E}}\frac{n^n}{(n-N_E)^{n-N_E}N_E^{N_E}}\left(1+O\left(\frac{1}{N_E}\right)\right) \\
&= \frac{1}{\sqrt{2\pi N_E}}\frac{n^n}{(n-N_E)^n}\frac{(n-N_E)^{N_E}}{N_E^{N_E}}\left(1+O\left(\frac{1}{N_E}\right)\right) \\
&= \frac{1}{\sqrt{2\pi N_E}}e^{N_E}\left(\frac{n}{N_E}-1\right)^{N_E}\left(1+O\left(\frac{1}{N_E}\right)\right)
\end{aligned}$$

If we take $N_E \simeq 3N_V$ as in the simulations, then the above number becomes

$$\mathcal{N} \simeq \frac{1}{\sqrt{2\pi N_E}}e^{N_E}\left(\frac{N_V}{6}\right)^{3N_V}\left(1+O\left(\frac{1}{N_V}\right)\right).$$

The dominant part of this number is thus $N_V^{3N_V}$.

The second example takes into account the distribution of valencies. Constrained by the Hamiltonian, all vertices in the model have valency-6 or 7. For a graph with N_V vertices and $N_E = 3N_V + X$ edges, there are $2X$ vertices with valency-7, and $N_V - 2X$ vertices with valency-6. The number of graphs with this distribution of valencies is [27]

$$\mathcal{N} = \frac{\binom{N_V}{2X}(3N_V+X)!}{(6!)^{N_V-2X}(7!)^{2X}}\left[\frac{2(3N_V+X)}{e}\right]^{3N_V+X}\exp\left[-\frac{21(3N_V+2X)(5N_V+4X)}{4(3N_V+X)^2}\right]\left(1+O\left(\frac{1}{N_V}\right)\right)$$

In our case, X is proportional to N_V, and it can be seen that the dominant term in this case also takes the form $N_V^{\gamma' N_V}$.

Two other constraints in the simulation, which are that the graph must be connected, and that all the neighborhood subgraphs must be connected, are not implemented in the above examples. However, we expect that this constraint will not change the general form of the graph counting.

Chapter 2

Aspects of Chern-Simons theory in $2+1$ dimensions

2.1 Introduction

Gauge symmetries play a crucial role in quantum field theory. Historically, the first well-studied gauge theory is the theory of electromagnetic field, and then its non-Abelian counterpart, Yang-Mills theory (see (2.2) below). Perhaps surprisingly, it was discovered that Chern-Simons theory (CST) in $2+1$ dimensions (see (2.1) below), for which the action takes a completely different form than the standard Yang-Mills action, is also a very interesting prototype gauge theory [58, 59]. From its action, it can be derived that CST possess many distinct properties from those of Yang-Mill theory. For example, CST is a topological field theory, and it imposes a chirality to the system, both of which will be discussed in detail later. The study of CST has uncovered several intriguing connections between CST and other topics in both mathematics and physics, including knot theory [59, 60], conformal field theory [61–64], and Morse theory [65]. CST has been widely used in building various physics models. For example, it is incorporated in models for quantum Hall effect [66], anyons [67], and protein folding with chirality [68].

One important motivation for studying CST is its relation with three dimensional gravity [69–72]: There exists a mapping between the gauge fields from the theory defined by the sum of two CSTs, and the metric field of gravity in $2+1$ dimensions. As a consequence, infinitesimal gauge transformations of CST are mapped to the infinitesimal diffeomorphisms of gravity. By quantization of CST, which is better understood than that of 3D gravity,

quantization of 3D gravity then becomes relatively straightforward. Because of the difficulties involved in four (or more) dimensional gravity theories (see, e.g., [73–76]), 3D gravity is used as an important test ground for possible resolutions to its more realistic counterparts. Thus the relation between CST and 3D gravity is an important step in our exploration of models of quantum gravity.

Some subtleties exist in relating CST and 3D gravity [77, 78], however: By inspecting these two theories, one can note that CST is only well-defined if the spacetime manifold is orientable, while 3D gravity, which in principle includes all possible topologies of the spacetime manifold, has no such constraint. Thus it is natural to consider how the relation between CST and 3D gravity can be generalized to incorporate the case of non-orientable manifolds. For this purpose, the definition of integration of forms will be reviewed, and a more general version of integration – the integration of densities, which is well-defined on both orientable and non-orientable manifold will be applied to this relation. With some modifications, it will be shown that CST can be utilized in calculating quantities in 3D gravity, now including the non-orientable topologies.

Another interesting aspect of the connection between CST and 3D gravity is the mapping class group (MCG) [79] of the spacetime manifold, which is the group of large diffeomorphisms of the spacetime manifold. Since a gravity model should possess the property of general covariance, which includes the MCG as a classical symmetry, it is reasonable to try to implement this symmetry into CST after the connection with 3D gravity is established. It is known that by incorporating the MCG in the process of quantization, non-trivial effects can emerge, e.g., the value of the coupling constant is constrained. This question will be studied in detail later in this chapter, for the case of U(1) gauge group, and in the process of quantization, the large gauge transformation group and the holonomy group are only required to have deformed representation after quantization.

The method of quantizing U(1) CST can also be applied to non-orientable manifolds, using the formalism of integration of densities. CST cannot be defined on non-orientable manifold however. Thus the analog theory, which is U(1) BF theory (named after the fields

involved in the theory, see (2.15) and (2.16)) in our case, will be quantized on non-orientable manifolds.

This chapter is organized as follows. In section 2.2, some relevant fundamental properties of CST will be reviewed. In section 2.3, the relation among the CST, the BF theory, and 3D gravity will be elucidated, especially when the space-time manifold is non-orientable. In section 2.4, some results from theory of MCG that are important to our calculations will be reviewed. In section 2.5, the U(1) Chern-Simons theory on orientable manifolds will be quantized in an explicit manner. In section 2.6, the same technique will be applied to quantizing U(1) BF theory on non-orientable manifolds.

2.2 Fundamentals of Chern-Simons theory

In this section some fundamental properties of CST will be reviewed. CST shows exceptionally rich structures after years of study. (For comprehensive review of CST, see e.g. [80].) This section will thus not cover all aspects of CST, but will focus on those aspects related with its relation with BF theory and 3D gravity, and the quantization of U(1) CST.

The action of CST is the integral of the Chern-Simons 3-form [81]:

$$I_{\mathrm{CS}}[A] = \frac{k_{\mathrm{CS}}}{4\pi} \int_M \mathrm{Tr}\left\{ A \wedge dA + \frac{2}{3} A \wedge A \wedge A \right\}, \tag{2.1}$$

where M is an orientable, three dimensional, spacetime manifold with no spatial boundary, A is a one-form field taking values in a Lie algebra[†] $\mathfrak{g}$, d is the exterior derivative, $\wedge$ is the wedge product operator, Tr is a trace operator on $\mathfrak{g}$, and the integration is the integration of n-forms defined on n-dimensional manifolds (for definitions of these terms, see, e.g., [83]). If M has spatial boundary, the action (2.1) should be supplemented with proper boundary terms. For simplicity, here and in the following, M is always assumed to have no spatial boundary.

[†]More generally, A is defined to be a connection of a G-bundle on M. If the bundle is trivial, and $\mathfrak{g}$ is the Lie algebra of G, then it reduces to the above simplified definition [82].

The standard Yang-Mills theory in $2+1$ dimensions has the action

$$I_{\mathrm{YM}}[A] = \int_M \sqrt{\det g} g^{\mu\rho} g^{\nu\sigma} \mathrm{Tr}\left(F_{\mu\nu} F_{\rho\sigma}\right) d^3x, \tag{2.2}$$

where $g^{\mu\nu}$ is a metric on M, $F = dA + A \wedge A$, and in this case the integration is the Riemann integration.

Compared with the Yang-Mills action (2.2), the most obvious features of the CST action (2.1) are that it has only first order derivative, and is independent of the metric on M. As will be explained later, these properties have important consequences for the structure of CST.

For both Yang-Mills theory and CST, the gauge transformation takes the form

$$A \to g^{-1} dg + g^{-1} A g, \tag{2.3}$$

where g is a Lie group G-valued field, and the corresponding Lie algebra of G should be $\mathfrak{g}$. When the difference between g and the unity is infinitesimal, the Yang-Mills action and the CST action are invariant under (2.3). However, for a general field g, the CST action (2.1) is not exactly invariant. Rather, it transforms as

$$I_{\mathrm{CS}}[A] \to I_{\mathrm{CS}}[A] - \frac{k_{\mathrm{CS}}}{4\pi} \int_{\partial M} \mathrm{Tr}((dgg^{-1}) \wedge A) - \frac{k_{\mathrm{CS}}}{12\pi} \int_M \mathrm{Tr}(g^{-1}dg) \wedge (g^{-1}dg) \wedge (g^{-1}dg). \tag{2.4}$$

On the right-hand side, the second term vanishes as M is assumed to have no boundary; the third term is a topological invariant [84], which is the winding number of g multiplied by $2\pi k_{\mathrm{CS}}$. If $\mathfrak{g}$ is non-abelian, there exists gauge transformations that give non-zero winding numbers. Thus for a non-abelian $\mathfrak{g}$, the path integral of the Chern-Simons action (2.1) is invariant under gauge transformations with nonzero winding numbers only if k_{CS} is an integer.

CST is known be a topological field theory, in the sense that observables of CST depend only on topological structures of the configuration, but not on the metric of the spacetime manifold [59] (see [85] for a review of topological field theory). This result is shown under a Dirac quantization, wherein the full phase space is quantized first, and then the gauge conditions are imposed at the quantum level. In an alternative method called the reduced

quantization, the gauge conditions are imposed at the classical level, and then the reduced phase is quantized. It is much easier to show that CST is topological under the reduced quantization, as it is only necessary to show that CST possess no local degree of freedoms classically. The proof of CST being topological under the reduced quantization is reviewed below.

In a nutshell, the absence of local degrees of freedom can be shown using a simple counting of degrees of freedom "per point". Assume that the rank of the Lie algebra $\mathfrak{g}$ is r. At one spacetime point, the A field has $3r$ degrees of freedom. In (2.1), there is no time derivative on the temporal component of A, so these r degrees of freedom act as Lagrangian multipliers and are not dynamical. By fixing the gauge symmetries generated by (2.3), r degrees of freedom are fixed by the gauge equation, and the last r degrees of freedom are fixed by the gauge-invariant condition. So in the end there is zero degree of freedom at each spacetime point, which shows the CST theory is classically topological. Of course, when the topology of M is non-trivial, this argument does not take the global structures into consideration. There are "left-over" discrete degrees of freedom which depend on the topology of M.

To be more precise, assume that M is in the form $M = \mathbb{R} \times \Sigma$, where $\mathbb{R}$ is the real line, and Σ is a compact two dimensional manifold without boundary. The 1-form field A defined on M can be decomposed as $A = A_t + A_\Sigma$, with A_t the temporal component and A_Σ the components on Σ. The Chern-Simons action is decomposed as

$$\begin{aligned} I_{\mathrm{CS}}[A] =& \frac{k_{\mathrm{CS}}}{4\pi} \int_M \mathrm{Tr} \left\{ A \wedge dA + \frac{2}{3} A \wedge A \wedge A \right\} \\ =& \frac{k_{\mathrm{CS}}}{4\pi} \int_M \mathrm{Tr} \left\{ A_t \wedge dA_t + A_\Sigma \wedge dA_t + A_t \wedge dA_\Sigma + A_\Sigma \wedge dA_\Sigma + 2A_t \wedge A_\Sigma \wedge A_\Sigma \right\} \\ =& \frac{k_{\mathrm{CS}}}{4\pi} \int_M \mathrm{Tr} \left\{ A_\Sigma \wedge d_t A_\Sigma + 2A_t \wedge (d_\Sigma A_\Sigma + A_\Sigma \wedge A_\Sigma) \right\} \\ =& \frac{k_{\mathrm{CS}}}{4\pi} \int_M \mathrm{Tr} \left\{ A_\Sigma \wedge d_t A_\Sigma + 2A_t \wedge F_\Sigma \right\}, \end{aligned} \tag{2.5}$$

where d_t and d_Σ are the exterior differentiation operators on $\mathbb{R}$ and Σ respectively. Note that in the second line, the first term vanishes because the wedge product is antisymmetric,

and the second and the third term cancel each other by doing integration by parts. In the above action, A_t acts as a Lagrange multiplier and enforces the constraint equation $F_\Sigma = 0$. In addition, gauge equivalent configurations need to be identified. Thus the reduced phase space is the space of flat connections on Σ modulo gauge transformations. This space is also the space of all possible holonomies around non-trivial cycles on Σ, modulo a constant gauge transformation. In mathematical terms, this is

$$\mathcal{M}_{\text{reduced}} = \text{Hom}(\pi_1(\Sigma), G)/\text{ad}\, G, \tag{2.6}$$

where $\pi_1(\Sigma)$ is the fundamental group of Σ, $\text{Hom}(\cdot,\cdot)$ is the space of homomorphisms, and $\text{ad}\, G$ is the space of adjoint action of G on the homomorphisms. This reduced phase space $\mathcal{M}_{\text{reduced}}$ is finite dimensional, because $\pi_1(\Sigma)$ and G are both finite dimensional. Thus the conclusion that CST is topological by the naive counting argument in the previous paragraph is confirmed.

2.3 Relation with the BF theory and 3D gravity

In this section we will study the relations between CST, BF theory and 3D gravity. 3D gravity in this thesis refers to standard General Relativity in three dimensions, which is defined by the path integral of the Einstein-Hilbert action

$$I_{\text{EH}} = \frac{1}{16\pi G}\int_M d^3x\sqrt{-\det g}(R - 2\Lambda) + \text{boundary terms}, \tag{2.7}$$

where the dynamic field g is a rank 2 symmetric tensor field on M with Lorentzian signature, Λ is the cosmological constant. In principle, the path integral includes all possible manifolds M satisfying the boundary conditions, if there is any boundary. Although the action has the same form as its higher dimensional counterparts, the theory can be shown to be free of any local degrees of freedom, so it is particularly simple to analyze. On the other hand, interesting solutions can be constructed in 3D gravity, such as propagating massive particles [86], black holes [87] and wormholes [88]. As a consequence, 3D gravity can be

viewed as a prototype quantum gravity theory, and be studied to understand the difficulties arisen from quantum gravity theories, such as the black hole entropy paradox [87].

It is well known that the action of 3D gravity can be reformulated as some gauge theory action [69, 70], usually the sum of two Chern-Simons actions. (See [71] for a review of the relation between the two theories.) Compared with 3D gravity, the corresponding gauge theories are defined on a fixed spacetime manifold rather than all possible manifolds, and their properties are better understood. Thus this relation between 3D gravity and gauge theory can further simplify the study of 3D gravity.

However, there are subtleties in this relation [77, 78]. One inequivalence is that some gauge theory configurations are mapped to degenerate metrics, which is putatively forbidden in gravity theories. As a result, the gauge theory phase space splits into several sectors, which are separated by the configurations corresponding to degenerate metrics, and the 3D gravity phase space is only one of these sectors. Quantizations of these two different phase spaces are generally different.

There is yet another inequivalence that will be focused on in this section. One can note that the Chern-Simons action (2.1), as an integral of 3-form, is defined only when the manifold is orientable. On the other hand, the 3D gravity theory is a theory of geometries, and should be well-defined regardless of the orientability of the space-time manifold. Actually, because we are dealing with gravity, no prior metric is present, so we hope to write the gauge theory action as an integral of differential forms. But if the space-time manifold is non-orientable, the conventional definition of such integral fails. Fortunately, there is a generalization of such integral – on an orientable or non-orientable n-manifold, n-form densities can be integrated. An n-form density is different with an n-form only in that, under a coordinate transformation with a negative Jacobian determinant, an n-form density obtains an extra minus sign. The mathematical definition of densities will constructed in detail below. In terms of such integral, 3D gravity in general can be written as a gauge theory known as BF theory. In [89], 3D gravity action with vanishing cosmological constant is written as an integral of a 3-form density, and the classical solution space for

the space-time topology $\mathbb{R} \times$ (Klein bottle) is discussed in detail. Our formalism below will generalize the results of [89] to arbitrary cosmological constant and arbitrary topology of the spacetime. Also, following the general recipe we developed, more models can be defined on non-orientable manifolds.

We show below that 3D gravity is related with BF theory, so that techniques developed for one theory can be utilized to deal with the other. Classically, BF theory is closely related with CST defined on the orientable double cover with parity conditions on the solution, with the exception that their mapping class groups do not map simply. Most results of Chern-Simons gravity remain true in this more general theory.

2.3.1 p-form densities and integration

In this subsection we review the mathematical formulation involving integration of densities, which can be used to deal with fields on non-orientable manifolds.

Recall that a diffeomorphism of open subsets of $\mathbb{R}^n$ is **orientation-preserving** if the Jacobian determinant of the diffeomorphism is everywhere positive. Let M be covered by the atlas $\{U_\alpha, \phi_\alpha\}_{\alpha \in A}$, where U_α's are open sets that cover M, and for each α, $\phi_\alpha : U_\alpha \to \mathbb{R}^n$ is a homeomorphism. The atlas is **oriented** if all the transition functions $g_{\alpha\beta} = \phi_\alpha \circ \phi_\beta^{-1}$ are orientation-preserving, and M is **orientable** if it has an oriented atlas. On an orientable manifold M, there are two sets of coordinate charts, which is defined such that charts in the same set have orientation-preserving transition functions. Either set is called an **orientation**, denoted by $[M]$. It can be shown that an n-dimensional manifold M is orientable if and only if there exist a nowhere vanishing n-form on M.

On an orientable n-dimensional manifold M, after choosing an orientation $[M]$, the (conventional) integration of a n-form is defined as follows. Given an oriented atlas $\{U_\alpha, \phi_\alpha\}_{\alpha \in A}$ within $[M]$, the integration of n-form τ is

$$\int_{[M]} \tau = \sum_{\alpha \in A} \int_{\mathbb{R}^n} (\phi_\alpha^{-1})^* (\rho_\alpha \tau), \tag{2.8}$$

where $\{\rho_\alpha\}_{\alpha \in A}$ is a partition of unity of the atlas A, $(\phi_\alpha^{-1})^*$ is the pullback of ϕ_α^{-1}, and the

integrals on the right-hand side are Riemann integrals [90]. Usually a fixed orientation $[M]$ is understood, and the integration is simply written as $\int_M \tau$. This definition of the integral $\int_M \tau$ has the property that it is independent of the atlas and the partition of unity.

With the above conventional integral of forms in mind, we define several concepts to deal with integration on non-orientable manifolds. All the following concepts and properties apply to both orientable and non-orientable cases, although for the orientable cases, they are rather trivial counterparts of the conventional concepts.

On a non-orientable n-dimensional manifold, an n-form indeed cannot be integrated. However, another set of objects, the n-form densities, can be integrated. Let the n-dimensional manifold M be covered by the atlas $\{U_\alpha, \phi_\alpha\}_{\alpha\in A}$. The **orientation bundle** (O, M, π) [91, 92] is a $\mathbb{Z}_2$-bundle over M, specified by transition functions $t_{\alpha\beta} = \mathrm{sgn}[\det(J_{\alpha\beta})]$, where $J_{\alpha\beta}$ is the Jacobian of the transition function between two charts. Let $\Omega^p(M)$ denote the bundle of smooth p-forms on M. A **p-form density** is a smooth section of the bundle $\Omega^p(M) \otimes_{\mathrm{p}} O$, where the notation $\otimes_{\mathrm{p}}$ means the the tensor product is taken for the fibers at each point.

One can see the orientation bundle merely stores information about relative orientation between local charts – if two overlapping charts have the same orientation, their transition function is 1, otherwise it is -1. In a local chart, assume a p-form density is expressed as $(a_{i_1\cdots i_p} dx^{i_1} \wedge \cdots \wedge dx^{i_p}, z)$, then the combination of coefficients $z \cdot a_{i_1\cdots i_p}$ of a p-form density transforms between two coordinate charts as [90]

$$\bar{z} \cdot \bar{a}_{j_1\cdots j_p} = \mathrm{sgn}(\det J) \sum_{i_1,\ldots,i_p} \frac{\partial x^{i_1}}{\partial \bar{x}^{j_1}} \cdots \frac{\partial x^{i_p}}{\partial \bar{x}^{j_p}} z \cdot a_{i_1\cdots i_p} \tag{2.9}$$

That is, they transform in the same way as coefficients of regular p-forms, except that there is an extra minus sign when the coordinate orientation is reversed. In physics, such an object is also called axial scalar/vector/tensor; examples include magnetic field and angular momentum.

The total space of the orientation bundle of M is called the **orientable double cover**[‡] of M, and is denoted as $\tilde{M}$. Because the fiber of this orientation bundle is a discrete set,

[‡]Note that given M, there can be other double cover spaces of M that is orientable. For example, a

and thus sections take constant values in the fiber locally, $\tilde{M}$ is indeed a double cover of M. Explicitly, $\tilde{M}$ is the set $(\bigcup_{\alpha\in A} U_\alpha \times \{\pm 1\})/\sim$, where $(x,z)\sim(x',z')$ if and only if $x = x' \in U_\alpha \cap U_\beta$ and $z = t_{\alpha\beta}(x)z'$. In this way $\tilde{M}$ is a two-fold cover of M, with the projection map $\pi : \tilde{M} \to M$ given by $\pi(x,z) = x$. $\tilde{M}$ as a manifold is described by the atlas $\{\tilde{U}_{\alpha,z}, \tilde{\phi}_{\alpha,z}\}_{\alpha\in A, z\in\mathbb{Z}_2}$, where the new atlas is labelled by two indices α and z, and $\tilde{\phi}_{\alpha,z} = (\phi_\alpha, z)$. If $U_\alpha \cap U_\beta \neq \emptyset$, then $\tilde{U}_{\alpha,z} \cap \tilde{U}_{\beta,t_{\alpha\beta}z} \neq \emptyset$, and the transition function is $\phi_\beta\phi_\alpha^{-1}$.

As suggested by its name, $\tilde{M}$ is orientable. This can be proven by using a refinement $\{V_\beta\}_{\beta\in B}$ of $\{\tilde{U}_{\alpha,z}\}$, that is, for any $\beta \in B$, there exists α and z such that $V_\beta \subseteq \tilde{U}_{\alpha,z}$, and $\{V_\beta\}_{\beta\in B}$ still covers $\tilde{M}$. Construct the functions $\chi_\beta(\tilde{x})$ such that $\chi_\beta(\tilde{x}) = 1$ for $\tilde{x} \in V_\beta$, $\chi_\beta(\tilde{x}) = 0$ for $\tilde{x} \notin \tilde{U}_{\alpha(\beta),z(\beta)}$, and $\chi_\beta(\tilde{x}) \geq 0$ everywhere. Then the n-form

$$\sum_{\beta\in B} z\chi_\beta(\tilde{x}) d\tilde{x}^1_\beta \wedge \cdots \wedge d\tilde{x}^n_\beta$$

is nowhere vanishing, because every nonzero term in the summand has the same sign, due to the expression of $t_{\alpha\beta}$, and at each point in $\tilde{M}$, at least one term is nonzero, since $\{V_\beta\}_{\beta\in B}$ covers $\tilde{M}$.

With respect to the involution $\sigma : \tilde{M} \to \tilde{M}$ given by $\sigma(x,z) = (x,-z)$, p-forms on $\tilde{M}$ split into **even forms** and **odd forms**

$$\Omega^p(\tilde{M}) = \Omega^p_+(\tilde{M}) \oplus \Omega^p_-(\tilde{M}) \tag{2.10}$$

according to $(\sigma^*\tilde{\omega}_+)(\tilde{x}) = \tilde{\omega}_+(\tilde{x})$, and $(\sigma^*\tilde{\omega}_-)(\tilde{x}) = -\tilde{\omega}_-(\tilde{x})$. The pullback $\pi^* : \Omega^p(M) \to \Omega^p_+(\tilde{M})$ is a bijection, so regular forms on M are equivalent with even forms on $\tilde{M}$. Given a p-form density ξ on M and $v_1, \ldots, v_p \in T_{(x,z)}(\tilde{M})$, we can define $\tilde{\xi} \in \Omega^p_-(\tilde{M})$ by

$$\xi(\pi_*(v_1), \ldots, \pi_*(v_p)) = \tilde{\xi}(v_1, \ldots, v_p) \otimes (x,z), \tag{2.11}$$

which gives an identification of p-form densities on M and odd forms on $\tilde{M}$. In plain words, on M there exists p-forms and p-form densities, and equivalently we can work on

circle S^1 can be double-covered by another S^1, while the orientable double cover of S^1 is two copies of S^1. Thus the name "orientable double cover" is a little confusing. In the following, we always use it to indicate the total space of the orientation bundle.

the orientable double cover $\tilde{M}$, on which we only consider p-forms with a definite parity. It is obvious that the wedge product of two odd forms is an even form, the wedge product of two even forms is an even form, and the wedge product of an odd form and an even form is an odd form, as their names suggest. These relations hold for p-forms and p-form densities correspondingly.

We can also define Lie algebra valued p-form densities. They are sections of the tensor product space $\mathfrak{g} \otimes (\Omega^p(M) \otimes_{\mathrm{p}} O)$.

The exterior derivative d commutes with σ^*, because in general, the exterior derivative commutes with pullbacks. The de Rham cohomology group splits accordingly,

$$H^p(\tilde{M}, \mathbb{R}) = H^p_+(\tilde{M}, \mathbb{R}) \oplus H^p_-(\tilde{M}, \mathbb{R}), \tag{2.12}$$

so we can talk about harmonic p-form densities on M, in addition to harmonic p-forms.

The most important property of densities is that a p-form density can be consistently integrated on a p dimensional manifold. From the above discussion, one can easily see that the following integration of p-form densities on a p-dimensional manifold M' is well defined,

$$\int_{M'} \xi = \frac{1}{2} \int_{\tilde{M}'} \tilde{\xi}, \tag{2.13}$$

where on the right side it is the regular integral of the corresponding odd p-form on the orientable double cover.

Consider a p-form density ξ supported on one coordinate chart. By (2.13), the integration of ξ is given in terms of the coordinates by

$$\int_{M'} \xi = \int z a_{i_1 \cdots i_p} dx^{i_1} \cdots dx^{i_p}$$

Under a diffeomorphism of M', the integration transforms into

$$\begin{aligned} &\int \bar{z} \bar{a}_{j_1 \cdots j_p} d\bar{x}^{j_1} \cdots d\bar{x}^{j_p} \\ &= \int \left[\operatorname{sgn}(\det J) \sum_{i_1, \ldots, i_p} \frac{\partial x^{i_1}}{\partial \bar{x}^{j_1}} \cdots \frac{\partial x^{i_p}}{\partial \bar{x}^{j_p}} z a_{i_1 \cdots i_p} \right] \left[\operatorname{sgn}(\det J) \sum_{i_1, \ldots, i_p} \frac{\partial \bar{x}^{j_1}}{\partial x^{i_1}} \cdots \frac{\partial \bar{x}^{j_p}}{\partial x^{i_p}} dx^{i_1} \cdots dx^{i_p} \right] \end{aligned}$$

So the transformations of the two parts cancel exactly, and the integration is invariant under arbitrary diffeomorphisms, as opposed to regular integrations, which are only invariant under orientation-preserving diffeomorphisms. This conclusion holds for integration of a general p-form density, because it can be decomposed into a sum of p-form densities supported on one coordinate chart, using a partition of unity for M'.

From Stokes' theorem of regular integrations, using (2.13), we can prove the following Stokes' theorem for densities: Let D be a regular domain in a p-dimensional manifold M', and ξ be a $(p-1)$-form density of compact support. Then

$$\int_D d\xi = \int_{\partial D} \xi. \tag{2.14}$$

Example 1. As a first example, let M be orientable. By the nowhere vanishing n-form on M, all coordinate charts fall into two families: charts on which the coefficient of the n-form is positive/negative. Then the orientation bundle is a trivial $\mathbb{Z}_2$-bundle – it is composed of two disconnected copies of M, say $M_{\pm 1} = M \times \{\pm 1\}$. Given a p-form ω on M, the corresponding even form is $\pi^*\omega$. It happens ω also corresponds to an odd form, by $\tilde{\omega}_- = \pm\pi^*\omega$, for $x \in M_{\pm 1}$, and the p-form density is given by (2.11). So essentially there is no need to distinguish between p-forms and p-form densities when the manifold is orientable.

Example 2. A simple non-orientable example is the Möbius strip. It can be covered by three coordinate charts $(x, y) \in \phi_1(U_1) = [0, 1/2) \times [0, 1], (x', y') \in \phi_2(U_2) = [1/3, 5/6) \times [0, 1], (x'', y'') \in \phi_3(U_3) = [2/3, 7/6) \times [0, 1]$, and the transition functions are

$$\begin{aligned}
(x', y') &= \phi_{2,1}(x, y) = (x, y) \\
(x'', y'') &= \phi_{3,2}(x', y') = (x', y') \\
(x, y) &= \phi_{1,3}(x'', y'') = (x'' - 1, 1 - y'').
\end{aligned}$$

Consider a constant 0-form α and a constant 0-form density β. Assume that on U_1, $\alpha = a$, where a is a constant real number. By the coordinate transformation law, it is easy to see that $\alpha = a$ on all charts. Assume that on U_1, $\beta = b$, where b is a constant real number. By

the coordinate transformation law of densities, by $\phi_{2,1}$, $\beta = b$ on U_2; by $\phi_{3,2}$, $\beta = b$ on U_3; by $\phi_{1,3}$, $\beta = -b$ on U_1. Thus this constant 0-form density is inconsistent unless $b = 0$.

The orientable double cover of the Möbius strip by construction is covered by 6 coordinate charts, $\phi_{i,\pm 1}$, and the transition functions are

$$\begin{aligned}
(x'_+, y'_+) &= \phi_{2,+1,1,+1}(x_+, y_+) = (x_+, y_+) \\
(x''_+, y''_+) &= \phi_{3,+1,2,+1}(x'_+, y'_+) = (x'_+, y'_+) \\
(x_-, y_-) &= \phi_{1,-1,3,+1}(x''_+, y''_+) = (x''_+ - 1, 1 - y''_+) \\
(x'_-, y'_-) &= \phi_{2,-1,1,-1}(x_-, y_-) = (x_-, y_-) \\
(x''_-, y''_-) &= \phi_{3,-1,2,-1}(x'_-, y'_-) = (x'_-, y'_-) \\
(x_+, y_+) &= \phi_{1,+1,3,-1}(x''_-, y''_-) = (x''_- - 1, 1 - y''_-)
\end{aligned}$$

This is just a complicated way to describes a cylinder, because the transition functions listed above connect the coordinate charts one by one, with the last chart connected back to the first, and two of the transition functions flip the orientation. In fact, if M is non-orientable, its orientable double cover $\tilde{M}$ is always connected.

2.3.2 The relation

In the previous sub-section the integral of n-form densities on non-orientable n-manifolds was defined. Using this construction we can define field theories on manifolds with either orientability by finding some n-form density as the Lagrangian. The BF theory [93] is such a theory. The action of the BF theory in three dimensions is written as

$$I_{\mathrm{BF0}}[A, B] = \frac{k_{\mathrm{BF0}}}{2\pi} \int_M \mathrm{Tr}\left\{B \wedge F\right\}, \tag{2.15}$$

where the integral now is an integration of densities, A is a $\mathfrak{g}$-valued one-form field, B is a $\mathfrak{g}$-valued one-form density, $F = dA + A \wedge A$, and k_{BF0} is the coupling constant. This theory is well-defined regardless of the orientability of M.

Because we like to map the BF theory to 3D gravity with arbitrary cosmological constant (see (2.24)), a generalized BF theory is needed. To construct a n-form density, it is required

each term of the Lagrangian includes odd number of densities. In $n = 3$ dimensions, another term composed of A and B may be added to (2.15),

$$I_{\mathrm{BF}}[A, B]_M = \frac{k_{\mathrm{BF}}}{2\pi} \int_M \mathrm{Tr} \left\{ B \wedge F - \frac{\Lambda}{3} B \wedge B \wedge B \right\} \tag{2.16}$$

where k_{BF} and Λ are parameters. When we relate this theory with 3D gravity below, Λ will become the cosmological constant. In the rest of this section, we will analyze this three dimensional, generalized BF theory, and will refer to it simply as BF theory. Using Stokes' theorem, its equations of motion are

$$\begin{aligned} dB + A \wedge B + B \wedge A = 0, \\ dA + A \wedge A - \Lambda B \wedge B = 0. \end{aligned} \tag{2.17}$$

Now we show that the BF theory is related with the 3D gravity theory. From the 3D gravity action

$$I_{\mathrm{EH}} = \frac{1}{16\pi G} \int_M d^3x \sqrt{-\det g}(R - 2\Lambda), \tag{2.18}$$

one can change the fundamental variable from the metric g to the local frame e and spin connection ω, according to the definitions

$$\eta_{ab} e_\mu{}^a e_\nu{}^b = g_{\mu\nu}, \tag{2.19}$$

$$\nabla_\mu e_\nu{}^a + \omega_\mu{}^a{}_b e_\nu{}^b = 0. \tag{2.20}$$

where $\eta = \mathrm{diag}\{-1, 1, 1\}$. We also define the spin connection field with one local index

$$\omega^a = \frac{1}{2} \epsilon^{abc} \omega_{\mu bc} dx^\mu.$$

where ϵ^{abc} is totally antisymmetric with $\epsilon^{012} = 1$, and its indices are raised and lowered by η^{ab} and η_{ab}. Note that in this change of variable, according to (2.19), the local frame e is determined by g up to a local Lorentz rotation. This symmetry is an additional gauge symmetry of the resulting model. On the other hand, ω is fully determined by e classically, so there is no more gauge symmetry associated with ω. In fact, it can be shown that ω is given by

$$\omega_\mu{}^a = \epsilon^{abc} e^\nu{}_c (\partial_\mu e_{\nu b} - \partial_\nu e_{\mu b}) - \frac{1}{2} \epsilon^{bcd} (e^\nu{}_b e^\rho{}_c \partial_\rho e_{\nu d}) e_\mu{}^a. \tag{2.21}$$

Now we rewrite the action (2.18) in terms of the new variables e and ω. The determinant of metric is related to the local frame e as

$$(-\det g) = (\epsilon^{\mu\nu\lambda} e_\mu{}^0 e_\nu{}^1 e_\lambda{}^2)^2,$$

where $\epsilon^{\mu\nu\lambda}$ is totally antisymmetric with $\epsilon^{txy} = 1$. When taking square root on both sides, there may or may not be an extra minus sign, so the volume element in the Einstein-Hilbert action (2.7) is

$$\sqrt{-\det g} d^3x = \frac{1}{6}\epsilon_{abc} e^a \wedge e^b \wedge e^c \cdot \mathrm{sgn}(\det e).$$

The left-hand side of the above equation is a volume form that can always be integrated; the right side is a 3-form, and it is integrable in general only if e^a is a 1-form density. So we identify e^a as a 1-form density field with a local frame index. According to the definition (2.20), ω^a is still a 1-form field with a local frame index. After some calculation, the Einstein-Hilbert action can be cast into the Palatini form [94],

$$I'_{\mathrm{P}} = \frac{2}{16\pi G}\int_M \left\{ \left[e^a \wedge \left(d\omega_a + \frac{1}{2}\epsilon_{abc}\omega^b \wedge \omega^c \right) - \frac{\Lambda}{6}\epsilon_{abc} e^a \wedge e^b \wedge e^c \right] \cdot \mathrm{sgn}(\det e) \right\}. \quad (2.22)$$

If the topology of M is fixed, this action appears to be a well-defined gauge theory action, except for the awkward term $\mathrm{sgn}(\det e)$. Actually, in gravity traditionally we require the metric to be non-degenerate everywhere, so for any gravity solution, the factor $\mathrm{sgn}(\det e)$ does not change sign, and thus has no effect at all. However, as soon as we write the metric in terms of the local frame in this way, we allow the factor $\mathrm{sgn}(\det e)$ to change sign within the space-time, which is equivalent to allowing the metric to take degenerate values. In other words, the gauge theory is not really a reformulation of 3D gravity, but an extension whose classical solutions include the gravity solutions as a subset [77,78]. For the same reason, one can also choose to neglect the factor $\mathrm{sgn}(\det e)$, and the result is another extension of 3D gravity. Due to difficulties in quantizing the original gravity theory, it is conjectured that such a gauge theory extension may give a quantization of 3D gravity [70]. For simplicity, we choose to neglect the factor $\mathrm{sgn}(\det e)$, so the action becomes

$$I_{\mathrm{P}} = \frac{2}{16\pi G}\int_M \left\{ e^a \wedge \left(d\omega_a + \frac{1}{2}\epsilon_{abc}\omega^b \wedge \omega^c \right) - \frac{\Lambda}{6}\epsilon_{abc} e^a \wedge e^b \wedge e^c \right\} \quad (2.23)$$

This Palatini gravity action is nothing but the BF action (2.16) with a cosmological constant term, if we interpret the local indices as labeling the components of a gauge field taking value in the Lie algebra $\mathfrak{sl}(2,\mathbb{R})$. Let $B = e^a T_a$, $A = \omega^a T_a$, where T_a is the following set of $\mathfrak{sl}(2,\mathbb{R})$ generators,

$$T_0 = \frac{1}{2}\begin{pmatrix} 0 & -1 \\ 1 & 0 \end{pmatrix}, \quad T_1 = \frac{1}{2}\begin{pmatrix} 1 & 0 \\ 0 & -1 \end{pmatrix}, \quad T_2 = \frac{1}{2}\begin{pmatrix} 0 & 1 \\ 1 & 0 \end{pmatrix}$$

They have the properties $[T_a, T_b] = \epsilon_{ab}{}^c T_c$, $\mathrm{Tr}(T_a T_b) = \frac{1}{2}\eta_{ab}$. Then

$$I_{\mathrm{P}} = I_{\mathrm{BF}} = \frac{1}{4\pi G}\int_M \mathrm{Tr}\left\{B \wedge (dA + A \wedge A) - \frac{\Lambda}{3} B \wedge B \wedge B\right\}. \tag{2.24}$$

This is the relation between BF theory and 3D gravity, at the level of Lagrangian. There are more conceptual differences between them. A gravity theory is supposed to include all possible manifolds. In our case, there is no spatial boundary, so all manifolds of the form $\mathbb{R} \times \Sigma$ with Σ a compact 2-manifold should be included. On the other hand, the BF theory is defined on a fixed manifold. If one performs a path-integral of 3D gravity, and decides to include the non-orientable configurations, our formalism allows computing contribution from the non-orientable manifolds to the path-integral, by means of BF theory.

A further step in this relation between theories is that the BF theory action is the sum of two Chern-Simons actions. In this relation, the Lie algebra of the BF theory is not restrained to $\mathfrak{sl}(2,\mathbb{R})$. This relation depends on the sign of the the parameter Λ. If $\Lambda < 0$, let $\ell = 1/\sqrt{-\Lambda}$, and define $A^{\pm} = \tilde{A} \pm \ell^{-1}\tilde{B}$, where $\tilde{A}$ is the even form field on $\tilde{M}$ corresponding to A, and $\tilde{B}$ is the odd form field on $\tilde{M}$ corresponding to B. Then

$$\begin{aligned} I_{\mathrm{BF}}[A,B]_M =& \frac{k_{\mathrm{BF}}}{4\pi}\int_{\tilde{M}} \mathrm{Tr}\Big\{\frac{\ell}{4}(A^+ - A^-)\wedge(dA^+ + dA^-) + \frac{\ell}{8}(A^+ - A^-)\wedge(A^+ + A^-)\wedge(A^+ + A^-) \\ &+ \frac{\ell}{24}(A^+ - A^-)\wedge(A^+ - A^-)\wedge(A^+ - A^-)\Big\} \\ =& \frac{\ell k_{\mathrm{BF}}}{16\pi}\int_{\tilde{M}} \mathrm{Tr}\left\{A^+ \wedge dA^+ + \frac{2}{3}A^+ \wedge A^+ \wedge A^+ - A^- \wedge dA^- - \frac{2}{3}A^- \wedge A^- \wedge A^-\right\} \\ =& \frac{1}{2}\left(I_{\mathrm{CS}}[A^+]_{\tilde{M}} - I_{\mathrm{CS}}[A^-]_{\tilde{M}}\right) \end{aligned} \tag{2.25}$$

where $I_{\mathrm{CS}}[A^{\pm}]_{\tilde{M}}$ is the Chern-Simons action $\frac{k_{\mathrm{CS}}}{4\pi}\int_{\tilde{M}}\mathrm{Tr}\left\{A^{\pm}\wedge dA^{\pm}+\frac{2}{3}A^{\pm}\wedge A^{\pm}\wedge A^{\pm}\right\}$, and the coupling constants of the two theories are matched by $k_{\mathrm{CS}}=\ell k_{\mathrm{BF}}/2$. It is well-known that the Chern-Simons theory is topological [59], so from this relation it is clear that the BF theory is topological too. Because $\tilde{A}$ is an even 1-form field and $\tilde{B}$ is an odd 1-form field, $A^{\pm}$ can not take arbitrary values. Rather, they must satisfy

$$\sigma^* A^+(\tilde{x}) = A^-(\tilde{x}), \tag{2.26}$$

where σ is the involution defined in Section 2.3.1. By this parity condition, A^- is determined by A^+. In fact, one can see that

$$I_{\mathrm{CS}}[A^-]_{\tilde{M}} = -I_{\mathrm{CS}}[A^+]_{\tilde{M}}. \tag{2.27}$$

The action of BF theory is re-expressed simply as

$$I_{\mathrm{BF}}[A,B]_M = I_{\mathrm{CS}}[A^+]_{\tilde{M}}. \tag{2.28}$$

This is an exact equivalence between the BF theory on M and the Chern-Simons theory on the orientable double cover $\tilde{M}$, which is a very well understood theory. Properties of the BF theory on the left-hand side of (2.28), such as its gauge symmetry, classical moduli space, and quantization schemes, can be read off directly from the Chern-Simons theory on the right-hand side of (2.28).

On the other hand, if $\Lambda>0$, we can let $\ell=1/\sqrt{\Lambda}$, and define $C=\tilde{A}+\mathrm{i}\ell^{-1}\tilde{B}$. Then

$$\begin{aligned}
I_{\mathrm{BF}}[A,B]_M =& \frac{k_{\mathrm{BF}}}{4\pi}\int_{\tilde{M}}\mathrm{Tr}\Big\{\frac{\ell}{4\mathrm{i}}(C-C^*)\wedge(dC+dC^*)+\frac{\ell}{8\mathrm{i}}(C-C^*)\wedge(C+C^*)\wedge(C+C^*)\\
&+\frac{\ell}{24\mathrm{i}}(C-C^*)\wedge(C-C^*)\wedge(C-C^*)\Big\}\\
=&\frac{\ell k_{\mathrm{BF}}}{16\mathrm{i}\pi}\int_{\tilde{M}}\mathrm{Tr}\left\{C\wedge C+\frac{2}{3}C\wedge C\wedge C-C^*\wedge dC^*-\frac{2}{3}C^*\wedge C^*\wedge C^*\right\}\\
=&\frac{1}{2\mathrm{i}}\left(I_{\mathrm{CS}}[C]_{\tilde{M}}-I_{\mathrm{CS}}[C^*]_{\tilde{M}}\right)
\end{aligned} \tag{2.29}$$

where the coupling constants of the two theories are again matched by $k_{\mathrm{CS}}=\ell k_{\mathrm{BF}}/2$. The gauge group of the right hand side theory is $G^{\mathbb{C}}$, which is some group with algebra $\mathfrak{g}^{\mathbb{C}}$,

which in turn is the complexification of $\mathfrak{g}$. However, the parity conditions on $\tilde{A}$ and $\tilde{B}$ are equivalent to the following condition on C,

$$\sigma^* C(\tilde{x}) = C^*(\tilde{x}). \tag{2.30}$$

Note that this does not imply the C field is real. Rather, this is a constrained Chern-Simons theory. The gauge transformations are parameterized by a $G^{\mathbb{C}}$-valued function $g^{\mathbb{C}}(\tilde{x})$,

$$C \to \left(g^{\mathbb{C}}\right)^{-1} dg^{\mathbb{C}} + \left(g^{\mathbb{C}}\right)^{-1} C g^{\mathbb{C}} \tag{2.31}$$

Gauge transformations consistent with the parity conditions are of the form

$$\sigma^* g^{\mathbb{C}}(\tilde{x}) = Z(\tilde{x}) g^{\mathbb{C}^*}(\tilde{x}), \tag{2.32}$$

where $Z(\tilde{x})$ belongs to the center of $G^{\mathbb{C}}$. As in (2.6), here the classical moduli space is $\mathrm{Hom}(\pi_1(\tilde{M}), G^{\mathbb{C}})/\mathrm{ad}\, G^{\mathbb{C}}$ with the constraint

$$\exp\left(\int_\alpha C\right) = \exp\left(\int_{\sigma\alpha} C^*\right). \tag{2.33}$$

Existing quantization methods of Chern-Simons theory [59,61,63,95–98] can still be applied, but the constraint (2.30) or (2.33) restricts the phase space that will be so quantized.

2.4 The mapping class group

In this section, we review some basic properties about the mapping class group, which will be needed in the following sections.

2.4.1 MCG on orientable manifolds

For an orientable manifold M without boundary, the mapping class group (MCG) is defined as

$$\mathrm{MCG}(M) = \mathrm{Diff}^+(M)/\mathrm{Diff}_0^+(M), \tag{2.34}$$

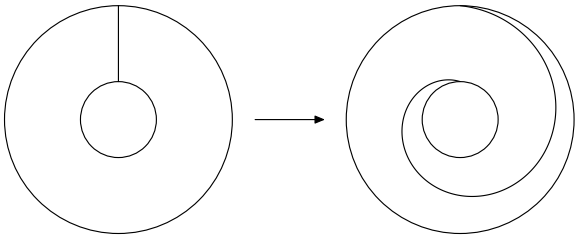

Figure 2.1: The map T constructed for defining the Dehn twist.

where $\mathrm{Diff}^+(M)$ is the group of orientation-preserving diffeomorphisms on M, and $\mathrm{Diff}_0^+(M)$ is the connected component of the identity in $\mathrm{Diff}^+(M)$. This definition thus can also be written as

$$\mathrm{MCG}(M) = \pi_0(\mathrm{Diff}^+(M)). \tag{2.35}$$

Elements of the MCG are called **mapping classes**.

A **closed curve** is a continuous map $S^1 \to M$. A closed curve in a manifold M is **simple** if it is embedded, i.e., if the map $S^1 \to M$ is injective.

We consider a special type of mapping class known Dehn twists, because of the following theorem known as the Dehn-Lickorish Theorem [99–101] : For the genus g surface with $g \geq 0$, the group $\mathrm{MCG}(\Sigma_g)$ is generated by finitely many Dehn twists about nonseparating simple closed curves.

A Dehn twist is constructed as follows (see Figure 2.1). Let A be the annulus $A = S^1 \times [0, 1]$, and let $T : A \to A$ be the "twist map" given by

$$T(\theta, t) = (\theta + 2\pi t, t).$$

Let M be a manifold and α be a simple closed curve in M. Let N be a regular neighborhood of α. We can define a homeomorphism $\phi : A \to N$. The Dehn twist about α is defined as

$$T_\alpha(x) = \begin{cases} \phi \circ T \circ \phi^{-1}(x), & \text{if } x \in N, \\ x, & \text{if } x \in M \backslash N. \end{cases}$$

It can be shown that the mapping class of T_α does not depend on the choice of N and the choice of ϕ. Moreover, the mapping class of T_α does not depend on the choice of α within its homotopy class a. Thus T_a is a well-defined element in $\mathrm{MCG}(M)$.

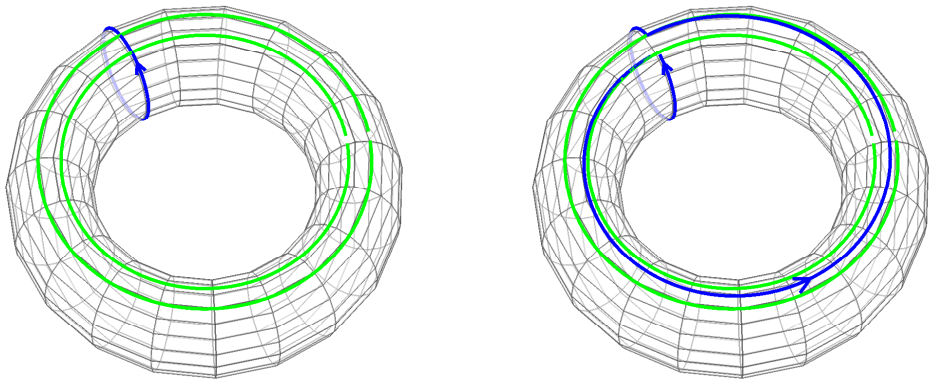

(a) (b)

Figure 2.2: The effect of a Dehn twist on a closed curve. The annulus in Figure 2.1 is embedded between the two green lines. The closed curve is shown as the blue directed loop. (a) and (b) show the curve before and after the Dehn twist operation, respectively.

The effect of a Dehn twist can be quantified by its action on the isotopy classes of simple closed curves (see Figure 2.2). A Dehn twist can be represented by a simple closed curve α. Another simple closed curve β is twisted by the Dehn twist by the following convention: after performing the Dehn twist, β is turned to the left at the point where it intersects with the representative curve α of the Dehn twist, and goes along α, until it comes back to the intersecting point and continues its original path.

Due to the Dehn-Lickorish Theorem, we can constrain ourselves to only study the generating set of Dehn twists, and the relations that they must satisfy in a specific presentation. One of the most convenient explicit presentation of $\mathrm{MCG}(\Sigma_g)$ is given by Wajnryb [102]. The form of the presentation splits into three cases: $g = 1$, $g = 2$, and $g \geq 3$. As a consequence, we shall discuss the quantization of these three cases in Section 2.5.2, Section 2.5.3 and Section 2.5.4, respectively, and we shall give the presentations in their respective sections.

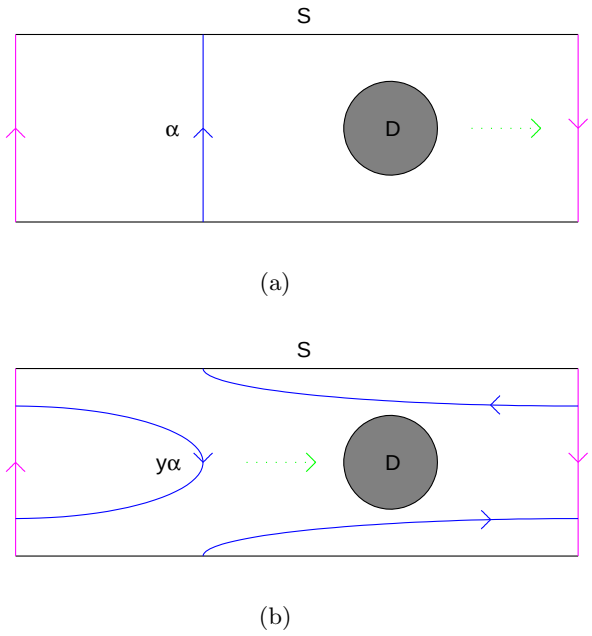

Figure 2.3: The map y constructed for defining the Y-homeomorphism. The Möbius strip S is represented by a rectangle, with its left side and right side identified along the magenta directed lines. The disc D is shown in grey color, and the green dashed arrows show its movement direction by the isotopy map f_t. The curve α is shown in blue color. The map y maps the configuration shown in (a) to the configuration shown in (b).

2.4.2 MCG on non-orientable manifolds

For a non-orientable manifold M without boundary, the MCG is defined slightly differently than (2.34) as

$$\mathrm{MCG}(M) = \mathrm{Diff}(M)/\mathrm{Diff}_0(M), \tag{2.36}$$

where $\mathrm{Diff}(M)$ is the group of diffeomorphisms on M, and $\mathrm{Diff}_0(M)$ is the connected component of the identity in $\mathrm{Diff}(M)$.

On non-orientable manifolds, in addition to the Dehn twists, there is another elementary type of mapping class called Y-homeomorphisms, or crosscap slides. The mapping can be constructed as follows (see Figure 2.3). Let S be a Möbius strip, and D be a disc in S. There is an isotopy map f_t on S such that $f_t|_{\partial S} = 1$, $f_0 = 1$, and $f_1\,|_D$ is an orientation

reversing homeomorphism of D. Intuitively, f_t can be viewed as a "slide" of D through S while fixing ∂S, and f_1 is when D travels around a circle and overlaps with its original position. Let L be another Möbius strip. There is a homeomorphism $g : L \to L$ such that $g|_{\partial L}$ is orientation reversing. As an example of g, if we represent L as a rectangle with the left side and right side identified (same as the representation of S in Figure 2.3(a)), then g can be defined as the map that vertically reflects the rectangle. Now glue L around ∂D to $S - D$, and call this space Y. Define the homeomorphism $y : Y \to Y$ by $y\big|_{S-D} = f_1\big|_{S-D}$, $y\big|_L = g$. For example, the curve α in Figure 2.3, which connects two points on ∂S, is mapped to $y\alpha$, which is not isotopic to α. Thus y is a nontrivial mapping class on the space Y.

Let M be a non-orientable manifold. If a subspace N of M is homeomorphic to Y via the map $\phi : Y \to N$, the Y-homeomorphisms is

$$y_N(x) = \begin{cases} \phi \circ y \circ \phi^{-1}(x), & \text{if } x \in N, \\ x, & \text{if } x \in M \backslash N. \end{cases}$$

As the Dehn twist, this is a well-defined element in MCG(M).

The analog of the Dehn-Lickorish theorem for non-orientable manifolds is still true [103,104]: The MCG on a non-orientable manifold without boundary is generated by finitely many Dehn twists and Y-homeomorphisms.

2.5 Quantization of U(1) CST on orientable manifolds

In this section, we consider the problem of quantization of U(1) CST on orientable manifolds. In the last two decades, several different ways to quantize CST has been studied [59, 61–63, 95–98, 105, 106], which have impact on diverse areas in mathematics and physics. The path-integral approach [59, 61] shed light on the relation between Chern-Simons theory, knot invariants and conformal field theory. Geometric quantization [95] gave a three-dimensional covariant formalism of the quantization. Canonical quantization can be performed using either a real polarization [62], or a complex polarization and coherent

states [63,105], and a general theory has been developed using quantum groups [96–98,106].

The example of Chern-Simons theory with a U(1) gauge group is particularly tractable in that quantization can be done explicitly. When the spacetime manifold has the product form $M = \mathbb{R} \times \Sigma$, with $\mathbb{R}$ the time and Σ a two-dimensional orientable surface, explicit wave-functions are obtained [107,108] and are identified with the generating functionals for the current correlator blocks of $c = 1$ rational conformal field theories [107].

Our goal in this section is to examine the role of the MCG of the orientable surface in quantizing U(1) CST. We shall demonstrate that the MCG is quantizable and we shall find its representation explicitly [2]. Quantization with a finite dimensional Hilbert space is possible only when the parameter $k = k_{\rm CS}$ in the Chern-Simons action (2.37) is a rational number [80, 109]. In [80, 107, 109], when $k = p/q$ with p and q coprime, it was stated that p (or k in [107]) must be an even integer. Our results differ qualitatively from these quantizations and depend on the genus. When the genus is one (Σ is the 2-torus), k can be any rational number. For higher genus, one of p or q must be even. Moreover, by incorporating MCG, we find that for a given k, the representations of the holonomy group and the large gauge transformation (LGT) group become unique, and the representation for MCG is also unique, apart from an arbitrary unitary sub-representation which acts on the holonomy group and LGT group trivially.

Generally, at the classical level, when Σ has genus g, the group of large gauge transformations is $\mathbb{Z}^{2g}$. We find that, commensurate with results of Ref. [107], this discrete group is realized undeformed at the quantum level only when k is an integer. However, even in that case, we find that, augmenting the quantization with the requirement that the Hilbert space carries a unitary representation of the MCG, restricts the representation of the LGTs to those where states are strictly invariant, i.e., theta angles associated with large gauge transforms vanish. Furthermore, we shall show that when k is rational but not integer-valued, the discrete group of LGTs, which was abelian at the classical level, obtains a 2-cocycle and becomes a clock algebra [80,109]. We find an interesting new result, where in there exists a $k \leftrightarrow 1/k$ duality of the representations of the homology group and the

large gauge group which, with the restrictions on k stated above, is compatible with our quantization of the MCG.

In a topological field theory, where the action does not depend on the metric, one may ask how the quantization of the MCG could be an issue at all. This is because in order to do canonical quantization, we must choose a set canonical variables, and to quantize, we must further choose a polarization. It is the latter which is not generally covariant. Covariance then needs to be restored by quantizing the MCG. As we shall show, the quantization of the MCG is non-trivial and, as we have discussed above, it can only be carried out with some restrictions on k and even then it poses restrictions on certain parameters which arise naturally in the quantization of the theory. See also [77, 110], where the question whether the MCG should be included in the quantization of CST, and its possible impacts, are discussed.

To avoid possible confusion, the notation conventions used in this section (Section 2.5) and the next section (Section 2.6) are listed on page xii.

2.5.1 General formalism

The action of CST with the U(1) gauge group simplifies from that in (2.1) to

$$I_{\mathrm{CS}}[A] = \frac{k}{4\pi}\int_M A \wedge dA, \tag{2.37}$$

and the gauge transformation simplifies from that in (2.3) to

$$A \to A + g^{-1}dg, \tag{2.38}$$

where g is a U(1)-valued function. We shall consider the Hamiltonian approach on a 3-manifold $M = \mathbb{R} \times \Sigma$ where $\mathbb{R}$ is time and Σ is a closed, oriented 2-manifold. The 1-form field A defined on M can be decomposed as $A = A_t + A_\Sigma$, with A_t the temporal component and A_Σ the components on Σ. The decomposition of the CST action can be written as

$$I_{\mathrm{CS}}[A] = \frac{k}{4\pi}\int_M (A_\Sigma \wedge d_t A_\Sigma + 2A_t \wedge d_\Sigma A_\Sigma) \tag{2.39}$$

where d_t and d_Σ are the exterior differentiation operators on $\mathbb{R}$ and Σ respectively. In the above action, A_t acts as a Lagrange multiplier and enforces the constraint that the connection on Σ is flat, $F_\Sigma \doteq d_\Sigma A_\Sigma = 0$. In the meantime, A_t is integrated over. Because only A_Σ appears in the analysis below, for simplicity, we use A to denote A_Σ from now on.

By Hodge decomposition, any 1-form field A can be written as

$$A = dU + \bar{d}V + h$$

where $\bar{d}$ is the adjoint to d, U is a 0-form, V is a 2-form, h is a harmonic 1-form, and U, V, h are all u(1)-valued. By the equation of motion $dA = 0$, because $d^2U = 0$ and $dh = 0$, it follows that $V = 0$. Because any u(1)-valued function can be continuously deformed to zero, the term dU can be eliminated by a small gauge transformation. There are still large gauge transformations to consider, which have gauge function with nonzero winding number around some non-trivial loop. To be explicit, for the genus g orientable surface Σ_g, we can take a set of generators of the fundamental group $\bar{\alpha}_n, \bar{\beta}_n, n = 1, \ldots, g$, such that $\#(\bar{\alpha}_n, \bar{\alpha}_m) = 0, \#(\bar{\beta}_n, \bar{\beta}_m) = 0, \#(\bar{\alpha}_n, \bar{\beta}_m) = \delta_{n-m}$, where $\#(,)$ is the algebraic intersection number between two loops. Then there is complete basis of harmonic 1-forms $\omega^{\alpha n}, \omega^{\beta n}$, such that $\oint_{\bar{\alpha}_n} \omega^{\alpha m} = \oint_{\bar{\beta}_n} \omega^{\beta m} = \delta_{n-m}, \oint_{\bar{\alpha}_n} \omega^{\beta m} = \oint_{\bar{\beta}_n} \omega^{\alpha m} = 0$, which implies

$$\int_\Sigma \omega^{\alpha n} \wedge \omega^{\beta m} = \delta_{n-m}, \quad \int_\Sigma \omega^{\alpha n} \wedge \omega^{\alpha m} = \int_\Sigma \omega^{\beta n} \wedge \omega^{\beta m} = 0. \tag{2.40}$$

Since now the field A only has the harmonic part,

$$A = \sum_{n=1}^{g} \left(a_n \omega^{\alpha n} + b_n \omega^{\beta n} \right). \tag{2.41}$$

For $N_{\alpha n}, N_{\beta n} \in \mathbb{Z}$, gauge transformations of the gauge function

$$g(x) = \exp\left[\sum_{n=1}^{g} \mathrm{i}2\pi \left(N_{\alpha n} \int_{x_0}^{x} \omega^{\alpha n} + N_{\beta n} \int_{x_0}^{x} \omega^{\beta n} \right) \right]$$

commute with the small gauge transformations, and are called large gauge transformations. Effectively they translate the variables a_n, b_n by multiples of $\mathrm{i}2\pi$. They form the abelian group $\mathbb{Z}^{2g}$.

Substituting (2.41) into (2.39), the action reduces to

$$\begin{aligned} I_{\mathrm{CS}} &= \frac{k}{4\pi}\int dt \int_\Sigma \sum_{n=1}^{g}\left(a_n\omega^{\alpha n}+b_n\omega^{\beta n}\right)\wedge\partial_t\sum_{n=1}^{g}\left(a_n\omega^{\alpha n}+b_n\omega^{\beta n}\right) \\ &= \frac{k}{2\pi}\int dt\sum_{n=1}^{g}a_n\partial_t b_n. \end{aligned}$$

where (2.40) is used from the first line to the second line. According to the canonical quantization recipe, at this point, there is some freedom in choosing the canonical coordinate and momentum. We will use a real polarization here, in that b_i and $\frac{k}{2\pi}a_i$ are taken as the canonical variables, with the commutation relation $[a_n, b_n] = \frac{-\mathrm{i}2\pi}{k}$, and any other pairs commute.

We shall require the quantum states to transform under LGTs covariantly.Generators of LGTs can be written as $\rho_n = \exp(ka_n)$ and $\sigma_n = \exp(kb_n)$. From the commutator of a_n and b_n, we can find they satisfy the relation

$$\rho_n\sigma_n = \sigma_n\rho_n\exp(k^2[a_n,b_n]) = \sigma_n\rho_n\exp\left(-\mathrm{i}2\pi k\right). \tag{2.42}$$

This is called the clock algebra. When k is not integer-valued, this is a deformed version of the classical commutation relation between ρ_n and σ_n. As a side note, it seems natural to interpret this deformation of algebra as a quantum effect: if one requires the quantum states to form a representation of the original undeformed classical algebra, then k is quantized to be integer-valued. We will not make such requirement in this section, and our results apply to the case of integer-valued k as a special case.

Aside from carrying a representation of the above clock algebra, a quantum state also stores information that is invariant under LGT. The invariant subspace of the phase space is a $2g$-dimensional torus, parameterized by generators of the holonomy group $\alpha_n = \exp\left(\oint_{\bar{\alpha}_n} A\right) = \exp(a_n)$ and $\beta_n = \exp\left(\oint_{\bar{\beta}_n} A\right) = \exp(b_n)$. The non-trivial relation is another clock algebra

$$\alpha_n\beta_n = \beta_n\alpha_n\exp\left(-\frac{\mathrm{i}2\pi}{k}\right). \tag{2.43}$$

These two clock algebras (2.42) and (2.43) can be regarded as being dual to each other, with duality transformation $k \leftrightarrow 1/k$. Note that these two sets of operators commute. For

example, $\alpha_n\sigma_n = \sigma_n\alpha_n \exp(-\mathrm{i}2\pi)$. Thus they realize the statement that on the classical level holonomies are invariant under LGTs.

Since both the LGT group and the holonomy group need to be represented in quantization, and there exists the above interesting duality transformation between them, we like to treat these two groups on an equal footing. This is another reason why k is not restrained to be integer-valued. There is no obvious reason to insist that the holonomy group is un-deformed, so by (2.43), $1/k$ does not need to integer-valued. To exploit the duality, it is better to allow non-integer-valued k as well.

To quantize the theory, we shall look for representations of the algebras (2.42) and (2.43), as well as of the MCG with appropriate induced action on (2.42) and (2.43), so that the quantum states form the left modules of the representations. Because the algebras (2.42) and (2.43) commute with each other, we can look for representations for them separately, and the complete representation is a tensor product.

2.5.2 Quantization on $\Sigma_1 = T^2$

Now we proceed to quantize the theory on a torus. We will use the following topological relations. For a torus, the fundamental group $\pi_1(T^2)$ is abelian and generated by two loops $\bar{\alpha}, \bar{\beta}$, with $\bar{\alpha}\bar{\beta} = \bar{\beta}\bar{\alpha}$. The MCG of the torus, $\mathrm{MCG}(T^2)$ is generated by a pair of Dehn twists, A, B, which can be presented in Figure 2.4 as the loops A, B. The MCG generators act on the the fundamental group generators as

$$\mathsf{A}(\bar{\alpha}, \bar{\beta}) = (\bar{\alpha}, \bar{\beta}\bar{\alpha}), \tag{2.44a}$$

$$\mathsf{B}(\bar{\alpha}, \bar{\beta}) = (\bar{\beta}^{-1}\bar{\alpha}, \bar{\beta}). \tag{2.44b}$$

This group is actually $\mathrm{SL}(2, \mathbb{Z})$, so the relations are

$$\mathsf{ABA} = \mathsf{BAB}, \tag{2.45a}$$

$$(\mathsf{BAB})^4 = 1. \tag{2.45b}$$

Let us consider the representation of holonomy group first. This group is generated

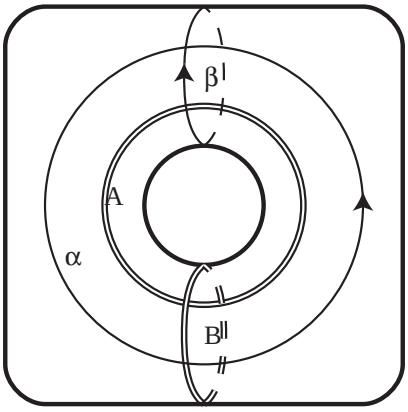

Figure 2.4: Fundamental group generators and MCG generators for Σ_1. The fundamental group generators are denoted by oriented loops with single thin lines, and labeled by Greek letters; the MCG generators are the unoriented loops with double lines, and labeled by Roman letters.

by α and β with $\alpha\beta = \beta\alpha\omega^{-1}$, where $\omega = \exp\left(\frac{\mathrm{i}2\pi}{k}\right)$. We first look for the irreducible representation of this clock algebra.

If $\tilde{\beta}$ and $\tilde{\alpha}$ form a representation of the clock algebra, and $\tilde{\beta}$ is diagonal, their components satisfy

$$\tilde{\alpha}_{ij}\tilde{\beta}_j = \tilde{\beta}_i\tilde{\alpha}_{ij}\omega^{-1}.$$

So if $\tilde{\alpha}_{ij}$ is nonzero, $\tilde{\beta}_i = \omega\tilde{\beta}_j$. A general solution can be written as

$$\tilde{\beta} = \begin{pmatrix} I_{d_0} & & & \\ & \omega I_{d_1} & & \\ & & \ddots & \\ & & & \omega^{p-1} I_{d_{p-1}} \end{pmatrix} e^{\mathrm{i}\theta^\beta}, \quad \tilde{\alpha} = \begin{pmatrix} 0 & & & \hat{\alpha}_{0,p-1} \\ \hat{\alpha}_{10} & 0 & & \\ & \ddots & \ddots & \\ & & \hat{\alpha}_{p-1,p-2} & 0 \end{pmatrix} e^{\mathrm{i}\theta^\alpha},$$

where d_i is the size of each block, and $\hat{\alpha}_{i,i-1}$ is $d_i \times d_{i-1}$ dimensional. But $\tilde{\alpha}$ can be unitary only if $d_0 = d_1 = \cdots = d_{p-1} = d$. While fixing $\tilde{\beta}$, the allowed unitary transformations have

the form $U = \mathrm{diag}\{U_0, \ldots, U_{p-1}\}$, and

$$U^{-1}\tilde{\alpha}U = \begin{pmatrix} 0 & & & U_0^{-1}\hat{\alpha}_{0,p-1}U_{p-1} \\ U_1^{-1}\hat{\alpha}_{10}U_0 & 0 & & \\ & \ddots & \ddots & \\ & & U_{p-1}^{-1}\hat{\alpha}_{p-1,p-2}U_{p-2} & 0 \end{pmatrix} e^{\mathrm{i}\theta^\alpha}.$$

We can take all the U_i's to be the same, but perform such unitary transformation p times. One of the $\hat{\alpha}_{i,i-1}$'s can be diagonalized each time. Finally we get a reducible representation unless $d = 1$.

So in the (not necessarily irreducible) representation where β is diagonal, α, β has the block-diagonal form: (From here on, index of every series starts from 0.)

$$\beta = \mathrm{diag}\{\tilde{\beta}(k, \theta_0^\beta), \ldots, \tilde{\beta}(k, \theta_{r-1}^\beta)\}, \quad \alpha = \mathrm{diag}\{\tilde{\alpha}(k, \theta_0^\alpha), \ldots, \tilde{\alpha}(k, \theta_{r-1}^\alpha)\}, \tag{2.46}$$

where each block forms irreducible representation and is determined by two parameters

$$\tilde{\beta}(k, \theta^\beta) = \begin{pmatrix} 1 & & & \\ & \omega & & \\ & & \ddots & \\ & & & \omega^{p-1} \end{pmatrix} e^{\mathrm{i}\theta^\beta}, \quad \tilde{\alpha}(k, \theta^\alpha) = \begin{pmatrix} 0 & & & 1 \\ 1 & 0 & & \\ & \ddots & \ddots & \\ & & 1 & 0 \end{pmatrix} e^{\mathrm{i}\theta^\alpha}, \tag{2.47}$$

where $\omega = \exp\left(\frac{\mathrm{i}2\pi}{k}\right)$, $k = p/q$ with p, q coprime, and each block in α, β is $p \times p$ dimensional. Note that after taking β to be diagonal, there still remains some unitary transformation on these matrices: while keeping the above form, we can do a cyclic permutation of basis, which changes θ^β by a multiple of $\frac{2\pi}{p}$, and we can shift the phases of the set of basis, which changes θ^α by a multiple of $\frac{2\pi}{p}$. Thus using this unitary transformation, the phase parameters can be restricted as $\theta^\beta, \theta^\alpha \in [0, \frac{2\pi}{p})$.

Next, we find the representations for the MCG generators, whose operation on the holonomies is derived from their classical operation (2.44). The relations that A should satisfy are

$$\mathsf{A}^\dagger \alpha \mathsf{A} = \alpha, \quad \mathsf{A}^\dagger \beta \mathsf{A} = \exp(b + a) = \beta\alpha\omega^{-1/2}. \tag{2.48}$$

where a and b are the coefficients in (2.41) (the subscript is omitted because it can only be 1). To solve these equations, we decompose A into $r \times r$ blocks of $p \times p$ elements as the holonomies. If we focus on the (m, m)-th block of (2.48), we find that the solution is given by

$$\mathsf{A}_{mm} = u^{\mathsf{A}}_{mm} \tilde{\mathsf{A}}(k, \theta^{\alpha}_{m}, \theta^{\mathsf{A}}), \tag{2.49}$$

where u^{A}_{mm} is a complex number, and the components of the $p \times p$ matrix $\tilde{\mathsf{A}}$ are given by

$$\tilde{\mathsf{A}}(k, \theta^{\alpha}_{m}, \theta^{\mathsf{A}})_{ij} = \frac{1}{\sqrt{p}} \omega^{-(i-j)^2/2} e^{\mathrm{i}(i-j)\theta^{\alpha}_{m}} e^{\mathrm{i}\theta^{\mathsf{A}}}. \tag{2.50}$$

The parameter θ^{A}, which does not depend on the block index m, is redundant, because it can be absorbed into u^{A}_{mm}. We keep this seemingly redundant parameter in order to make sure that the matrices $\tilde{\mathsf{A}}$ and $\tilde{\mathsf{B}}$ can form a representation of the MCG (see below). In addition, (2.50) solves the equations (2.48) provided it is periodic with respect to the two indices. Changing i from 0 to p in $\tilde{\mathsf{A}}_{ij}$ gives the condition $\omega^{-p^2/2} e^{\mathrm{i}p\theta^{\alpha}_{m}} = \exp[\mathrm{i}2\pi(-pq/2 + p\theta^{\alpha}_{m}/2\pi)] = 1$. This means if p or q is even, then θ^{α}_{m} are multiples of $\frac{2\pi}{p}$; if p, q are both odd, then θ^{α}_{m} are multiples of $\frac{2\pi}{p}$ plus $\frac{\pi}{p}$. On the other hand, we knew $0 \leq \theta^{\alpha}_{m} < \frac{2\pi}{p}$, so θ^{α}_{m}'s are uniquely determined by k,

$$\theta^{\alpha}_{m} = \frac{\pi}{p} \cdot \Delta, \quad \Delta = \begin{cases} 0, & p \text{ or } q \text{ even}, \\ 1, & p \text{ and } q \text{ odd}. \end{cases} \tag{2.51}$$

After fixing the value of θ^{α}_{m}, we can solve for all blocks of A, and the solution is

$$\mathsf{A}_{mn} = u^{\mathsf{A}}_{mn} \tilde{\mathsf{A}} \left(k, \frac{\pi\Delta}{p}, \theta^{\mathsf{A}} \right). \tag{2.52}$$

In other words, the representations have the form

$$\alpha = I \otimes \tilde{\alpha}(k, \frac{\pi\Delta}{p}), \beta = I \otimes \tilde{\beta}(k, \frac{\pi\Delta}{p}), \mathsf{A} = U^{\mathsf{A}} \otimes \tilde{\mathsf{A}}(k, \frac{\pi\Delta}{p}, \theta^{\mathsf{A}}), \tag{2.53}$$

where U^{A} is any unitary matrix.

For B, the conditions are

$$\mathsf{B}^{\dagger} \alpha \mathsf{B} = \beta^{-1} \alpha \omega^{1/2}, \quad \mathsf{B}^{\dagger} \beta \mathsf{B} = \beta. \tag{2.54}$$

The solution is

$$\mathsf{B}_{mn} = u^{\mathsf{B}}_{mn}\tilde{\mathsf{B}}(k, \theta^{\beta}_{n}, \theta^{\mathsf{B}}), \tag{2.55}$$

where the components of the $p \times p$ matrix $\tilde{\mathsf{B}}$ are given by

$$\tilde{\mathsf{B}}(k, \theta^{\beta}_{n}, \theta^{\mathsf{B}})_{ij} = \omega^{i^2/2} e^{\mathrm{i}i\theta^{\beta}_{n}} \delta_{i-j} e^{\mathrm{i}\theta^{\mathsf{B}}}.$$

By the same periodicity argument, we have

$$\theta^{\beta}_{n} = \theta^{\alpha}_{n} = \frac{\pi}{p} \cdot \Delta, \quad \Delta = \begin{cases} 0, & p \text{ or } q \text{ even}, \\ 1, & p \text{ and } q \text{ odd}. \end{cases} \tag{2.56}$$

Therefor, B also has the form

$$\mathsf{B} = U^{\mathsf{B}} \otimes \tilde{\mathsf{B}}(k, \frac{\pi\Delta}{p}, \theta^{\mathsf{B}}). \tag{2.57}$$

Because the MCG of T^2 is $\mathrm{SL}(2, \mathbb{Z})$, its generators A, B should satisfy the relations $\mathsf{ABA} = \mathsf{BAB}, (\mathsf{BAB})^4 = 1$. Because of the redundant parameters θ^{A} and θ^{B}, we can require that the two parts of direct production in (2.53) and (2.57) satisfy the relations separately. So U^{A} and U^{B} are generators of an arbitrary unitary representation of the MCG. $\tilde{\mathsf{A}}$ and $\tilde{\mathsf{B}}$ are specified by the parameters θ^{A} and θ^{B}, and we need to check how the relations $\mathsf{ABA} = \mathsf{BAB}, (\mathsf{BAB})^4 = 1$ constrain these parameters. For the first relation $\mathsf{ABA} = \mathsf{BAB}$, the right hand side is

$$(\tilde{\mathsf{B}}\tilde{\mathsf{A}}\tilde{\mathsf{B}})_{ij} = \frac{1}{\sqrt{p}} \omega^{i^2/2 + j^2/2 - (i-j)^2/2} e^{\mathrm{i}(i+j)\pi\Delta/p + \mathrm{i}(i-j)\pi\Delta/p} e^{\mathrm{i}(2\theta^{\mathsf{B}} + \theta^{\mathsf{A}})} = \frac{1}{\sqrt{p}} \omega^{ij} e^{\mathrm{i}2i\pi\Delta/p} e^{\mathrm{i}(2\theta^{\mathsf{B}} + \theta^{\mathsf{A}})},$$

and the left-hand side of (2.45a) is

$$\begin{aligned}
(\tilde{\mathsf{A}}\tilde{\mathsf{B}}\tilde{\mathsf{A}})_{ij} =& \frac{1}{p} \sum_{l=0}^{p-1} \omega^{-(i+j-l)^2/2} \omega^{ij} e^{\mathrm{i}(i-j+l)\pi\Delta/p} e^{\mathrm{i}(2\theta^{\mathsf{A}} + \theta^{\mathsf{B}})} \\
=& \frac{1}{p} \sum_{l=0}^{p-1} \omega^{-l^2/2} \omega^{ij} e^{\mathrm{i}(l+2i)\pi\Delta/p} e^{\mathrm{i}(2\theta^{\mathsf{A}} + \theta^{\mathsf{B}})} \\
=& \frac{1}{p} \sum_{l=0}^{p-1} \omega^{-l^2/2 + \Delta l/2q} \omega^{ij} e^{\mathrm{i}2i\pi\Delta/p} e^{\mathrm{i}(2\theta^{\mathsf{A}} + \theta^{\mathsf{B}})}.
\end{aligned}$$

Comparing the two sides, we find a condition for $\theta^{\mathsf{A}}, \theta^{\mathsf{B}}$

$$e^{\mathrm{i}(\theta^{\mathsf{B}}-\theta^{\mathsf{A}})} = \frac{1}{\sqrt{p}} \sum_{l=0}^{p-1} \exp\left(\frac{\mathrm{i}\pi(-ql^2+\Delta l)}{p}\right). \tag{2.58}$$

The right-hand side is a quadratic Gauss sum, for which the summation could be analytically performed. The exact expression will not be presented here. The important fact is, this equation is satisfiable for all possible p and q's (p, q odd, or p even q odd, or p odd q even). It can be checked that the two sides always have the same abstract values, and the phases can be matched by the yet-unknown θ_{A} and θ_{B}.

For the second relation $(\mathsf{BAB})^4 = 1$,

$$\begin{aligned}
(\tilde{\mathsf{B}}\tilde{\mathsf{A}}\tilde{\mathsf{B}})_{ij} =& \frac{1}{\sqrt{p}} \omega^{ij} e^{\mathrm{i}2i\pi\Delta/p} e^{\mathrm{i}(2\theta^{\mathsf{B}}+\theta^{\mathsf{A}})}, \\
((\tilde{\mathsf{B}}\tilde{\mathsf{A}}\tilde{\mathsf{B}})^2)_{ij} =& \frac{1}{p} \sum_{l=0}^{p-1} \omega^{il}\omega^{lj} e^{\mathrm{i}(2i+2l)\pi\Delta/p} e^{\mathrm{i}2(2\theta^{\mathsf{B}}+\theta^{\mathsf{A}})} \\
=& \delta_{(q(i+j)+\Delta) \bmod p} e^{\mathrm{i}2i\pi\Delta/p} e^{\mathrm{i}2(2\theta^{\mathsf{B}}+\theta^{\mathsf{A}})}, \\
((\tilde{\mathsf{B}}\tilde{\mathsf{A}}\tilde{\mathsf{B}})^4)_{ij} =& \delta_{(i-j)} e^{-\mathrm{i}2\pi\Delta q'/p} e^{\mathrm{i}4(2\theta^{\mathsf{B}}+\theta^{\mathsf{A}})},
\end{aligned}$$

where q' satisfies $qq' \equiv 1 \pmod{p}$. So we get the another condition on $\theta^{\mathsf{A}}, \theta^{\mathsf{B}}$

$$e^{-\mathrm{i}2\pi\Delta q'/p} e^{\mathrm{i}4(\theta^{\mathsf{A}}+2\theta^{\mathsf{B}})} = 1. \tag{2.59}$$

The two conditions (2.58) and (2.59) will determine θ^{A} and θ^{B} up to 12 choices, but different choices are equivalent. Actually, if θ^{A} and θ^{B} are a set of solution, then $\theta^{\mathsf{A}}+n\frac{2\pi}{12}$ and $\theta^{\mathsf{B}}+n\frac{2\pi}{12}$ also solve (2.58) and (2.59). The difference between these two set of solutions is nothing but an abelian representation of the MCG, so it can be absorbed into U^{A} and U^{B}.

We still need to find representation for the dual clock algebra (2.42) for LGTs and representation for the action of MCG to the LGTs. But these are exactly the same algebras as those solved above, except k is replaced by $1/k$, or equivalently, p, q are exchanged. Thus the irreducible unitary representation for the dual clock algebra is q-dimensional, phase parameters θ_n^ρ and θ_n^σ are uniquely determined to be $\frac{\pi}{q} \cdot \Delta$, and counterparts of (2.58) and (2.59) give some solution to the phase parameters $\hat{\theta}^{\mathsf{A}}$ and $\hat{\theta}^{\mathsf{B}}$. The full representation for

the algebras is

$$\alpha = I_r \otimes \tilde{\alpha}\left(k, \pi\Delta/p\right) \otimes I_q, \quad \beta = I_r \otimes \tilde{\beta}\left(k, \pi\Delta/p\right) \otimes I_q,$$
$$\rho = I_r \otimes I_p \otimes \tilde{\alpha}\left(1/k, \pi\Delta/q\right), \quad \sigma = I_r \otimes I_p \otimes \tilde{\beta}\left(1/k, \pi\Delta/q\right)$$
$$\mathsf{A} = U^{\mathsf{A}} \otimes \tilde{\mathsf{A}}\left(k, \pi\Delta/p, \theta^{\mathsf{A}}\right) \otimes \tilde{\mathsf{A}}\left(1/k, \pi\Delta/q, \hat{\theta}^{\mathsf{A}}\right), \quad \mathsf{B} = U^{\mathsf{B}} \otimes \tilde{\mathsf{B}}\left(k, \pi\Delta/p, \theta^{\mathsf{B}}\right) \otimes \tilde{\mathsf{B}}\left(1/k, \pi\Delta/q, \hat{\theta}^{\mathsf{B}}\right), \tag{2.60}$$

where I_d is the $d \times d$ identity matrix.

Generalizing the work of [107], in this section, the value of k is not restricted after imposing MCG. However, representing the MCG still affects the representation of the holonomy group and the LGT group, because in this process, the phase parameters θ_n^α and θ_n^β are determined as in (2.56), which are otherwise free to change within $[0, \frac{2\pi}{p})$, and $\theta_n^\rho, \theta_n^\sigma$ are restricted similarly.

2.5.3 Quantization on Σ_2

We now consider quantization of CST on a genus two surface Σ_2. The relevant topological properties of Σ_2 are the following. The fundamental group of Σ_2 has 4 generators $\bar{\alpha}_1, \bar{\beta}_1, \bar{\alpha}_2, \bar{\beta}_2$ with one relation $\bar{\alpha}_1^{-1}\bar{\beta}_1\bar{\alpha}_1\bar{\beta}_1^{-1}\bar{\alpha}_2^{-1}\bar{\beta}_2\bar{\alpha}_2\bar{\beta}_2^{-1} = 1$. The MCG of Σ_2, MCG(Σ_2), is generated by five Dehn twists, $\mathsf{A}_1, \mathsf{B}_1, \mathsf{A}_2, \mathsf{B}_2, \mathsf{S}$, as are drawn in Figure 2.5. Their operation on the loops are derived to be

$$\mathsf{A}_1(\bar{\alpha}_1, \bar{\beta}_1, \bar{\alpha}_2, \bar{\beta}_2) = (\bar{\alpha}_1, \bar{\beta}_1\bar{\alpha}_1, \bar{\alpha}_2, \bar{\beta}_2), \tag{2.61a}$$
$$\mathsf{B}_1(\bar{\alpha}_1, \bar{\beta}_1, \bar{\alpha}_2, \bar{\beta}_2) = (\bar{\beta}_1^{-1}\bar{\alpha}_1, \bar{\beta}_1, \bar{\alpha}_2, \bar{\beta}_2), \tag{2.61b}$$
$$\mathsf{A}_2(\bar{\alpha}_1, \bar{\beta}_1, \bar{\alpha}_2, \bar{\beta}_2) = (\bar{\alpha}_1, \bar{\beta}_1, \bar{\alpha}_2, \bar{\beta}_2\bar{\alpha}_2), \tag{2.61c}$$
$$\mathsf{B}_2(\bar{\alpha}_1, \bar{\beta}_1, \bar{\alpha}_2, \bar{\beta}_2) = (\bar{\alpha}_1, \bar{\beta}_1, \bar{\beta}_2\bar{\alpha}_2^{-1}, \bar{\beta}_2), \tag{2.61d}$$
$$\mathsf{S}(\bar{\alpha}_1, \bar{\beta}_1, \bar{\alpha}_2, \bar{\beta}_2) = (\bar{\alpha}_1\bar{\beta}_1^{-1}\bar{\beta}_2, \bar{\beta}_1, \bar{\beta}_2^{-1}\bar{\beta}_1\bar{\alpha}_2, \bar{\beta}_2), \tag{2.61e}$$

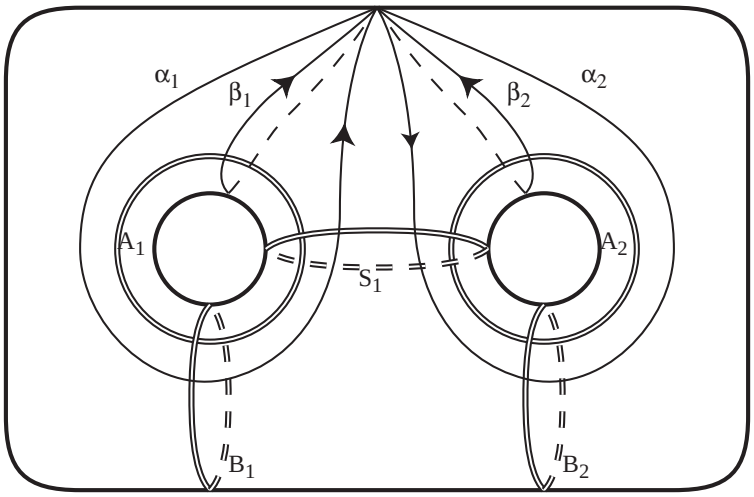

Figure 2.5: Fundamental group generators and MCG generators for Σ_2. The fundamental group generators are denoted by oriented loops with single thin lines, and labeled by Greek letters; the MCG generators are the unoriented loops with double lines, and labeled by Roman letters.

and they satisfy the following relations [111]

$$[[\mathsf{A}_1, \mathsf{A}_2]] = [[\mathsf{A}_1, \mathsf{B}_2]] = [[\mathsf{B}_1, \mathsf{A}_2]] = [[\mathsf{B}_1, \mathsf{B}_2]] = [[\mathsf{B}_1, \mathsf{S}]] = [[\mathsf{B}_2, \mathsf{S}]] = 1, \tag{2.62a}$$

$$\mathsf{A}_1\mathsf{B}_1\mathsf{A}_1 = \mathsf{B}_1\mathsf{A}_1\mathsf{B}_1, \quad \mathsf{A}_2\mathsf{B}_2\mathsf{A}_2 = \mathsf{B}_2\mathsf{A}_2\mathsf{B}_2, \quad \mathsf{A}_1\mathsf{S}\mathsf{A}_1 = \mathsf{S}\mathsf{A}_1\mathsf{S}, \quad \mathsf{A}_2\mathsf{S}\mathsf{A}_2 = \mathsf{S}\mathsf{A}_2\mathsf{S}, \tag{2.62b}$$

$$(\mathsf{B}_1\mathsf{A}_1\mathsf{S})^4 = \mathsf{B}_2^2, \tag{2.62c}$$

$$[[\mathsf{B}_2\mathsf{A}_2\mathsf{S}\mathsf{A}_1\mathsf{B}_1\mathsf{B}_1\mathsf{A}_1\mathsf{S}\mathsf{A}_2\mathsf{B}_2, \mathsf{B}_1]] = 1, \tag{2.62d}$$

$$(\mathsf{B}_2\mathsf{A}_2\mathsf{S}\mathsf{A}_1\mathsf{B}_1\mathsf{B}_1\mathsf{A}_1\mathsf{S}\mathsf{A}_2\mathsf{B}_2)^2 = 1. \tag{2.62e}$$

where $[[\cdot, \cdot]]$ is the group theory commutator defined as $[[g_1, g_2]] \doteq g_1 g_2 g_1^{-1} g_2^{-1}$.

By the conventions shown in Figure 2.5, with $a_i = \int_{\alpha_i} A, b_i = \int_{\beta_i} A$, the Chern-Simons action is

$$I_{\mathrm{CS}} = \frac{k}{2\pi} \int dt (a_1 \partial_t b_1 + a_2 \partial_t b_2)$$

which results in the commutators

$$[a_1, b_1] = [a_2, b_2] = \frac{-\mathrm{i}2\pi}{k}$$

and any other pair commutes.

As in section 2.5.2, let us only consider representation of the holonomy group for now. From the above commutation relations, the holonomy group generators satisfy the clock algebra,

$$\alpha_1\beta_1 = \beta_1\alpha_1\omega^{-1}, \quad \alpha_2\beta_2 = \beta_2\alpha_2\omega^{-1}, \tag{2.63}$$

and any other pair commutes. Similar to section 2.5.2, we have the following equations for the MCG generators,

$$\mathsf{B}_1^\dagger\alpha_1\mathsf{B}_1 = \beta_1^{-1}\alpha_1\omega^{1/2}, \quad \mathsf{B}_2^\dagger\alpha_2\mathsf{B}_2 = \beta_2\alpha_2\omega^{1/2}, \quad \mathsf{A}_1^\dagger\beta_1\mathsf{A}_1 = \beta_1\alpha_1\omega^{-1/2}, \quad \mathsf{A}_2^\dagger\beta_2\mathsf{A}_2 = \beta_2\alpha_2^{-1}\omega^{-1/2},$$

and they commute with the rest of the holonomy group generators.

The equations we have listed so far are just two copies of their counterparts in section 2.5.2, so the solution of the generators is just a direct product of the solutions in section 2.5.2,

$$\begin{aligned}
&\beta_1 = I_r \otimes \tilde{\beta}_1, \quad \beta_2 = I_r \otimes \tilde{\beta}_2, \quad \alpha_1 = I_r \otimes \tilde{\alpha}_1, \quad \alpha_2 = I_r \otimes \tilde{\alpha}_2, \\
&\mathsf{B}_1 = U_1^{\mathsf{B}} \otimes \tilde{\mathsf{B}}_1, \quad \mathsf{B}_2 = U_2^{\mathsf{B}} \otimes \tilde{\mathsf{B}}_2, \quad \mathsf{A}_1 = U_1^{\mathsf{A}} \otimes \tilde{\mathsf{A}}_1, \quad \mathsf{A}_2 = U_2^{\mathsf{A}} \otimes \tilde{\mathsf{A}}_2,
\end{aligned} \tag{2.64}$$

where

$$\begin{aligned}
&\tilde{\beta}_1 = \tilde{\beta}\left(k, \pi\Delta/p\right) \otimes I_p, \quad \tilde{\beta}_2 = I_p \otimes \tilde{\beta}\left(k, \pi\Delta/p\right), \\
&\tilde{\alpha}_1 = \tilde{\alpha}\left(k, \pi\Delta/p\right) \otimes I_p, \quad \tilde{\alpha}_2 = I_p \otimes \tilde{\alpha}\left(k, \pi\Delta/p\right), \\
&\tilde{\mathsf{B}}_1 = \tilde{\mathsf{B}}\left(k, \pi\Delta/p, \theta_1^{\mathsf{B}}\right) \otimes I_p, \quad \tilde{\mathsf{B}}_2 = I_p \otimes \tilde{\mathsf{B}}\left(k, \pi\Delta/p, \theta_2^{\mathsf{B}}\right), \\
&\tilde{\mathsf{A}}_1 = \tilde{\mathsf{A}}\left(k, \pi\Delta/p, \theta_1^{\mathsf{A}}\right) \otimes I_p, \quad \tilde{\mathsf{A}}_2 = I_p \otimes \tilde{\mathsf{A}}\left(k, \pi\Delta/p, \theta_2^{\mathsf{A}}\right).
\end{aligned}$$

The new generator S is determined by the equations

$$\mathsf{S}^\dagger\alpha_1\mathsf{S} = \alpha_1\beta_1^{-1}\beta_2\omega^{-1/2}, \quad \mathsf{S}^\dagger\alpha_2\mathsf{S} = \beta_2^{-1}\beta_1\alpha_2\omega^{1/2}, \quad \mathsf{S}^\dagger\beta_1\mathsf{S} = \beta_1, \quad \mathsf{S}^\dagger\beta_2\mathsf{S} = \beta_2.$$

The solution is

$$\mathsf{S} = U^{\mathsf{S}} \otimes \tilde{\mathsf{S}}(k, \theta^{\mathsf{S}}),$$

where

$$\tilde{\mathsf{S}}(k, \theta^{\mathsf{S}})_{i_1 j_1, i_2 j_2} = \omega^{(i_2 - i_1)^2/2}\delta_{i_1 - j_1}\delta_{i_2 - j_2}e^{\mathrm{i}\theta^{\mathsf{S}}}.$$

This matrix is periodic only if one of p, q are even, that is, $\Delta = 0$. This is a non-trivial "quantization condition" for k on Σ_2. One can see that if we restrict k to be integer-valued, then this condition agree with that in ref. [107], which is that k must be an even integer.

Now we check the relations (2.62a)-(2.62e). Equation (2.62a) is automatically satisfied; (2.62b) gives the same equation as (2.58) except now $\Delta = 0$,

$$e^{\mathrm{i}(\theta_1^{\mathsf{B}}-\theta_1^{\mathsf{A}})} = e^{\mathrm{i}(\theta_2^{\mathsf{B}}-\theta_2^{\mathsf{A}})} = e^{\mathrm{i}(\theta^{\mathsf{S}}-\theta_1^{\mathsf{A}})} = e^{\mathrm{i}(\theta^{\mathsf{S}}-\theta_2^{\mathsf{A}})} = \frac{1}{\sqrt{p}}\sum_{l=0}^{p-1}\exp\left(\frac{-\mathrm{i}\pi q l^2}{p}\right) \tag{2.65}$$

which means $\theta_1^{\mathsf{A}} = \theta_2^{\mathsf{A}}, \theta_1^{\mathsf{B}} = \theta_2^{\mathsf{B}} = \theta^{\mathsf{S}}$, and the two angles θ_1^{A} and θ_1^{B} are related by this equation. So there is really only one free angle parameter left. Consider the relation (2.62c),

$$\begin{aligned}((\tilde{\mathsf{B}}_1\tilde{\mathsf{A}}_1\tilde{\mathsf{S}})^2)_{i_1j_1,i_2j_2} =&\delta_{i_1+j_1-j_2}\delta_{i_2-j_2}\omega^{-j_1j_2+j_2^2}e^{\mathrm{i}2(\theta_1^{\mathsf{B}}+\theta_1^{\mathsf{A}}+\theta^{\mathsf{S}})}\\ ((\tilde{\mathsf{B}}_1\tilde{\mathsf{A}}_1\tilde{\mathsf{S}})^4)_{i_1j_1,i_2j_2} =&\delta_{i_1-j_1}\delta_{i_2-j_2}\omega^{j_2^2}e^{\mathrm{i}4(\theta_1^{\mathsf{B}}+\theta_1^{\mathsf{A}}+\theta^{\mathsf{S}})}.\end{aligned}$$

Equating this with $(\mathsf{B}_2^2)_{i_1j_1,i_2j_2}$ gives

$$e^{\mathrm{i}4(\theta_1^{\mathsf{B}}+\theta_1^{\mathsf{A}}+\theta^{\mathsf{S}})-\mathrm{i}2\theta_2^{\mathsf{B}}} = 1 \tag{2.66}$$

and this will fix all the angles up to 10 choices. Next consider the relation (2.62d),

$$\begin{aligned}(\tilde{\mathsf{B}}_2\tilde{\mathsf{A}}_2\tilde{\mathsf{S}}\tilde{\mathsf{A}}_1\tilde{\mathsf{B}}_1)_{i_1j_1,i_2j_2} =&\frac{1}{p}\omega^{i_1j_1-i_1j_2+i_2j_2}e^{\mathrm{i}(\theta_1^{\mathsf{A}}+\theta_2^{\mathsf{A}}+\theta_1^{\mathsf{B}}+\theta_2^{\mathsf{B}}+\theta^{\mathsf{S}})}\\ (\tilde{\mathsf{B}}_2\tilde{\mathsf{A}}_2\tilde{\mathsf{S}}\tilde{\mathsf{A}}_1\tilde{\mathsf{B}}_1\tilde{\mathsf{B}}_1\tilde{\mathsf{A}}_1\tilde{\mathsf{S}}\tilde{\mathsf{A}}_2\tilde{\mathsf{B}}_2)_{i_1j_1,i_2j_2} =&\delta_{i_1+j_1}\delta_{i_2+j_2}e^{\mathrm{i}2(\theta_1^{\mathsf{A}}+\theta_2^{\mathsf{A}}+\theta_1^{\mathsf{B}}+\theta_2^{\mathsf{B}}+\theta^{\mathsf{S}})}\end{aligned}$$

It can be checked now that this matrix commutes with $\tilde{\mathsf{B}}_1$. Multiplying $\tilde{\mathsf{B}}_1$ from left or from right just adds the factor $\omega^{i_1^2/2}$ or $\omega^{j_1^2/2}$, respectively, and they are the same because of the first delta function. So the relation (2.62d) poses no condition on the angles. The last relation (2.62e) is

$$((\tilde{\mathsf{B}}_2\tilde{\mathsf{A}}_2\tilde{\mathsf{S}}\tilde{\mathsf{A}}_1\tilde{\mathsf{B}}_1\tilde{\mathsf{B}}_1\tilde{\mathsf{A}}_1\tilde{\mathsf{S}}\tilde{\mathsf{A}}_2\tilde{\mathsf{B}}_2)^2)_{i_1j_1,i_2j_2} = \delta_{i_1-j_1}\delta_{i_2-j_2}e^{\mathrm{i}4(\theta_1^{\mathsf{A}}+\theta_2^{\mathsf{A}}+\theta_1^{\mathsf{B}}+\theta_2^{\mathsf{B}}+\theta^{\mathsf{S}})}$$

so

$$e^{\mathrm{i}4(\theta_1^{\mathsf{A}}+\theta_2^{\mathsf{A}}+\theta_1^{\mathsf{B}}+\theta_2^{\mathsf{B}}+\theta^{\mathsf{S}})} = 1 \tag{2.67}$$

Given (2.65) and (2.66), this condition is also redundant. The nontrivial conditions are (2.65) and (2.66), and they have 10 distinct solutions, which are equivalent because the difference between the solutions are merely an abelian representation of the MCG.

By repeating the above calculation with k replaced by $1/k$, we can obtain the representation for the dual algebra satisfied by LGT generators. In particular, the quantization condition for k, which is that one of p, q must be even, is symmetric with respect to p and q, so the dual algebra will not give additional restriction on k.

2.5.4 Quantization on Σ_g, $g \geq 3$

For higher genus surfaces, the fundamental group and MCG of Σ_g with $g \geq 3$ have the following presentation. The fundamental group $\pi_1(\Sigma_g)$ is generated by $2g$ loops $\bar{\alpha}_1, \ldots, \bar{\alpha}_g, \bar{\beta}_1, \ldots, \bar{\beta}_g$, with one relation $\bar{\alpha}_1^{-1}\bar{\beta}_1\bar{\alpha}_1\bar{\beta}_1^{-1}\cdots\bar{\alpha}_g^{-1}\bar{\beta}_g\bar{\alpha}_g\bar{\beta}_g^{-1} = 1$. For $g \geq 3$, MCG have $2g+2$ generators, which are $\mathsf{A}_n, n = 1, \ldots, g$, $\mathsf{S}_n, n = 1, \ldots, g$, and $\mathsf{B}_n, n = 1, 2$, as shown in Fig.2.6. An explicit presentation of MCG is given in [102]. It takes the following form in our convention

$$[[\mathsf{C}, \mathsf{C}']] = 1, \quad \text{when } \#(C, C') = 0, \tag{2.68a}$$

$$\mathsf{C}\mathsf{C}'\mathsf{C} = \mathsf{C}'\mathsf{C}\mathsf{C}', \quad \text{when } \#(C, C') = \pm 1, \quad \text{(braid relation)}, \tag{2.68b}$$

$$(\mathsf{S}_1\mathsf{A}_1\mathsf{B}_1)^4 = \mathsf{E}_0\mathsf{B}_2, \quad \text{(3-chain relation)}, \tag{2.68c}$$

$$\mathsf{E}_2\mathsf{E}_1\mathsf{B}_2 = \mathsf{E}_3\mathsf{S}_2\mathsf{S}_1\mathsf{B}_1, \quad \text{(lantern relation)}, \tag{2.68d}$$

$$[[\mathsf{A}_g\mathsf{S}_{g-1}\mathsf{A}_{g-1}\cdots\mathsf{S}_1\mathsf{A}_1\mathsf{B}_1\mathsf{B}_1\mathsf{A}_1\mathsf{S}_1\cdots\mathsf{A}_{g-1}\mathsf{S}_{g-1}\mathsf{A}_g, \mathsf{B}_g]] = 1, \quad \text{(hyperelliptic relation)}, \tag{2.68e}$$

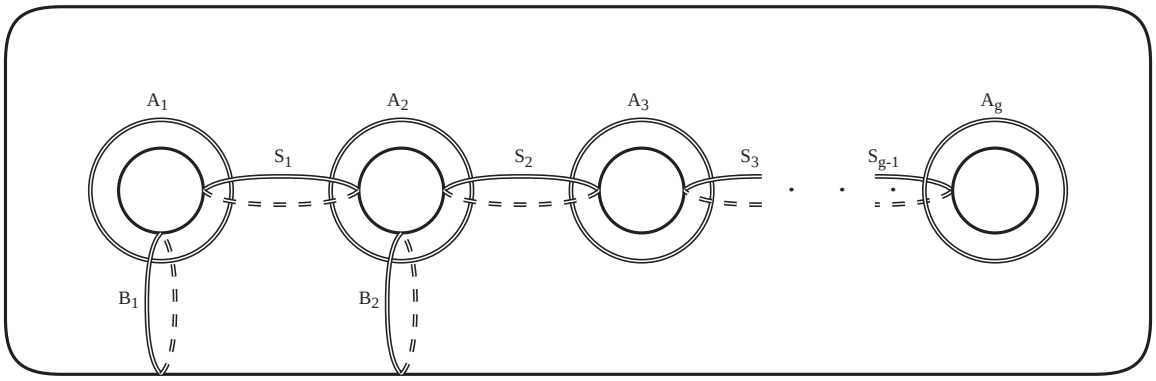

Figure 2.6: MCG generators for $\Sigma_g, g \geq 3$.

where the conventional names of the last four relations are also from [102], and

$$\begin{aligned}
\mathsf{E}_0 =&(\mathsf{A}_2\mathsf{S}_1\mathsf{A}_1\mathsf{B}_1\mathsf{B}_1\mathsf{A}_1\mathsf{S}_1\mathsf{A}_2)\mathsf{B}_2(\mathsf{A}_2\mathsf{S}_1\mathsf{A}_1\mathsf{B}_1\mathsf{B}_1\mathsf{A}_1\mathsf{S}_1\mathsf{A}_2)^{-1},\\
\mathsf{E}_1 =&(\mathsf{A}_2\mathsf{S}_2\mathsf{S}_1\mathsf{A}_2)^{-1}\mathsf{B}_2(\mathsf{A}_2\mathsf{S}_2\mathsf{S}_1\mathsf{A}_2),\\
\mathsf{E}_2 =&(\mathsf{A}_1\mathsf{S}_1\mathsf{B}_1\mathsf{A}_1)^{-1}\mathsf{E}_1(\mathsf{A}_1\mathsf{S}_1\mathsf{B}_1\mathsf{A}_1),\\
\mathsf{E}_3 =&(\mathsf{A}_3\mathsf{S}_2\mathsf{A}_2\mathsf{S}_1\mathsf{A}_1\mathsf{U}\mathsf{B}_1^{-1}\mathsf{A}_1^{-1}\mathsf{S}_1^{-1}\mathsf{A}_2^{-1})\mathsf{B}_2(\mathsf{A}_3\mathsf{S}_2\mathsf{A}_2\mathsf{S}_1\mathsf{A}_1\mathsf{U}\mathsf{B}_1^{-1}\mathsf{A}_1^{-1}\mathsf{S}_1^{-1}\mathsf{A}_2^{-1})^{-1},\\
\mathsf{U} =&(\mathsf{A}_3\mathsf{S}_2)^{-1}\mathsf{E}_1^{-1}(\mathsf{A}_3\mathsf{S}_2),
\end{aligned}$$

and B_{n+2} is computed from $\mathsf{B}_n, \mathsf{B}_{n+1}$ and the generators by induction

$$\mathsf{B}_{n+2} = \mathsf{W}_n\mathsf{B}_n\mathsf{W}_n^{-1}, \tag{2.69}$$

where

$$\mathsf{W}_n = (\mathsf{A}_n\mathsf{S}_n\mathsf{A}_{n+1}\mathsf{B}_{n+1})(\mathsf{S}_{n+1}\mathsf{A}_{n+2}\mathsf{A}_{n+1}\mathsf{S}_{n+1})(\mathsf{S}_n\mathsf{A}_{n+1}\mathsf{A}_n\mathsf{S}_n)(\mathsf{B}_{n+1}\mathsf{A}_{n+1}\mathsf{S}_{n+1}\mathsf{A}_{n+2}).$$

The holonomy group is generated by $2g$ generators α_n, β_n, $n = 1, ldots, g$, and they satisfy the clock algebra in pairs. Representation of the $2g + 2$ MCG generators can also be derived from their actions on the holonomies. The result is

$$\begin{aligned}
&\beta_n = I_r \otimes \tilde{\beta}_n, \quad \alpha_n = I_r \otimes \tilde{\alpha}_n,\\
&\mathsf{A}_n = U_n^{\mathsf{A}} \otimes \tilde{\mathsf{A}}_n, \quad \mathsf{S}_n = U_n^{\mathsf{S}} \otimes \tilde{\mathsf{S}}_n, \quad \mathsf{B}_n = U_n^{\mathsf{B}} \otimes \tilde{\mathsf{B}}_n,
\end{aligned}$$

where

$$\tilde{\beta}_n = I_p^{\otimes n-1} \otimes \tilde{\beta}(k,0) \otimes I_p^{\otimes g-n}, \tag{2.70a}$$

$$\tilde{\alpha}_n = I_p^{\otimes n-1} \otimes \tilde{\alpha}(k,0) \otimes I_p^{\otimes g-n}, \tag{2.70b}$$

$$\tilde{\mathsf{A}}_n = I_p^{\otimes n-1} \otimes \tilde{\mathsf{A}}(k,0,\theta_n^{\mathsf{A}}) \otimes I_p^{\otimes g-n}, \tag{2.70c}$$

$$\tilde{\mathsf{S}}_n = I_p^{\otimes n-1} \otimes \tilde{\mathsf{S}}(k,0,\theta_n^{\mathsf{S}}) \otimes I_p^{\otimes g-n-1}, \tag{2.70d}$$

$$\tilde{\mathsf{B}}_n = I_p^{\otimes n-1} \otimes \tilde{\mathsf{B}}(k,0,\theta_n^{\mathsf{B}}) \otimes I_p^{\otimes g-n}. \tag{2.70e}$$

In this process, we get the same quantization condition on k, which is one of p, q must be even.

We still need to make sure the relations (2.68a)-(2.68e) are satisfied. Equation (2.68a) is trivially satisfied. The braid relations (2.68b) give as before

$$\theta_n^{\mathsf{A}} = \theta^{\mathsf{A}},\ \theta_n^{\mathsf{B}} = \theta_n^{\mathsf{S}} = \theta^{\mathsf{B}},\ e^{\mathrm{i}(\theta^{\mathsf{B}}-\theta^{\mathsf{A}})} = \frac{1}{\sqrt{p}} \sum_{l=0}^{p-1} \exp\left(\frac{-\mathrm{i}\pi q l^2}{p}\right) \tag{2.71}$$

There leaves only one undetermined phase in the MCG generators. The 3-chain relation (2.68c) is

$$(\mathsf{S}_1\mathsf{A}_1\mathsf{B}_1)^4 = (\mathsf{A}_2\mathsf{S}_1\mathsf{A}_1\mathsf{B}_1\mathsf{B}_1\mathsf{A}_1\mathsf{S}_1\mathsf{A}_2)\mathsf{B}_2(\mathsf{A}_2\mathsf{S}_1\mathsf{A}_1\mathsf{B}_1\mathsf{B}_1\mathsf{A}_1\mathsf{S}_1\mathsf{A}_2)^{-1}\mathsf{B}_2$$

Note that every element in this relation has the same form as in the previous section, so those results can be used. From (2.62d), we know that $[[\mathsf{A}_2\mathsf{S}_1\mathsf{A}_1\mathsf{B}_1\mathsf{B}_1\mathsf{A}_1\mathsf{S}_1\mathsf{A}_2, \mathsf{B}_2]] = 1$. By conjugation and commutation, this 3-chain relation (2.68c) reduces to the previously proven relation (2.62c), $(\mathsf{B}_1\mathsf{A}_1\mathsf{S}_1)^4 = \mathsf{B}_2^2$. Regarding the lantern relation (2.68d)

$$\mathsf{E}_2\mathsf{E}_1\mathsf{B}_2 = \mathsf{E}_3\mathsf{S}_2\mathsf{S}_1\mathsf{B}_1,$$

after some calculation, we find

$$\begin{aligned}
(\tilde{\mathsf{E}}_2\tilde{\mathsf{E}}_1\tilde{\mathsf{B}}_2)_{i_1 j_1,\ldots,i_g j_g} =& \omega^{j_1^2+j_2^2+j_3^2-j_1 j_2-j_2 j_3} e^{\mathrm{i}3\theta^{\mathsf{B}}} \delta_{i_1-j_1}\delta_{i_2-j_2}\delta_{i_3-j_3}\cdots \\
(\tilde{\mathsf{E}}_3\tilde{\mathsf{S}}_2\tilde{\mathsf{S}}_1\tilde{\mathsf{B}}_1)_{i_1 j_1,\ldots,i_g j_g} =& \omega^{j_1^2+j_2^2+j_3^2-j_1 j_2-j_2 j_3} e^{\mathrm{i}4\theta^{\mathsf{B}}} \delta_{i_1-j_1}\delta_{i_2-j_2}\delta_{i_3-j_3}\cdots
\end{aligned}$$

so $\theta^{\mathsf{B}} = 0$. This fixes the remaining freedom in the MCG generators. To check the hyperelliptic relation (2.68e),

$$[[\mathsf{A}_g\mathsf{S}_{g-1}\mathsf{A}_{g-1}\cdots\mathsf{S}_1\mathsf{A}_1\mathsf{B}_1\mathsf{B}_1\mathsf{A}_1\mathsf{S}_1\cdots\mathsf{A}_{g-1}\mathsf{S}_{g-1}\mathsf{A}_g,\mathsf{B}_g]] = 1,$$

by (2.69), we find that $\tilde{\mathsf{B}}_n$ takes the form of (2.70e) for all n, and

$$(\tilde{\mathsf{A}}_g\tilde{\mathsf{S}}_{g-1}\tilde{\mathsf{A}}_{g-1}\cdots\tilde{\mathsf{S}}_1\tilde{\mathsf{A}}_1\tilde{\mathsf{B}}_1\tilde{\mathsf{B}}_1\tilde{\mathsf{A}}_1\tilde{\mathsf{S}}_1\cdots\tilde{\mathsf{A}}_{g-1}\tilde{\mathsf{S}}_{g-1}\tilde{\mathsf{A}}_g)_{i_1j_1,\ldots,i_gj_g} = \delta_{i_1+j_1}\cdots\delta_{i_g+j_g}e^{\mathrm{i}g(\theta^{\mathsf{A}}+\theta^{\mathsf{B}})}$$

Obviously this commutes with $\tilde{\mathsf{B}}_g$.

As in the previous section, representation of the dual clock algebra gives no additional quantization condition on k.

2.5.5 Discussion

To summarize our results [2], in this section, we found that the U(1) Chern-Simons theory defined on $\mathbb{R}\times\Sigma_g$ is quantizable, if we required the quantum states to form representations for the deformed holonomy group, the deformed LGT group, and the MCG. Explicit, finite dimensional representations of these groups were found. The parameter k was quantized as follows: on the torus Σ_1, k can take any nonzero rational value, however for Σ_g with $g \geq 2$, k must be a rational number with either its numerator or denominator being even. The representations are unique in the sense that, apart from a choice of arbitrary unitary representation of the MCG, the representations of the discrete groups (holonomy group + LGT group + MCG) are completely fixed.

The uniqueness of the representation of these discrete groups is an interesting result. In general, when one considers gravity with some non-trivial space-time topology, it is expected that some theta angle parameters, or more complicated non-abelian parameters, will arise. But in our toy model, which can be regarded as three dimensional Chern-Simons gravity with gauge group U(1) instead of some non-abelian gauge group [70], although some theta angle parameters appear in representation of the clock algebra, they disappear after representing the MCG.

The representations of the discrete groups on Σ_g are found to be $r(pq)^g$ dimensional, where r is the dimensionality of an arbitrary unitary representation of the MCG, and $k = p/q$ with p, q coprime. This can be compared with the result of the path-integral quantization in Ref. [107], which studied the special case of k being integer-valued. If we take $r = 1$ and k integer-valued, it is easy to check that, the k^g dimensional dimensional representation of the holonomy group from this work is exactly the same representation formed by states in the k^g dimensional Hilbert space found in Ref. [107](see Equation (23) and (24) therein). As a consequence, the representations of MCG in this work and that in Ref. [107] are also the same.

The $r(pq)^g$ dimensional Hilbert space that we find can be viewed as a direct product of g (pq)-dimensional subspaces, and one r-dimensional subspace. Each (pq)-dimensional subspace is associated with one specific handle on Σ_g, and the r-dimensional subspace forms an extra representation of the MCG. Due to this tensor product structure, we can consider pinching of the handles, in which some handles are shrank to marked points. Because the quantization condition on k is stronger for $g \geq 2$ than for $g = 1$, i.e., an allowed k value on a higher genus surface will not pose any problem on a lower genus surface. Without loss of generality, assume the first handle is pinched. The holonomy around the remaining marked points is $\alpha_1\beta_1\alpha_1^{-1}\beta_1^{-1}$, which is the constant number $\exp\left(-\frac{\mathrm{i}2\pi}{k}\right)$ by Equation (2.43). This means in a quantum state, after the pinching, all information about holonomies of the first handle is lost. The same is true for information about LGTs, with the same reason. Thus the $(pq)^g$-dimensional subspace becomes $(pq)^{g-1}$ dimensional after pinching. For the r-dimensional subspace, the situation is more complicated. In general, representations of the MCG of higher genus surface does not reduce to representations of MCG of lower genus surface with marked points, so if pinching is allowed, there may be some extra conditions on the r-dimensional representation of the MCG.

As shown previously in Section 2.5.2, 2.5.3 and 2.5.4, to impose the large gauge symmetry and large diffeomorphisms, it is impossible to simply reduce the original classical phase space to some invariant subspace of these symmetries. However, it is straightforward, at

least classically, to find the invariant phase space under one of the two symmetries. In fact, we chose to represent the large gauge symmetry first, and as a result the $b_1(\Sigma_g)$-dimensional quantum plane, where b_1 is the first Betti number, reduces to a $b_1(\Sigma_g)$-dimensional torus times a $\mathbb{Z}^{b_1(\Sigma_g)}$ lattice, both of which are deformed by the canonical commutator to non-commutative spaces. Wave functions take values on these two parts of phase space separately. Then the implementation of MCG gives some non-trivial and rather technical restrictions on the parameters of the theory, as were listed above.

In principle, the other way around, i.e., to impose MCG first should be equally tractable. Indeed, the invariant subspace is the moduli space of Teichmüller space of Σ_g, and wave functions are sections based upon this moduli space. But presently it is not clear how the wave functions can carry a representation of the large gauge transformations.

2.6 Quantization of U(1) BF theory on non-orientable manifolds

With the results from Section 2.3, we can apply the same methodology in Section 2.5 to the case of non-orientable manifolds, on which a single CST is not well-defined, but the BF theory is well-defined.

The question of quantizing BF theory on non-orientable manifolds has been studied in [89], which is for the case of Σ being the Klein bottle, and the gauge group is taken to be the $2+1$ dimensional Poincaré group $\mathrm{IO}(2,1)$, to match with the corresponding $2+1$ dimensional gravity theory with vanishing cosmological constant. In that paper, it is found that the classical solution space of this model splits into seven components. Four of the components correspond to non-degenerate metrics, and in particular for one component the Klein bottle metric is space-like. Thus quantization on this component will lead to a reasonable quantization of 2+1 dimensional gravity on Klein bottle.

In this section, the quantization will be studied for arbitrary non-orientable surfaces, and explicit quantum states can be found, as long as the explicit presentation of the MCG

is known. As in Section 2.5, we shall take the gauge group to be U(1) for simplicity; the LGT group and holonomy group are required to have projective representations, and the MCG is required to have (non-projective) representations.

2.6.1 General formalism

To find an analogous model with the orientable case we studied before, we consider the BF theory (2.15) with gauge group U(1). With this Abelian gauge group, (2.15) simplifies to

$$I = \frac{k}{2\pi} \int_{\mathbb{R}\times N} B \wedge dA \tag{2.72}$$

where $k = k_{\mathrm{BF0}}$, B is a 1-form-density U(1) gauge field, and A is a regular 1-form U(1) gauge field. By decomposing the fields into time-like components and space-like components, the action becomes

$$I = \frac{k}{2\pi} \int_{N\times\mathbb{R}} \left(B_y \partial_t A_x - B_x \partial_t A_y + B_t F^A_{xy} + A_t F^B_{xy}\right) \tag{2.73}$$

where $F^A_{xy} = \left(\frac{d}{dx}A_y - \frac{d}{dy}A_x\right) dx \wedge dy$, $F^B_{xy} = \left(\frac{d}{dx}B_y - \frac{d}{dy}B_x\right) dx \wedge dy$. By imposing the gauge fixing conditions $A_t = 0, B_t = 0$, and regarding A and B as forms on 2-manifold, the constraint equation is $dA = 0, dB = 0$ (A, B closed). Any classical solution thus can be decomposed as

$$\begin{aligned} A =& dU + \sum a_i \eta^i \\ B =& dV + \sum b_i \xi^i \end{aligned} \tag{2.74}$$

where $\{\eta^i\}(\{\xi^i\})$ is a complete basis of harmonic 1-forms (1-form densities).

The topology of a non-orientable compact surface is specified by the non-orientable genus g, and we denote the surface by N_g. The orientable double cover of N_g is the genus g orientable compact surface Σ_g. Generators of $\pi_1(\Sigma_g)$ can be taken as $\alpha_i, \beta_i, i = 1, \ldots, g$, such that $\#(\alpha_i, \alpha_j) = 0, \#(\beta_i, \beta_j) = 0, \#(\alpha_i, \beta_j) = \pm\delta_{i-j}$, where $\#(,)$ is the algebraic intersection number between two loops. Each loop corresponds to exactly a harmonic form $\omega^{\alpha i}, \omega^{\beta i}$, such that $\int_{\alpha_i} \omega^{\alpha j} = \int_{\beta_i} \omega^{\beta j} = \delta_{i-j}, \int_{\alpha_i} \omega^{\beta j} = \int_{\beta_i} \omega^{\alpha j} = 0$. From these harmonic

forms on Σ_g, one can construct the corresponding harmonic forms and densities on N_g. Forms of the form $\omega^{\alpha i}+\omega^{\alpha g+1-i}$ and $\omega^{\beta i}-\omega^{\beta g+1-i}$ are even forms; $\omega^{\alpha i}-\omega^{\alpha g+1-i}$ and $\omega^{\beta i}+\omega^{\beta g+1-i}$ are odd forms. When g is odd, $\omega^{\alpha(g+1)/2}$ is even, and $\omega^{\beta(g+1)/2}$ is odd. The harmonic forms and densities we found above should be complete, because it can be shown any harmonic form or density on N_g induce a harmonic form on Σ_g, and there are $2g$ harmonic forms on Σ_g, while we already found g harmonic forms and g harmonic densities on N_g. Using these explicit harmonic forms on N_g, we obtain the symplectic structure of the phase space.

The reduced phase space is spanned by a_i, b_i in (2.74). To account for the LGTs, instead of quantizing the u(1)-valued coordinates a_i, b_i, we quantize the U(1)-valued holonomies (see Section 2.5.1)

$$\alpha_\gamma = \exp\left(\oint_{\bar{\gamma}} A\right), \quad \alpha'_\gamma = \exp\left(\oint_{\bar{\gamma}} B\right), \tag{2.75}$$

and the U(1)-valued LGT generators

$$\rho_\gamma = \exp\left(k\oint_{\bar{\gamma}} A\right), \quad \rho'_\gamma = \exp\left(k\oint_{\bar{\gamma}} B\right). \tag{2.76}$$

Classically, the holonomy group and the LGT group formed from these generators are abelian. After quantization however, these two groups are deformed to be non-abelian due to the canonical commutators. Still, these two groups commute with each other, so we can treat with them separately. Their representations are related by the duality transformation $k \leftrightarrow 1/k$. In addition, we require the quantum states to form (un-deformed) representations of the MCG. MCG elements operate on the loops in a definite way, thus their operations on the holonomies and LGTs can be derived accordingly.

The MCG of the Klein bottle MCG(N_1) was found to be $\mathbb{Z}_2 \oplus \mathbb{Z}_2$ in [103]. It was shown in [112] that the MCG of an non-orientable surface can be derived from its oriented double cover, and an explicit presentation of MCG(N_2) was derived there. In Ref. [113] an algorithm was devised to provide an explicit presentation of the MCG for any non-orientable surface, and this was applied to N_3 in [114]. However, the resulting presentation of MCG(N_3) is quite complicated, and we shall not calculate the representation of this

group in the quantization of BF theory. Beyond N_3, no explicit presentation is presently known.

2.6.2 N_1, Klein bottle

For the Klein bottle N_1, the fundamental group is generated by two loops $\bar{\alpha}, \bar{\beta}$, with the relation $\bar{\alpha}\bar{\beta}\bar{\alpha}\bar{\beta}^{-1} = 1$. It has 1 even harmonic form $\eta^1 = \omega^{\alpha 1}$ and 1 odd harmonic form $\xi^1 = \omega^{\beta 1}$, so we define two holonomies

$$\alpha = e^{\int_{\bar{\alpha}} A} = e^a, \ \beta = e^{\int_{\bar{\beta}} B} = e^b. \tag{2.77}$$

From $[b, a] = \frac{-\mathrm{i}2\pi}{k}$, we obtain the clock algebra

$$\alpha\beta = \beta\alpha\omega^{-1} \tag{2.78}$$

The MCG of the Klein bottle is generated by two elements, a Dehn twist A and a cross-cap slide Y. These operations act on the loops $\bar{\alpha}, \bar{\beta}$ as [103]:

$$\mathsf{A}(\bar{\alpha}, \bar{\beta}) = (\bar{\alpha}, \bar{\alpha}\bar{\beta}) \tag{2.79a}$$

$$\mathsf{Y}(\bar{\alpha}, \bar{\beta}) = (\bar{\alpha}^{-1}, \bar{\beta}) \tag{2.79b}$$

It can be checked that $\mathsf{A}^2 = 1, \mathsf{Y}^2 = 1, \mathsf{AY} = \mathsf{YA}$, which confirms the MCG is $\mathbb{Z}_2 \oplus \mathbb{Z}_2$.

The induced operations on the holonomies are

$$\mathsf{A}^\dagger(\alpha, \beta)\mathsf{A} = (\alpha, \beta), \tag{2.80a}$$

$$\mathsf{Y}^\dagger(\alpha, \beta)\mathsf{Y} = (\alpha^{-1}, \beta). \tag{2.80b}$$

Note that although the Dehn twist A maps the loop $\bar{\beta}$ to $\bar{\alpha}\bar{\beta}$, the holonomies are not affected by the operator A. Thus A is just the identity operator, up to a unitary representation U^{A} of the element A in $\mathbb{Z}_2 \oplus \mathbb{Z}_2$.

Because Equation (2.78) is identical to Equation (2.43), the holonomies α and β have the same block-diagonal form,

$$\beta = \mathrm{diag}\{\tilde{\beta}(k, \theta_0^\beta), \ldots, \tilde{\beta}(k, \theta_{r-1}^\beta)\}, \quad \alpha = \mathrm{diag}\{\tilde{\alpha}(k, \theta_0^\alpha), \ldots, \tilde{\alpha}(k, \theta_{r-1}^\alpha)\}, \tag{2.81}$$

with $\theta_i^{\alpha,\beta} \in [0, \frac{2\pi}{p})$.

To solve the equations $\mathsf{Y}^\dagger\beta\mathsf{Y} = \beta, \mathsf{Y}^\dagger\alpha\mathsf{Y} = \alpha^{-1}$, we decompose Y into $r \times r$ blocks of $p \times p$ element as the holonomies. Substituting (2.81) into (2.80b), we find that a solution exists only if $p = 1$ or 2, and when $p = 1$ or 2, the expression for each block of Y is simply

$$\mathsf{Y}_{mn} = u_{mn}\tilde{\mathsf{Y}} = u_{mn}I_p,$$

where u_{mn}^{Y} is complex number. Because $\tilde{\mathsf{Y}} = I_p$ does not depend on the indices m, n, Y can be written as the tensor product form $\mathsf{Y} = U^{\mathsf{Y}} \otimes I_p$, where U^{Y} is a unitary matrix.

The conditions $\mathsf{A}^2 = 1, \mathsf{Y}^2 = 1, \mathsf{AY} = \mathsf{YA}$ are trivially satisfied. Note that in this case of $\Sigma = N_1$, $\theta_i^{\alpha,\beta}$ is not fixed by the MCG.

The representations for the LGT group is just the dual of the representation of the holomony group, with $p \leftrightarrow q$. Thus q can also only take value 1 or 2, i.e., k is quantized to be 1/2, 1 or 2. The full representation of these discrete groups is

$$\begin{aligned}
&\alpha = U^\alpha \otimes \tilde{\alpha}(k,0) \otimes I_q, \quad \beta = U^\beta \otimes \tilde{\beta}(k,0) \otimes I_q, \\
&\rho = U^\rho \otimes I_p \otimes \tilde{\alpha}\left(1/k,0\right), \quad \sigma = U^\sigma \otimes I_p \otimes \tilde{\beta}\left(1/k,0\right), \\
&\mathsf{A} = U^{\mathsf{A}} \otimes I_p \otimes I_q, \quad \mathsf{Y} = U^{\mathsf{Y}} \otimes I_p \otimes I_q,
\end{aligned} \tag{2.82}$$

where U^{A} and U^{Y} form a unitary representation of the generators of the MCG $\mathbb{Z}_2 \oplus \mathbb{Z}_2$, U^α, U^β are diagonal unitary matrices such that

$$\begin{aligned}
(U^{\mathsf{A}})^\dagger(U^\alpha, U^\beta)U^{\mathsf{A}} &= (U^\alpha, U^\beta) \\
(U^{\mathsf{Y}})^\dagger(U^\alpha, U^\beta)U^{\mathsf{Y}} &= ((U^\alpha)^{-1}, U^\beta),
\end{aligned}$$

and similarly for U^ρ, U^σ.

2.6.3 N_2

According to the general formalism in Section 2.6.1, the closed 1-form A and the closed 1-form density B on N_2 can be decomposed as

$$\begin{aligned}
A =& dU + a_1(\omega^{\alpha 1} + \omega^{\alpha 2}) + a_2(\omega^{\beta 1} - \omega^{\beta 2}), \\
B =& dV + b_1(\omega^{\beta 1} + \omega^{\beta 2}) + b_2(\omega^{\alpha 1} - \omega^{\alpha 2}),
\end{aligned}$$

and thus the canonical commutators are $[b_1, a_1] = [a_2, b_2] = \frac{-\mathrm{i}2\pi}{k}$. We define the holonomies as

$$\begin{aligned} \alpha_1 &= e^{\int_{\tilde{\alpha}} B} = e^{b_2},\ \beta_1 = e^{\int_{\tilde{\beta}} A} = e^{a_2}, \\ \alpha_2 &= e^{\int_{\tilde{\alpha}} A} = e^{a_1},\ \beta_2 = e^{\int_{\tilde{\beta}} B} = e^{b_1}. \end{aligned} \tag{2.83}$$

Then again we find the clock algebra $\alpha_n\beta_n = \beta_n\alpha_n\omega$, $n = 1, 2$. The clock algebra representation can be written as

$$\begin{aligned} \beta_1 =& \mathrm{diag}\{\tilde{\beta}(k, \theta_0^{\beta 1}) \otimes I_p, \ldots, \tilde{\beta}(k, \theta_{r-1}^{\beta 1}) \otimes I_p\} \\ \alpha_1 =& \mathrm{diag}\{\tilde{\alpha}(k, \theta_0^{\alpha 1}) \otimes I_p, \ldots, \tilde{\alpha}(k, \theta_{r-1}^{\alpha 1}) \otimes I_p\} \\ \beta_2 =& \mathrm{diag}\{I_p \otimes \tilde{\beta}(k, \theta_0^{\beta 2}), \ldots, I_p \otimes \tilde{\beta}(k, \theta_{r-1}^{\beta 2})\} \\ \alpha_2 =& \mathrm{diag}\{I_p \otimes \tilde{\alpha}(k, \theta_0^{\alpha 2}), \ldots, I_p \otimes \tilde{\alpha}(k, \theta_{r-1}^{\alpha 2})\} \end{aligned}$$

The MCG generators act on the loops as [112]

$$\begin{aligned} \mathsf{A}(\bar{\alpha}, \bar{\beta}) =& (\bar{\alpha}, \bar{\beta}\bar{\alpha}), \\ \mathsf{B}(\bar{\alpha}, \bar{\beta}) =& (\bar{\beta}^{-1}\bar{\alpha}, \bar{\beta}), \\ \mathsf{Y}(\bar{\alpha}, \bar{\beta}) =& (\bar{\alpha}^{-1}, \bar{\beta}), \end{aligned}$$

and they have the relations $\mathsf{ABA} = \mathsf{BAB}, (\mathsf{BAB})^4 = 1, \mathsf{Y}^2 = 1, \mathsf{YAY} = \mathsf{A}^{-1}, \mathsf{YBY} = \mathsf{B}^{-1}$. Their induced operations on holonomies are

$$\begin{aligned} \mathsf{A}^\dagger(\alpha_1, \beta_1, \alpha_2, \beta_2)\mathsf{A} =& (\alpha_1, \beta_1\alpha_2, \alpha_2, \beta_2\alpha_1), \\ \mathsf{B}^\dagger(\alpha_1, \beta_1, \alpha_2, \beta_2)\mathsf{B} =& (\beta_2^{-1}\alpha_1, \beta_1, \beta_1^{-1}\alpha_2, \beta_2), \\ \mathsf{Y}^\dagger(\alpha_1, \beta_1, \alpha_2, \beta_2)\mathsf{Y} =& (\alpha_1^{-1}, \beta_1, \alpha_2^{-1}, \beta_2). \end{aligned}$$

To find representations of the MCG, we again decompose A, B and Y into $r \times r$ blocks of $p \times p$ elements. Let us first focus on the (m, m)-th block. A_{mm} and B_{mm} have the solution

$$\begin{aligned} \mathsf{B}_{mm} =& u_{mm}^{\mathsf{B}} \tilde{\mathsf{B}}\left(k, \theta_m^{\beta 1}, \theta_m^{\beta 2}, \theta^{\mathsf{B}}\right), \\ \mathsf{A}_{mm} =& u_{mm}^{\mathsf{A}} \tilde{\mathsf{A}}\left(k, \theta_m^{\alpha 1}, \theta_m^{\alpha 2}, \theta^{\mathsf{A}}\right), \end{aligned}$$

where

$$\begin{aligned} \tilde{\mathsf{B}}\left(k, \theta_m^{\beta 1}, \theta_m^{\beta 2}, \theta^{\mathsf{B}}\right)_{i_1 j_1, i_2 j_2} =& \omega^{-i_1 i_2} e^{-\mathrm{i}(i_1\theta_m^{\beta 2} + i_2\theta_m^{\beta 1})} \delta_{i_1 - j_1} \delta_{i_2 - j_2} e^{\mathrm{i}\theta_{\mathsf{B}}} \\ \tilde{\mathsf{A}}\left(k, \theta_m^{\alpha 1}, \theta_m^{\alpha 2}, \theta^{\mathsf{A}}\right)_{i_1 j_1, i_2 j_2} =& \frac{1}{d} \omega^{(i_1 - j_1)(i_2 - j_2)} e^{-\mathrm{i}[(i_1 - j_1)\theta_m^{\alpha 2} + (i_2 - j_2)\theta_m^{\alpha 1}]} e^{\mathrm{i}\theta_A} \end{aligned}$$

The unitarity of $\tilde{\mathsf{A}}$ and $\tilde{\mathsf{B}}$ enforces that $d = p$, and the periodicity of $\tilde{\mathsf{A}}$ and $\tilde{\mathsf{B}}$ enforces that $\theta_m^{\beta 1}, \theta_m^{\beta 2}, \theta_m^{\alpha 1}, \theta_m^{\alpha 2}$ are all multiples of $2\pi/p$, so we can take them all to be 0. Note that unlike the case of $\Sigma = \Sigma_2$, in this process the value of k is not restricted. After fixing these phase parameters, it is then straightforward to solve for all blocks of A, B,

$$\begin{aligned}\mathsf{B} =& U^{\mathsf{B}} \otimes \tilde{\mathsf{B}}\left(k, 0, 0, \theta^{\mathsf{B}}\right), \\ \mathsf{A} =& U^{\mathsf{A}} \otimes \tilde{\mathsf{A}}\left(k, 0, 0, \theta^{\mathsf{A}}\right),\end{aligned}$$

where U^{B} and U^{A} are arbitrary r-dimensional unitary matrices.

The relation $\mathsf{ABA} = \mathsf{BAB}$ gives $\theta^{\mathsf{A}} = \theta^{\mathsf{B}}$. Note that in this case no quadratic Gauss sum is involved in the equation. The relation $(\mathsf{BAB})^4 = 1$ gives $e^{\mathrm{i}12\theta^{\mathsf{B}}} = 1$.

However, when solving for Y, it turns out that solution exists only if $p = 1$ or 2, and $\mathsf{Y} = \pm I_p \otimes I_p$, $\theta^{\mathsf{A}} = \theta^{\mathsf{B}} = 0$ or π. As the previous cases, these choices of phases can be absorbed into the abelian representation of the MCG, which leaves the part of MCG representation that interacts with the holonomy group trivial when $p = 1$, and

$$\tilde{\mathsf{B}} = \begin{pmatrix} 1 & 0 & 0 & 0 \\ 0 & 1 & 0 & 0 \\ 0 & 0 & 1 & 0 \\ 0 & 0 & 0 & -1 \end{pmatrix}, \quad \tilde{\mathsf{A}} = \frac{1}{2}\begin{pmatrix} 1 & 1 & 1 & -1 \\ 1 & 1 & -1 & 1 \\ 1 & -1 & 1 & 1 \\ -1 & 1 & 1 & 1 \end{pmatrix}, \quad \tilde{\mathsf{Y}} = \begin{pmatrix} 1 & 0 & 0 & 0 \\ 0 & 1 & 0 & 0 \\ 0 & 0 & 1 & 0 \\ 0 & 0 & 0 & 1 \end{pmatrix}$$

when $p = 2$.

As for the representation of LGT and the part of MCG interacting with LGT, the same result can be found, with $p \leftrightarrow q$. Thus when $\Sigma = N_2$, the quantization condition for k is that k can take value among $1/2$, 1 and 2.

2.6.4 Discussion

To summarize the results in this section, we applied the formalism developed in Section 2.3, and quantized U(1) BF theory defined on $\mathbb{R} \times N_g$, where N_g is the non-orientable surface whose orientable double cover is Σ_g. In this process, the holonomy group and the LGT group are deformed according to the canonical commutation relation, while the MCG

is not deformed. For the cases $g = 1, 2$, for which explicit, tractable presentations of MCG are known, we found explicit, finite dimensional representation of the discrete groups. In order to consistently quantize the system, k are restricted to be either 1/2, 1 or 2. For the Klein bottle N_1, the phase parameters associated the holonomy group generators and the LGT group generators are not totally fixed by the value of k; for the non-orientable surface N_2, similar with the cases of orientable surfaces Σ_g, these phase parameters are fixed by k. For higher g, because no tractable presentation of the MCG is known, the representations of the MCG have not been calculated. However, if we do not require that the MCG is promoted into quantum operators, then the representations of the holonomy group and the LGT group can be directly generalized to cases of higher g.

Similar with the comments in Section 2.5.5, for U(1) BF theory defined on $\mathbb{R} \times N_g$, one can consider pinching of the topological structures, because the representations that we found have tensor product structure; because the phase parameters are fully fixed for the case of N_2, it is interesting to consider the implication on a quantum gravity model defined on $\mathbb{R} \times N_2$.

In addition, we note that the quantum states on the non-orientable manifolds are not simply the quantum states on the oriented double cover with the correct parity. For example, on N_1 and N_2, when k does not take value among 1/2, 1 or 2, there is no quantum state consistent with a representation of the MCG, while on Σ_1 and Σ_2, k can take any rational value with the numerator or the denominator being even, and quantum states with any parity can be constructed. This extra restriction on k is due to non-trivial effects from the quantization of the MCG. In particular, in the calculation in Section 2.6.3, representing the Dehn twists A and B does not introduce this extra quantization condition. It is only when we calculate the representation of the Y-homeomorphism Y that the quantization condition appears.

Chapter 3

Future directions

3.1 Introduction: finite size scaling of systems with first-order phase transition

In Chapter 1, the finite size scaling (FSS) method is applied to the numerical result of the graph model. In Figure 1.10, the inverse transition temperature is plotted as a function of system size N_V, from which it is derived that the transition temperature in the thermodynamic limit is zero. Moreover, the energy distributions of different N_V's are plotted in Figure 1.11. Given enough numerical data, in principle how the energy distribution depends on N_V, i.e., a FSS model of the distribution, can be deduced. Such a FSS model can facilitate our understanding of the macroscopic properties of the graph model.

More generally, the FSS method is a very useful tool in understanding results from physics systems with finite sizes. A phase transition is only strictly well-defined in the thermodynamic limit, for which the system size is infinite. For a finite size system, which is usually studied numerically, the free energy in the canonical ensemble is an analytic function of the temperature. In addition to smoothing out the singularities at transition, finite sizes can also affect other observed quantities non-trivially. The FSS method extrapolates the results with different finite sizes, and thus can make predictions in the thermodynamic limit.

For systems with second-order transition, the FSS method is particularly powerful (see, e.g., [28]). Near a second-order transition point, the correlation length ξ diverges in the thermodynamic limit, but with a finite size, it is bounded above by L, which is the typical

length the finite size. From this observation, it can be derived how other diverging quantities depend on L, and then the critical exponents can be determined by fitting the numerical results.

Systems with first-order transition on the other hand do not show such universality, and as a consequence, there are more open questions regarding how FSS should be performed. In this chapter, we will consider a wide range of the statistical models, including the Potts model [115], a structure-based model for protein folding known as the Gō model [116, 117], and the graph model in Chapter 1 [1], all of which possess a first-order phase transition. We will attempt to find FSS models for these models. If for such a diverse set of models, there are some common features in the FSS models, then these features will likely hold true for other physics models.

3.2 Physics models and numerical results

In this section, the definitions of the three physics models are reviewed, and for each model, numerical simulations are performed in preparation for FSS.

3.2.1 The Potts model

The Potts model [115] is a generalization of the Ising model. (For a review of the Potts model, see [118].) In the Ising model, at each site, the spin has two possible states, while in the Potts model, each spin can take q different states. The Hamiltonian of the Potts model is

$$H = -J \sum_{\langle ij \rangle} \delta_{\sigma_i, \sigma_j}, \tag{3.1}$$

where the summation is over all adjacent pairs of spins, σ_i denotes the spin at site i, δ is the Kronecker delta function, and J is the coupling constant.

The Potts model possesses a phase transition between a high temperature, disordered phase and a low temperature, ordered phase. In the following, this transition will be studied on a two-dimensional square lattice. In this setup, the transition is second-order for $q \leq 4$,

and first-order for $q > 4$ [119]. The transition temperature is given by [119]

$$T_c = \frac{J}{k_B}[\ln(1+\sqrt{q})]^{-1}. \tag{3.2}$$

In our simulations, the finite systems are taken to have size $L \times L$, with periodic boundary conditions. The transition temperature $T_c(L)$ for a finite system is defined to be the temperature that maximizes the heat capacity $C = T^{-2}(\langle E^2 \rangle - \langle E \rangle^2)$.

For $L = 10, 15, 20, 30, 40, 50, 60$ and 70, the (rescaled) energy distribution at $T_c(L)$ is shown in Figure 3.1(a), and $\langle E \rangle / L^2$ and C/L^4 are plotted as functions of $\Delta\beta L^2 = [T^{-1} - (T_c(L))^{-1}]L^2$ in Figure 3.1(b) and (c), respectively. As L increases, the curves in Figure 3.1(b) and (c) converges. This is actually true for any extensive system with first-order transition, because in the thermodynamic limit, the energy density distribution always becomes the sum of two delta functions, and the curves plotted in Figure 3.1(b) and (c) become two universal curves.

3.2.2 Structure-based model for protein folding

Numerical simulations of protein folding is a challenging problem. Compared with those derived from first principles, structure-based models for protein folding [120] are easier to implement. In structure-based models, the native state, i.e., the properly folded, functional state, of a protein is used in constructing the Hamiltonian, such that the native state is the global energy minimum.

The Gō model [116, 117] is one of the structure-based models for protein folding. In this model, hydrogen atoms are ignored. Each heavy atom is represented by a bead of unit mass and radius r_b. Two atom are called "in contact" if: 1. there are at least three residues between these two atoms; 2. in the native state, the two atoms are within the cutoff distance r_c; 3. in the native state, there is no atom between the two atoms spatially.

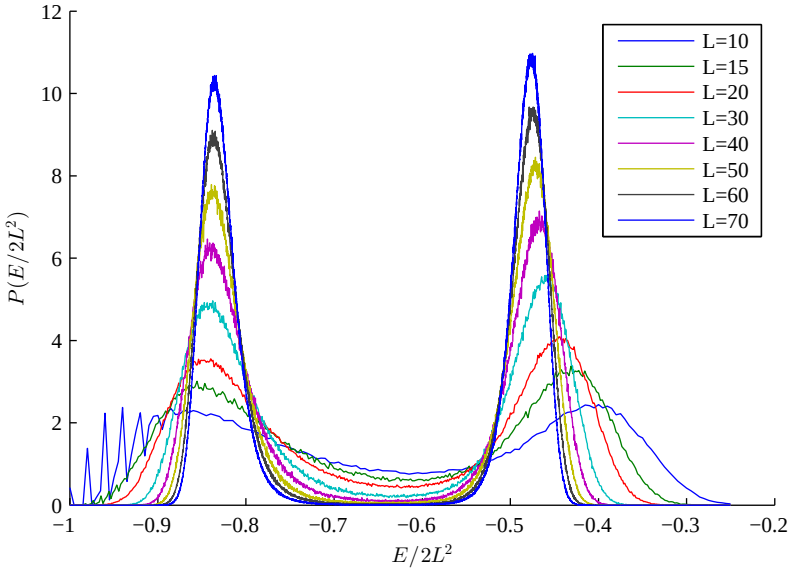

(a)

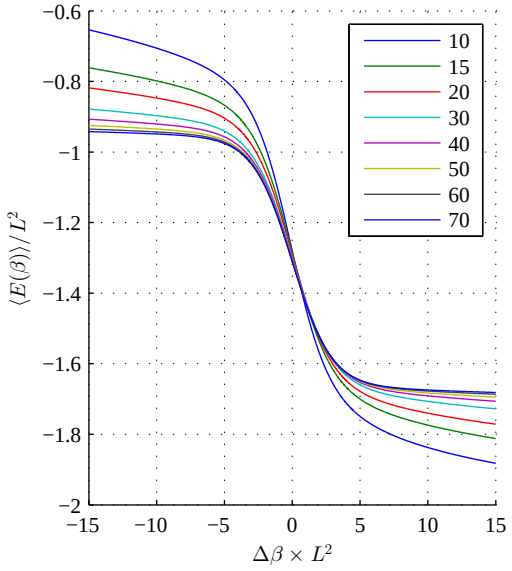

(b)

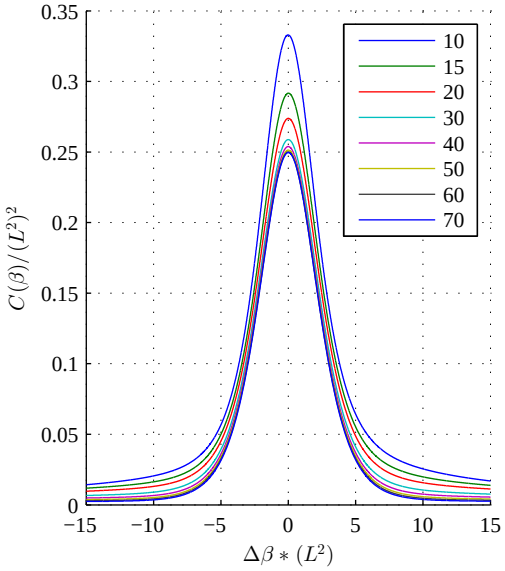

(c)

Figure 3.1: Simulation results of the Potts model. (a) The energy distributions at $T_c(L)$; (b) the rescaled energy expectation value as a function of $\Delta\beta \cdot L^2$. (c) the rescaled heat capacity as a function of $\Delta\beta \cdot L^2$.

The Hamiltonian is

$$\begin{aligned} H = &\sum_{\text{bonds}} \epsilon_r (r - r_0)^2 + \sum_{\text{angles}} \epsilon_\theta (\theta - \theta_0)^2 + \sum_{\text{improper/planar}} \epsilon_\chi (\chi - \chi_0)^2 \\ &+ \sum_{\text{backbone}} \epsilon_{\text{BB}} F_D(\phi) + \sum_{\text{sidechains}} \epsilon_{\text{SC}} F_D(\phi) \\ &+ \sum_{\text{contacts}} \epsilon_{\text{C}} \left[\left(\frac{\sigma_{ij}}{r} \right)^{12} - 2 \left(\frac{\sigma_{ij}}{r} \right)^{6} \right] + \sum_{\text{non-contacts}} \epsilon_{\text{NC}} \left(\frac{\sigma_{\text{NC}}}{r} \right)^{12} \end{aligned} \tag{3.3}$$

where

$$F_D = [1 - \cos(\phi - \phi_0)] + \frac{1}{2} [1 - \cos(3(\phi - \phi_0))]$$

and $\epsilon_r = 100$, $\epsilon_\theta = 20$, $\epsilon_\chi = 10$, $\epsilon_{\text{NC}} = 0.01$, and $\sigma_{\text{NC}} = 2.5\mathring{A}$. r_0, θ_0, χ_0 and σ_{ij} are given by the values measured in the native state. We take $r_b = 1.0\mathring{A}$ and $r_c = 6.0\mathring{A}$. The bonds, angles, improper/planar, backbone and sidechains that are summed over are all identified in the native state, and appropriate potentials are associated with them to favor the native state geometry. A Lennard-Jones potential is added to a pair of atoms that are in contact. Finally, a repulsive power-12 potential is assigned to a pair of atoms that are neither bonded nor in contact. See [116, 117] for more details.

Simulations are performed for eight two-state folders, i.e., proteins that have only two distinct macroscopic states. The rescaled energy distributions at the transition temperature are shown in Figure 3.2(a). The rescaled energy expectation value and the rescaled heat capacity are shown in Figure 3.2(b) and (c) as functions of $\Delta\beta L = [T^{-1} - T_c^{-1}]L$, where L is the number of amino acids in the protein, and T_c is defined for each protein as the temperature that maximize the heat capcity.

3.2.3 The graph model of emergent manifold

The graph model of emergent manifold is defined in Chapter 1. For the three largest sizes $N_V = 1000, 1500$ and 2000, the energy distributions at the transition temperature are plotted in Figure 1.11. The energy expectation value and heat capacity as functions of $\Delta\beta \cdot N_V = [T^{-1} - (T_c(N_V))^{-1}]N_V$ are plotted in Figure 3.3.

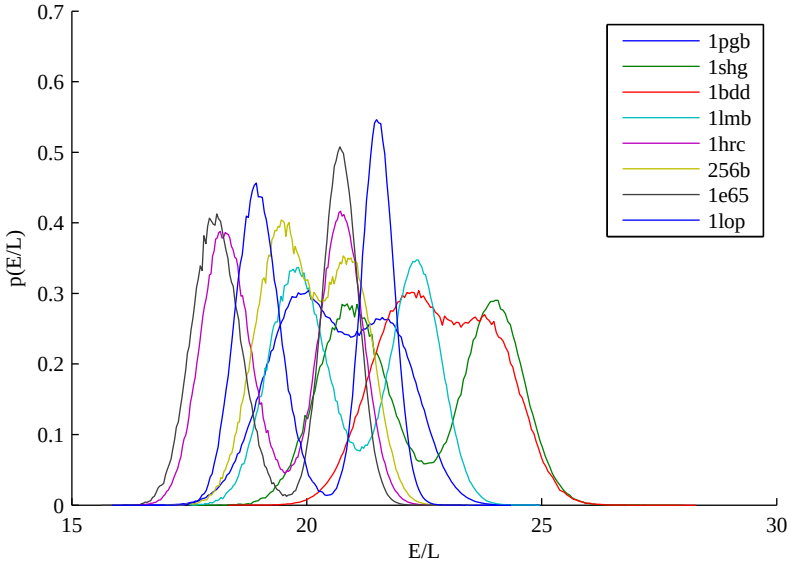

(a)

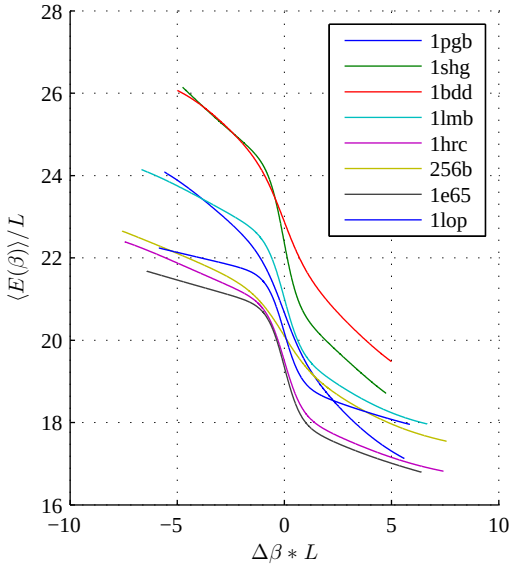

(b)

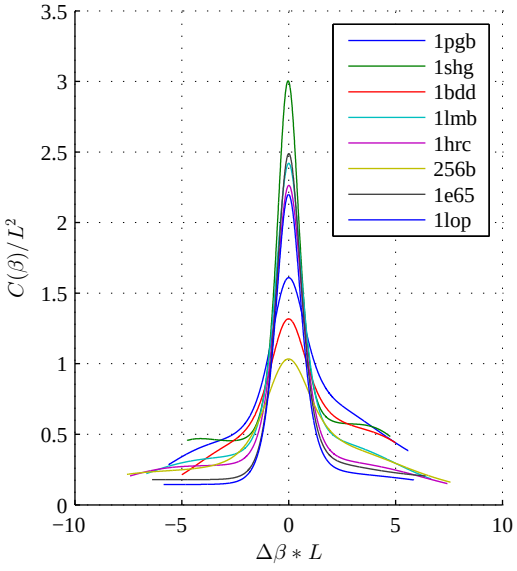

(c)

Figure 3.2: Simulation results for the protein folding model. (a) The rescaled energy distributions at the transition temperature; (b) the rescaled energy expectation value as a function of $\Delta\beta \cdot L$. (c) the rescaled heat capacity as a function of $\Delta\beta \cdot L$.

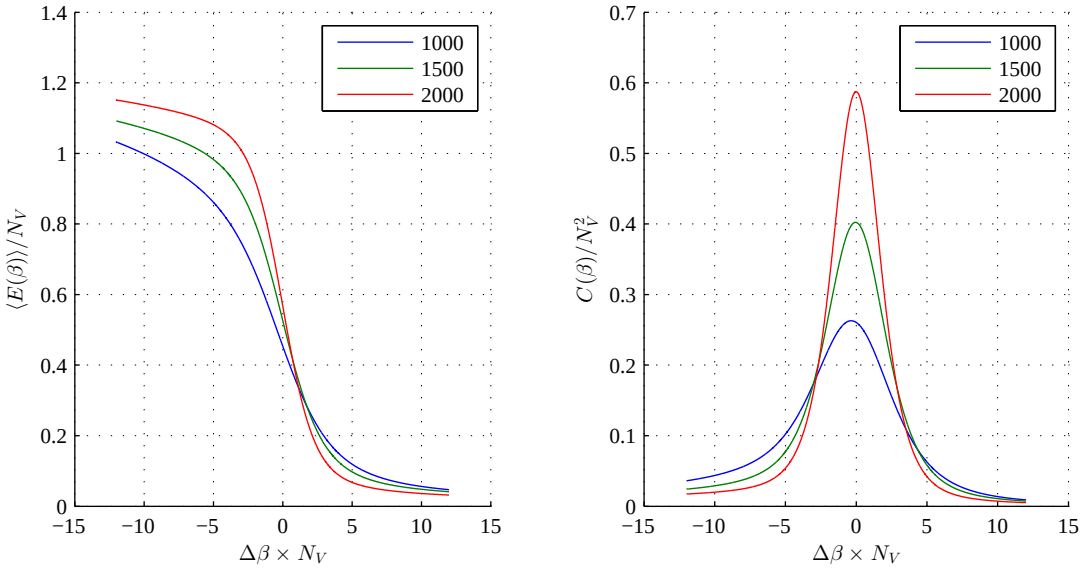

(a) (b)

Figure 3.3: Simulation results of the graph model. (a) the rescaled energy expectation value as a function of $\Delta\beta \cdot N_V$. (b) the rescaled heat capacity as a function of $\Delta\beta \cdot N_V$.

3.3 Finite size scaling models

In this section, we will test a series of FSS models on the above physics models. Each FSS model is motivated by features of some physics model near the transition point.

3.3.1 Sum of two Gaussian functions

In [121], near the transition temperature of a first-order phase transition, the energy distribution is modeled by the sum of two Gaussian functions, and this FSS model is tested for the Potts model described in section 3.2.1. This form of energy distribution can be motivated as follows. When the system size is large enough, the phase-coexisting states can be ignored (see also the capillarity model in Section 3.3.4). For a state composed of one phase, the correlation length of the field is finite, and the system can be viewed as being composed of independent sub-systems. When the system size is large enough, and consequently the number of sub-systems is large enough, by the central limit theorem, the total energy distribution approaches a Gaussian distribution. Near the transition temperature, states of either phase can be observed in the thermodynamic ensemble, so the energy distribution is taken to be the sum of two Gaussian functions.

The energy distribution at T_c is assumed to be,

$$P(e, T_c) = A \left\{ \exp\left[\frac{-(e-e_1)^2 V}{2T_c^2 c_1}\right] + \exp\left[\frac{-(e-e_2)^2 V}{2T_c^2 c_2}\right] \right\}, \tag{3.4}$$

where V is the volume of the system, $e = E/V$ is the intensive energy, and $e_{1,2}$ and $c_{1,2}$ are volume-independent constants. The two Gaussian functions have the same amplitude, because at T_c, the two phases have the same intensive free energy.

At a different temperature, the distribution is

$$P(e, T_c+\Delta T) \simeq A(\Delta T) \left\{ \frac{a_1}{c_1^{1/2}} \exp\left[\frac{-(e-(e_1+c_1\Delta T))^2 V}{2T_c^2 c_1}\right] + \frac{a_2}{c_2^{1/2}} \exp\left[\frac{-(e-(e_2+c_2\Delta T))^2 V}{2T_c^2 c_2}\right] \right\} \tag{3.5}$$

where $A(\Delta T)$ is the normalization factor, $a_1 = c_1^{1/2} e^X, a_2 = c_2^{1/2} e^{-X}$,

$$X = \frac{(e_1 - e_2)\Delta T V}{2T_c^2}. \tag{3.6}$$

and terms of order $(\Delta T/T)^2$ are ignored.

The following thermodynamic quantities can be computed,

$$\langle E\rangle = V\cdot\frac{a_1(e_1+c_1\Delta T)+a_2(e_2+c_2\Delta T)}{a_1+a_2} \tag{3.7}$$

$$\left\langle E^2\right\rangle = V^2\left[\frac{a_1(e_1+c_1\Delta T)^2+a_2(e_2+c_2\Delta T)^2}{a_1+a_2}+\frac{T_c^2}{V}\frac{a_1c_1+a_2c_2}{a_1+a_2}\right] \tag{3.8}$$

$$C\simeq\frac{1}{T_c^2}\left(\left\langle E^2\right\rangle-\langle E\rangle^2\right)=V\cdot\frac{a_1c_1+a_2c_2}{a_1+a_2}+V^2\cdot\frac{a_1a_2\left[e_1-e_2+(c_1-c_2)\Delta T\right]^2}{T_c^2(a_1+a_2)^2}. \tag{3.9}$$

If $c_{1,2}=0$, i.e., and the energy distribution is the sum of two delta functions, then $\langle E\rangle$ and C obey simple universal scaling laws, which is observed and tested numerically for the Potts model in [121]. If we keep $c_\pm$ nonzero, there is no simple universal scaling laws for $\langle E\rangle$ and C.

Figure 3.4 shows the fitting results for the Potts model, which become better for larger system sizes. As can be seen from this figure, the energy distribution of one phase is not left-right symmetric, and the probability between the two Gaussian peaks are too large to be fitted well by the Gaussian functions. In Section 3.3.2 and Section 3.3.4, two improved FSS models are proposed to address these issues.

It turns out that this FSS model works very well for the results of the protein folding model. The fittings to the energy distributions are plotted in Figure 3.5(a), and values of the fitting parameters are shown in Figure 3.5(b). From Figure 3.5(b), one can see that although e_1 and e_2 vary for different proteins, the quantities e_2-e_1 is relatively more stable, and thus can be used for extrapolation. c_1 and c_2 for different proteins also have fairly constant values. The fluctuation of these parameters among different proteins is natural, because different proteins have distinct structures.

3.3.2 Exponential of degree-4 polynomial

When the system size is not very large, the energy distribution of one phase is not necessarily Gaussian. In this sub-section, a heuristic generalization to the two-Gaussian

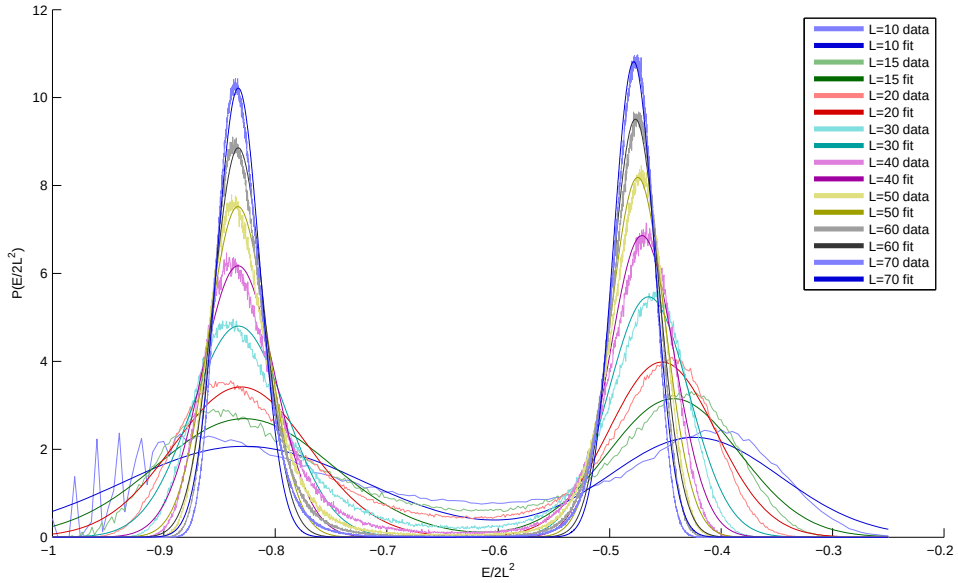

Figure 3.4: The Potts model WHAM results, and the best fit lines using the sum of two Gaussian functions

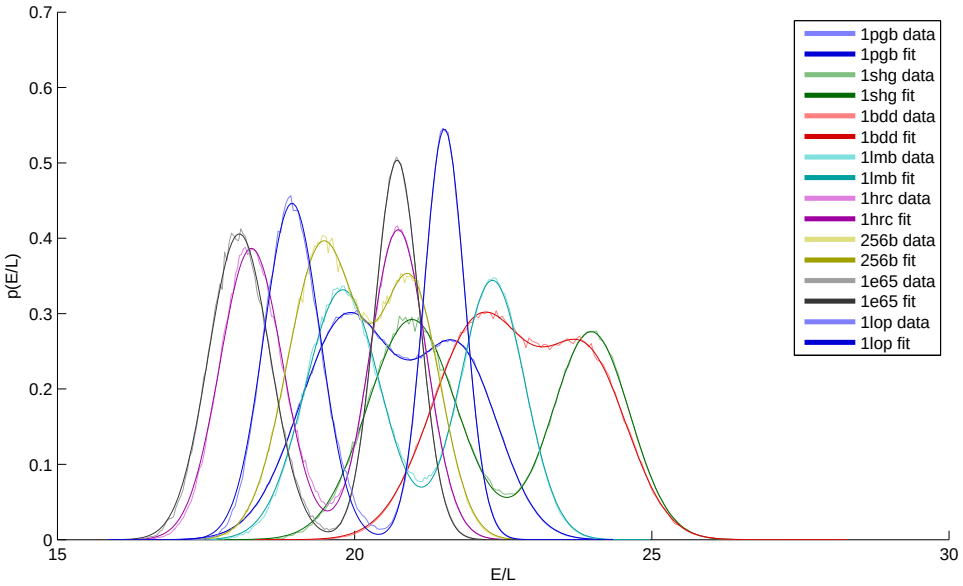

(a)

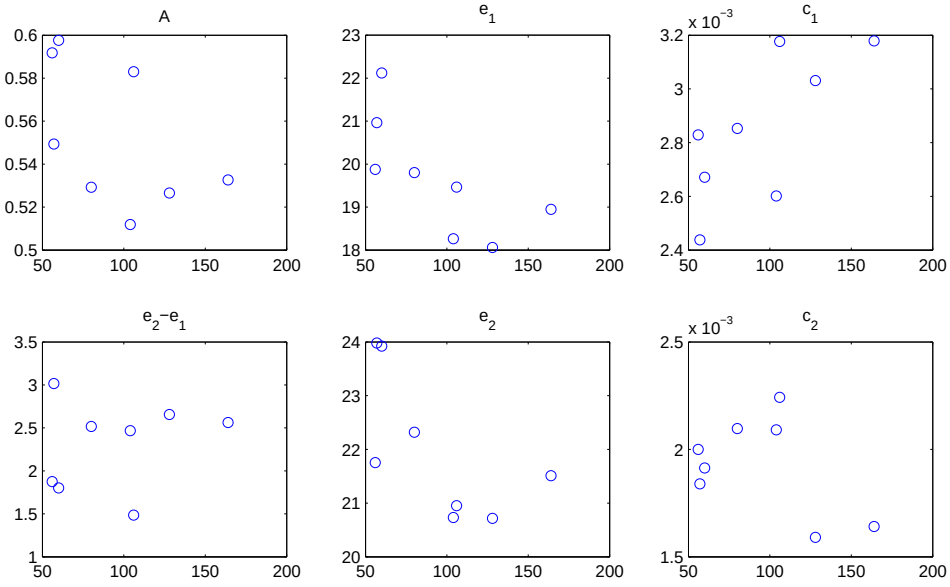

(b)

Figure 3.5: (a) The protein WHAM results, and the best fit lines using the sum of two Gaussian functions. (b) The values of the parameters of the best fit lines as functions of the length of the protein.

model, which replace the distribution of one phase by an exponential of degree-4 polynomial, is considered:

$$P_4(x + x_0) = N_4 \exp\left(-\frac{x^2}{c^2} - \frac{sx^3}{c^3} - \frac{kx^4}{c^4}\right). \tag{3.10}$$

where x_0, c, s and k are parameters, N_4 is the normalization factor, c has the same dimensionality as x, s and k are dimensionless, and they are named for their relations to the skewness and kurtosis of this distribution. The physical reason to use this functional form is the following. Value of the energy distribution function can change by several orders of magnitude from its minimum to maximum, while the free energy of each energy level, which is proportional to the logarithmic of the energy distribution function, typically changes within the same order of magnitude. For one phase, there is an energy with minimal free energy, and in this FSS model, the free energy as a function of energy is Taylor expanded around this energy up to the fourth power.

Now we apply this fitting function to the Potts model. Let $x = E/2L^2$. We assume that the energy distribution takes the form

$$P_{\text{Potts}}(x) = A_1 P_4(c_1, s_1, k_1; x + e_1) + A_2 P_4(c_2, s_2, k_2; x + e_2). \tag{3.11}$$

The fitting results are shown in Figure 3.6(a), and the values of the parameters are shown in Figure 3.6(b). It can be seen that this functional form can fit the data very well. In addition, all the parameters show smooth trends as functions of L. We can in principle fit the parameter functions with appropriate functional forms, and use them to predict the energy distribution at other system sizes. However, unlike the two-Gaussian model, in which the parameters are taken to be L-independent, it is not clear what functional forms should be used to fit the parameters $s_{1,2}$ and $k_{1,2}$ as functions of L.

3.3.3 A distribution concentrated near its lower bound

For the graph model, neither the Gaussian function nor Equation (3.10) can fit the distribution of the low temperature phase, because this distribution is concentrated around the lower bound $E = 0$. The distribution of one phase is thus assumed heuristically to take

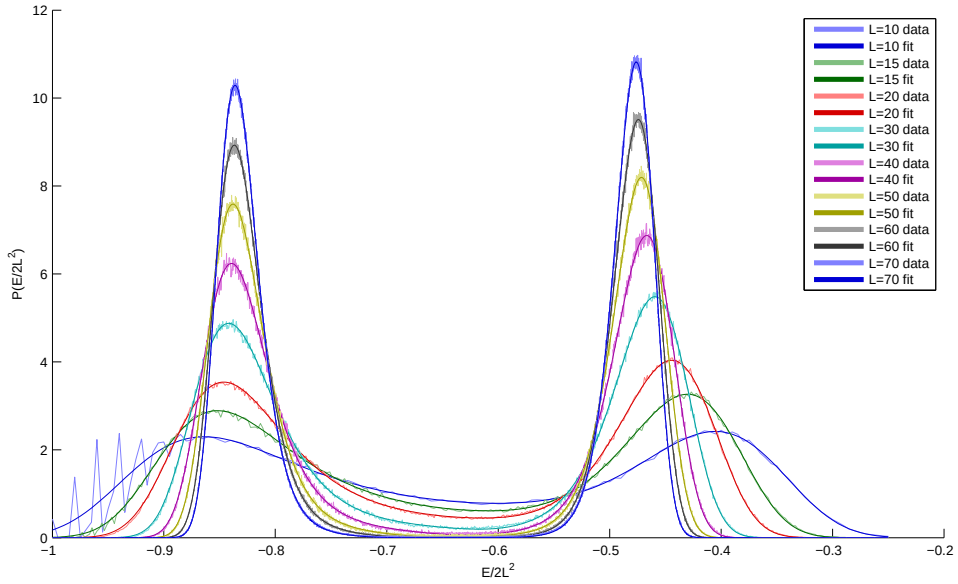

(a)

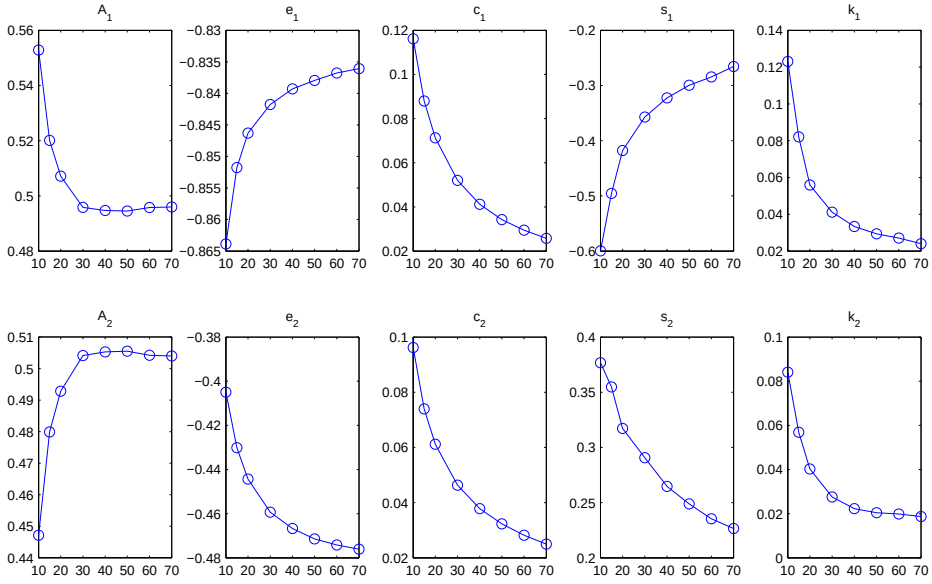

(b)

Figure 3.6: (a) The WHAM results of energy distribution of the Potts model, with $L = 10, 15, 20, 30, 40, 50, 60$ and 70, and the best fit lines using the distribution (3.11). (b) The values of the parameters of the best fit lines as functions of L.

the form

$$P_e(x) = N_e \exp\left[s \exp(-cx) - bx\right], \; x \in [0, \infty), \tag{3.12}$$

where c, b and s are parameters, and N_e is the normalization factor. The full energy distribution of graph model is fitted by the function

$$P_{\text{graph}}(x) = A_1 P_e(s_1, c_1, b_1; x) + A_2 P_e(c_2, s_2, k_2; x + e_2), \tag{3.13}$$

where $x = E/N_V$, and $A_1 + A_2 = 1$. The fitting results are shown in Figure 3.7(a), and the values of the parameters are shown in Figure 3.7(b). This FSS model can capture the shape of the energy distribution very well. However, because only three different sizes are available, additional numerical data are needed to identify the trends of the parameters as functions of N_V, and to further evaluate this FSS model.

3.3.4 A capillarity model

For a model with first-order transition, a state in the thermodynamic limit is always composed of one phase. At finite sizes, states with mixed phases can contribute to the partition function. For the phase-coexisting states, we can use the capillarity theory to analyze their effects. (See, e.g., [23, 122].)

In Monte Carlo simulations, the dynamics of a first-order phase transition can be understood as a nucleation process [23, 122]. Near the transition temperature, starting with a state composed of only one phase, the configuration contains many "bubbles", or nuclei, of the other phase. When a nucleus is small enough, due to the interface tension, the nucleus is not stable, and tends to shrink and disappear. However, with a very small probability, a nucleus can also grow large enough and overcome the free energy barrier. Thus in the rare process of one phase turning into the other phase, the intermediate states are phase-coexisting states, and the interface area between phases is suppressed by the interface tension. A typical phase-coexisting state of the Potts model with $L = 50$ is shown in Figure 3.8.

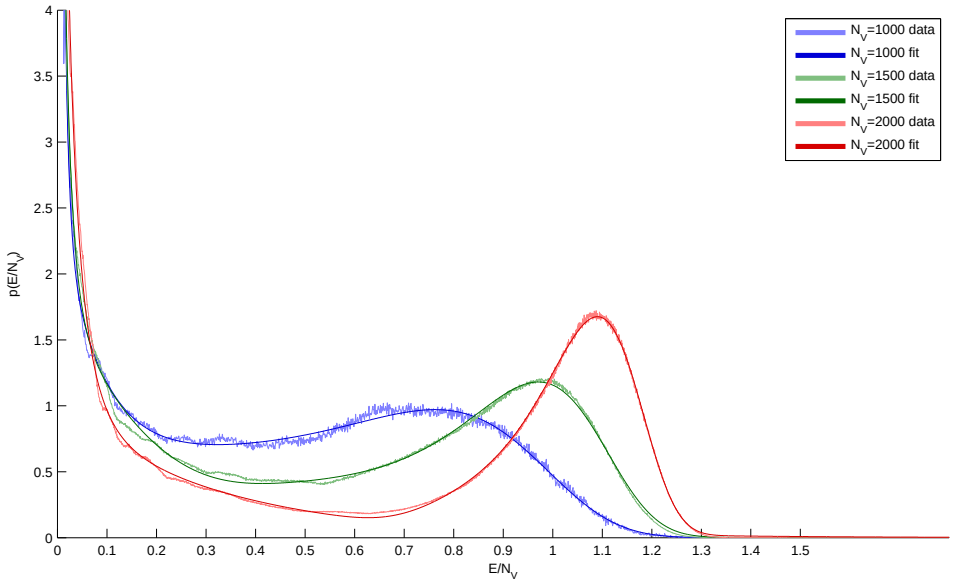

(a)

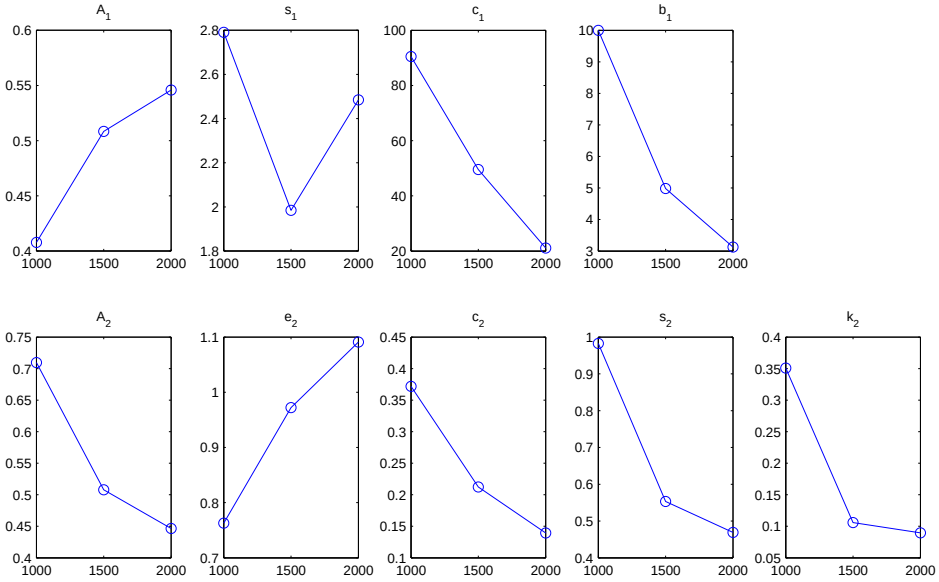

(b)

Figure 3.7: (a) The WHAM results of energy distribution of the graph model, with $N_V = 1000, 1500$ and 2000, and the best fit lines using (3.13). (b) The values of the parameters of the best fit lines as functions of N_V.

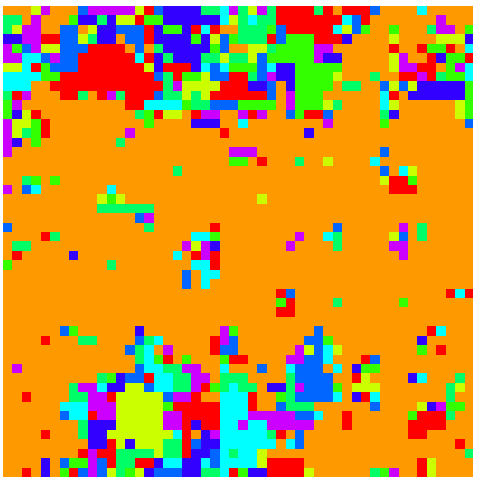

Figure 3.8: A typical phase-coexisting state of the Potts model with $L = 50$. Different spin values are denoted by different colors.

For a system of volume V, consider a phase-coexisting state which has volumes of the two phases V_1 and V_2, respectively, and the expected interface area A is determined by V_1. The entropy of the interface is ignored. Let T_c be the transition temperature in the bulk limit.

Assume first that the energy distribution of one phase is a delta function. At T_c, the energy distribution is the superposition of all possible values of V_1,

$$P(E, T_c) = \int_0^V dV_1 \; B(V_1)\delta[E - (V_1 e_1 + V_2 e_2 + A e_a)] \tag{3.14}$$

where e_1, e_2 are the energy densities of each phase, e_a is the interface tension, and

$$B(V_1) = B_0 \exp(-A(V_1) e_a / T_c). \tag{3.15}$$

This is because compared with the single-phase states, a phase-coexisting state has higher free energy due to the interface tension, and the amplitude is suppressed by the Boltzmann factor. If $e_a = 0$, $P(E, T_c)$ is flat between $V e_1$ and $V e_2$. In the limit $e_a \to \infty$, $P(E, T_c)$ is

the sum of two delta functions. If we assume the delta function is solved by $\tilde{V}(E)$, that is, $E = \tilde{V}(E)e_1 + (V - \tilde{V}(E))e_2 + A(\tilde{V}(E))e_a$, and assume there is only one solution to this equation, then (3.14) can be integrated

$$P(E, T_c) = \frac{B(\tilde{V}(E))}{\left| e_1 - e_2 + e_a \left. \frac{dA}{dV_1} \right|_{V_1 = \tilde{V}(E)} \right|}. \tag{3.16}$$

If we keep only the leading order of e_a, which is in (3.15), then $\tilde{V}(E) = \frac{Ve_2 - E}{e_2 - e_1}$, and

$$P(E, T_c) = \frac{B_0 \exp\left[-A\left(\frac{Ve_2 - E}{e_2 - e_1}\right) e_a / T_c \right]}{|e_2 - e_1|}, \quad Ve_1 \le E \le Ve_2. \tag{3.17}$$

From this expression, one can see that when V increases while $\tilde{V}(E)/V$ is fixed, A increases as $V^{(d-1)/d}$, and this distribution approaches the sum of two delta functions in the thermodynamic limit. This confirms the statement that when the system size is large enough, the contribution from the phase-coexisting states can be ignored.

Now assume that the variances of energy distribution of the two phase are $V\sigma_1^2$ and $V\sigma_2^2$, respectively. At T_c, macroscopic states with volume of one phase being any V_1 should have the same entropy. The energy distribution of such state is a Gaussian distribution with mean $(V_1 e_1 + V_2 e_2 + A e_a)$, and variance $(V_1\sigma_1^2 + (V - V_1)\sigma_2^2)$. The energy distribution (3.14) is generalized to

$$\begin{aligned} P(E, T_c) &= \int_0^V dV_1 \; B(V_1) \frac{1}{\sqrt{2\pi}\sqrt{V_1\sigma_1^2 + (V - V_1)\sigma_2^2}} \exp\left[-\frac{(E - (V_1 e_1 + V_2 e_2 + A e_a))^2}{2(V_1\sigma_1^2 + (V - V_1)\sigma_2^2)} \right] \\ &= \frac{B_0}{\sqrt{2\pi}} \int_0^V dV_1 \; \frac{1}{\sqrt{V_1\sigma_1^2 + (V - V_1)\sigma_2^2}} \exp\left[-\frac{(E - (V_1 e_1 + V_2 e_2 + A e_a))^2}{2(V_1\sigma_1^2 + (V - V_1)\sigma_2^2)} - \frac{A e_a}{T_c} \right] \end{aligned} \tag{3.18}$$

If $\sigma_1 = \sigma_2$, this integration can be performed analytically. However, in general, including the case of the Potts model, $\sigma_1 \neq \sigma_2$, and this integration can only be calculated numerically.

For the Potts model at $L = 30$, the simulation data can fitting relatively well (see Fig. 3.9), with parameters $e_1 = -1.72$, $e_2 = -0.89$, $\sigma_1 = 1.78$, $\sigma_2 = 1.53$, $e_a = 0.37$, $T_c = 1.4261$, and the area function is taken to be $A(V_1) = \min(\sqrt{V_1}, \sqrt{V - V_1})$. Compared with the two-Gaussian model, the addition of the phase-coexisting states contributes to some

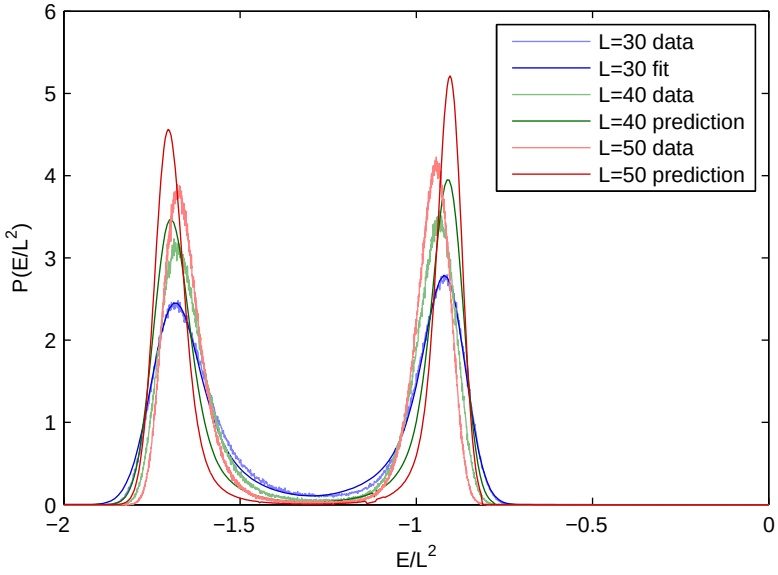

Figure 3.9: The WHAM result of the Potts model energy distribution for $L = 30, 40, 50$. For $L = 30$, the best fit line using (3.18) is shown. Then the values of the fitting parameters from $L = 30$ are used to predict the distributions for $L = 40$ and 50.

additional probability between Ve_1 and Ve_2, and can help to explain why the distribution of one phase has non-zero skewness. In the current FSS model, the values of the parameters should not scale with L. If the same parameters are used for other sizes, the predicted distributions do not fit the numerical results well (see Figure 3.9). This indicates that for the Potts model, there may be other finite size effects that should be incorporated in the FSS model.

The dependence of the interface length on the volume of one phase $A(V_1)$ was assumed to be $A(V_1) = \min(\sqrt{V_1}, \sqrt{V - V_1})$ above. The form of $A(V_1)$ can also be measured directly from the simulation as follows. For each sample of the Monte Carlo simulation of the Potts model, V_1 is measured as the volume of the largest component, where a component is a connected region with the same spin. A is measured as the length of the interface between the largest component and the rest of the system. For the same value of V_1, multiple measurements of A are averaged. The result for $L = 50$ is shown in Figure 3.10, along

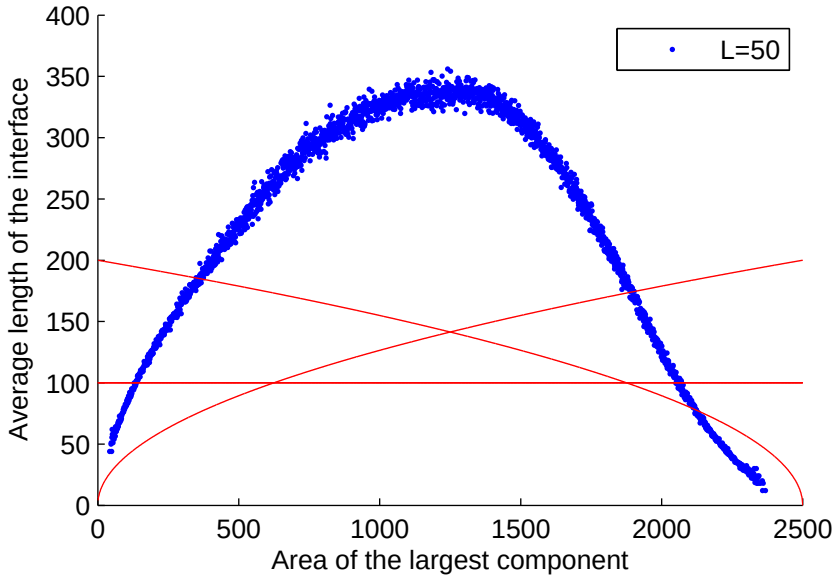

Figure 3.10: The average interface length is plotted in blue color as a function of the area of largest component. The three red curves $A = 4\sqrt{V_1}, A = 4\sqrt{V - V_1}, A = 2\sqrt{V} = 2L$ correspond to the cases with the ordered phase forming a square region, the complement of a square region, and a cylinder-shaped region.

with the three red curves $A = 4\sqrt{V_1}, A = 4\sqrt{V - V_1}, A = 2\sqrt{V} = 2L$, which correspond to the cases with the ordered phase forming a square region, the complement of a square region, and a cylinder-shaped region. For intermediate values of V_1 ($100 < V_1 < 2000$), the average of measured interface length is greater than the smallest of the three cases with regular shapes, which means that for a given V_1, the average interface length is greater than the smallest possible interface length. This phenomenon can be understood as that the interface is frustrated by the entropy associated with it (see also Figure 3.8).

3.4 Discussion

In this chapter, the Potts model, a structure-based model for protein folding, and the graph model of emergent manifold are considered, and three different fitting functions, as

well as a more physically motivated capillarity model are tested as FSS models. We found that to obtain the best fitting result, different physics models need different FSS models. Due to the limitation of available numerical results, the usefulness of these FSS model remains to be tested on larger system sizes, and on other physics models.

We note that the models in Section 3.3.2 and 3.3.4 are both generalizations of the two-Gaussian model in Section 3.3.1. For the Potts model, better fitting result are obtained with the generalized models, at the cost of using more fitting parameters. Thus it is an interesting question whether or not such generalizations actually improve the FSS model. This question can be addressed by considering a set of physics models, and check the statistical significance of the improvements of the fittings to the numerical results.

Another open question is how a different boundary condition (b.c.) can affect the finite size effects. For the Potts model, the current periodic b.c. can be changed into an open b.c., in which the spins at the boundary have no interaction with the outside, or a closed b.c., in which the spins at the boundary interact with fixed spins in the outside. Among these candidates, the periodic b.c. supposedly gives the closest results as the infinite size system. However, the periodic b.c. changes the topology of the system, which can have a significant effect when using the capillarity model. It is interesting to compare the results from different b.c.'s, and identify the differences in their finite size effects.

Bibliography

[1] S. Chen and S. S. Plotkin, "Statistical mechanics of graph models and their implications for emergent manifolds," *Phys. Rev. D 87,* **084011** (2013) , arXiv:1210.3372 [gr-qc].

[2] S. Chen, "Mapping class group and U(1) Chern-Simons theory on closed orientable surfaces," *Mod.Phys.Lett.* **A27** (2012) 1250087, arXiv:1103.2820 [hep-th].

[3] P. Erdős and A. Rényi, "On random graphs," *Publicationes Mathematicae Debrecen* **6** (1959) 290–297.

[4] G. 't Hooft, "A planar diagram theory for strong interactions," *Nucl.Phys.* **B72** (1974) 461.

[5] J. Ambjørn, J. Jurkiewicz, and R. Loll, "Emergence of a 4-D world from causal quantum gravity," *Phys.Rev.Lett.* **93** (2004) 131301, arXiv:hep-th/0404156 [hep-th].

[6] J. Ambjørn, J. Jurkiewicz, and R. Loll, "Reconstructing the universe," *Phys.Rev.* **D72** (2005) 064014, arXiv:hep-th/0505154 [hep-th].

[7] R. Albert and A.-L. Barabási, "Statistical mechanics of complex networks," *Rev. Mod. Phys.* **74** (2002) 47–97.

[8] D. S. Franzblau, "Computation of ring statistics for network models of solids," *Phys. Rev. B* **44** (Sep, 1991) 4925–4930.

[9] U. S. Bhalla and R. Iyengar, "Emergent properties of networks of biological signaling pathways," *Science* **283** no. 5400, (1999) 381–387.

[10] J. J. Hopfield, "Neural networks and physical systems with emergent collective computational abilities," *Proceedings of the National Academy of Sciences* **79** no. 8, (1982) 2554–2558, `http://www.pnas.org/content/79/8/2554.full.pdf+html`.

[11] T. Konopka, F. Markopoulou, and L. Smolin, "Quantum graphity," `arXiv:hep-th/0611197 [hep-th]`.

[12] T. Konopka, F. Markopoulou, and S. Severini, "Quantum graphity: a model of emergent locality," *Phys. Rev.* **D77** (2008) 104029, `arXiv:0801.0861 [hep-th]`.

[13] T. Konopka, "Statistical Mechanics of Graphity Models," *Phys.Rev.* **D78** (2008) 044032, `arXiv:0805.2283 [hep-th]`.

[14] A. Hamma, F. Markopoulou, S. Lloyd, F. Caravelli, S. Severini, *et al.*, "A Quantum Bose-Hubbard model with evolving graph as toy model for emergent spacetime," *Phys.Rev.* **D81** (2010) 104032, `arXiv:0911.5075 [gr-qc]`.

[15] F. Caravelli, A. Hamma, F. Markopoulou, and A. Riera, "Trapped surfaces and emergent curved space in the Bose-Hubbard model," *Phys.Rev.* **D85** (2012) 044046, `arXiv:1108.2013 [hep-th]`.

[16] F. Conrady, "Space as a low-temperature regime of graphs," *J. Statist. Phys.* **142** (2011) 898, `arXiv:1009.3195 [gr-qc]`.

[17] N. Mermin and H. Wagner, "Absence of ferromagnetism or antiferromagnetism in one-dimensional or two-dimensional isotropic Heisenberg models," *Phys.Rev.Lett.* **17** (1966) 1133–1136.

[18] P. Hohenberg, "Existence of Long-Range Order in One and Two Dimensions," *Phys.Rev.* **158** (1967) 383–386.

[19] S. R. Coleman, "There are no Goldstone bosons in two-dimensions," *Commun.Math.Phys.* **31** (1973) 259–264.

[20] A. Malnič and B. Mohar, "Generating locally cyclic triangulations of surfaces," *J. Combin. Theory Ser. B* **56** no. 2, (1992) 147–164. http://dx.doi.org/10.1016/0095-8956(92)90015-P.

[21] M. E. G. Newman and G. T. Barkema, *Monte Carlo methods in statistical physics*. Clarendon Press, Oxford, 1999.

[22] A. M. Ferrenberg and R. H. Swendsen, "New Monte Carlo technique for studying phase transitions," *Phys. Rev. Lett.* **61** (1988) 2635–2638.

[23] S. S. Plotkin and J. N. Onuchic, "Understanding protein folding with energy landscape theory i: Basic concepts," *Quart. Rev. Biophys.* **35** no. 2, (2002) 111–167.

[24] S. S. Plotkin and J. N. Onuchic, "Understanding protein folding with energy landscape theory ii: Quantitative aspects," *Quart. Rev. Biophys.* **35** no. 3, (2002) 205–286.

[25] K. Binder, "Theory of first-order phase transitions," *Reports on Progress in Physics* **50** no. 7, (1999) 783.

[26] M. Plischke and B. Bergersen, *Statistical Physics*. World Scientific, Singapore, 3rd ed., 2006.

[27] E. A. Bender and E. R. Canfield, "The asymptotic number of labeled graphs with given degree sequences," *J. Combinatorial Theory Ser. A* **24** no. 3, (1978) 296–307.

[28] R. Creswick, H. Farach, and C. Poole, *Introduction to renormalization group methods in physics*. A Wiley-Interscience publication. Wiley, 1992.

[29] L. Landau and E. Lifshitz, *Statistical physics*. Addison-Wesley series in advanced physics. Pergamon Press, 1958.

[30] D. Weingarten, "EUCLIDEAN QUANTUM GRAVITY ON A LATTICE," *Nucl.Phys.* **B210** (1982) 229.

[31] F. David, "Planar Diagrams, Two-Dimensional Lattice Gravity and Surface Models," *Nucl.Phys.* **B257** (1985) 45.

[32] J. Ambjorn, B. Durhuus, and J. Frohlich, "Diseases of Triangulated Random Surface Models, and Possible Cures," *Nucl.Phys.* **B257** (1985) 433.

[33] V. Kazakov, A. A. Migdal, and I. Kostov, "Critical Properties of Randomly Triangulated Planar Random Surfaces," *Phys.Lett.* **B157** (1985) 295–300.

[34] D. Boulatov, V. Kazakov, A. A. Migdal, and I. Kostov, "POSSIBLE TYPES OF CRITICAL BEHAVIOR AND THE MEAN SIZE OF DYNAMICALLY TRIANGULATED RANDOM SURFACES," *Phys.Lett.* **B174** (1986) 87–93.

[35] D. Johnston, "Gravity and random surfaces on the lattice: A Review," *Nucl.Phys.Proc.Suppl.* **53** (1997) 43–55, `arXiv:hep-lat/9607021 [hep-lat]`.

[36] M. J. Bowick, "Random surfaces and lattice gravity," *Nucl.Phys.Proc.Suppl.* **63** (1998) 77–88, `arXiv:hep-lat/9710005 [hep-lat]`.

[37] P. Di Francesco, P. H. Ginsparg, and J. Zinn-Justin, "2-D Gravity and random matrices," *Phys.Rept.* **254** (1995) 1–133, `arXiv:hep-th/9306153 [hep-th]`.

[38] A. M. Polyakov, "Quantum Geometry of Bosonic Strings," *Phys.Lett.* **B103** (1981) 207–210.

[39] D. Oriti, *The Group field theory approach to quantum gravity*. Cambridge University Press, 2006. `arXiv:gr-qc/0607032 [gr-qc]`.

[40] D. Oriti, "A Quantum field theory of simplicial geometry and the emergence of spacetime," *J.Phys.Conf.Ser.* **67** (2007) 012052, `arXiv:hep-th/0612301 [hep-th]`.

[41] A. Üngör, "Tiling 3D Euclidean space with acute tetrahedra," in *Proc. of the 13th Canadian Conference on Computational Geometry*, pp. 169–172. 2001.

[42] J. Q. Quach, C.-H. Su, A. M. Martin, and A. D. Greentree, "Domain structures in quantum graphity," *Phys.Rev.* **D86** (2012) 044001, arXiv:1203.5367 [gr-qc].

[43] F. Markopoulou and L. Smolin, "Disordered locality in loop quantum gravity states," *Class.Quant.Grav.* **24** (2007) 3813–3824, arXiv:gr-qc/0702044 [gr-qc].

[44] L. Pauling, "The structure and entropy of ice and of other crystals with some randomness of atomic arrangement," *J. Am. Chem. Soc.* **57** (1935) 2680–2684.

[45] P. W. Anderson, "Ordering and antiferromagnetism in ferrites," *Phys. Rev.* **102** (May, 1956) 1008–1013. http://link.aps.org/doi/10.1103/PhysRev.102.1008.

[46] S. T. Bramwell and M. J. P. Gingras, "Spin ice state in frustrated magnetic pyrochlore materials," *Science* **294** no. 5546, (2001) 1495–1501, http://www.sciencemag.org/content/294/5546/1495.full.pdf.

[47] F. Caravelli and F. Markopoulou, "Properties of Quantum Graphity at Low Temperature," *Phys.Rev.* **D84** (2011) 024002, arXiv:1008.1340 [gr-qc].

[48] J. B. Kogut, "An Introduction to Lattice Gauge Theory and Spin Systems," *Rev.Mod.Phys.* **51** (1979) 659.

[49] J. Ambjørn, J. Jurkiewicz, and Y. Watabiki, "On the fractal structure of two-dimensional quantum gravity," *Nucl.Phys.* **B454** (1995) 313–342, arXiv:hep-lat/9507014 [hep-lat].

[50] J. Ambjørn, J. Jurkiewicz, and R. Loll, "Spectral dimension of the universe," *Phys.Rev.Lett.* **95** (2005) 171301, arXiv:hep-th/0505113 [hep-th].

[51] G. Giasemidis, J. F. Wheater, and S. Zohren, "Dynamical dimensional reduction in toy models of 4D causal quantum gravity," *Phys.Rev.* **D86** (2012) 081503, arXiv:1202.2710 [hep-th].

[52] J. Ambjørn, S. Jordan, J. Jurkiewicz, and R. Loll, "A Second-order phase transition in CDT," *Phys.Rev.Lett.* **107** (2011) 211303, arXiv:1108.3932 [hep-th].

[53] R. Penrose, "Difficulties with inflationary cosmology," *Annals N.Y.Acad.Sci.* **571** (1989) 249–264.

[54] S. M. Carroll and J. Chen, "Does inflation provide natural initial conditions for the universe?," *Gen.Rel.Grav.* **37** (2005) 1671–1674, arXiv:gr-qc/0505037 [gr-qc].

[55] E. W. Dijkstra, "A note on two problems in connexion with graphs," *Numerische Mathematik* **1** (1959) 269–271. http://dx.doi.org/10.1007/BF01386390. 10.1007/BF01386390.

[56] R. W. Floyd, "Shortest path," *Commun. ACM* **5** no. 6, (June, 1962) 345.

[57] S. Warshall, "A theorem on boolean matrices," *Journal of the ACM* **9** no. 1, (1962) 11–12.

[58] A. S. Schwarz, "The Partition Function of Degenerate Quadratic Functional and Ray-Singer Invariants," *Lett.Math.Phys.* **2** (1978) 247–252.

[59] E. Witten, "Quantum field theory and the Jones polynomial," *Commun. Math. Phys.* **121** (1989) 351.

[60] M. Marino, "Chern-Simons theory and topological strings," *Rev.Mod.Phys.* **77** (2005) 675–720, arXiv:hep-th/0406005 [hep-th].

[61] G. W. Moore and N. Seiberg, "Taming the conformal zoo," *Phys.Lett.* **B220** (1989) 422.

[62] S. Elitzur, G. W. Moore, A. Schwimmer, and N. Seiberg, "Remarks on the canonical quantization of the Chern-Simons-Witten theory," *Nucl.Phys.* **B326** (1989) 108.

[63] M. Bos and V. Nair, "Coherent state quantization of Chern-Simons theory," *Int.J.Mod.Phys.* **A5** (1990) 959.

[64] M. Bañados, "Global charges in Chern-Simons field theory and the (2+1) black hole," *Phys.Rev.* **D52** (1996) 5816, arXiv:hep-th/9405171 [hep-th].

[65] E. Witten, "Analytic Continuation Of Chern-Simons Theory," arXiv:1001.2933 [hep-th].

[66] C. Nayak, S. H. Simon, A. Stern, M. Freedman, and S. Das Sarma, "Non-Abelian anyons and topological quantum computation," *Rev.Mod.Phys.* **80** (2008) 1083–1159.

[67] R. Iengo and K. Lechner, "Anyon quantum mechanics and Chern-Simons theory," *Phys.Rept.* **213** (1992) 179–269.

[68] U. H. Danielsson, M. Lundgren, and A. J. Niemi, "Gauge field theory of chirally folded homopolymers with applications to folded proteins," *Phys. Rev. E* **82** (Aug, 2010) 021910. http://link.aps.org/doi/10.1103/PhysRevE.82.021910.

[69] A. Achucarro and P. Townsend, "A Chern-Simons action for three-dimensional anti-De Sitter supergravity theories," *Phys.Lett.* **B180** (1986) 89.

[70] E. Witten, "(2+1)-dimensional gravity as an exactly soluble system," *Nucl. Phys.* **B311** (1988) 46.

[71] S. Carlip, "Quantum gravity in 2+1 dimensions: The case of a closed universe," *Living Rev. Rel.* **8** (2005) 1, arXiv:gr-qc/0409039 [gr-qc].

[72] E. Witten, "Three-dimensional gravity revisited," arXiv:0706.3359 [hep-th].

[73] S. Hawking and G. Ellis, *The Large Scale Structure of Space-Time*. Cambridge Monographs on Mathematical Physics. Cambridge University Press, 1973.

[74] G. 't Hooft and M. Veltman, "One loop divergencies in the theory of gravitation," *Annales Poincare Phys.Theor.* **A20** (1974) 69–94.

[75] C. Rovelli, "What is observable in classical and quantum gravity?," *Class.Quant.Grav.* **8** (1991) 297–316.

[76] C. Isham, "Canonical quantum gravity and the problem of time," in *Integrable systems, quantum groups, and quantum field theories*, pp. 157–287. Kluwer Academic, 1993. `arXiv:gr-qc/9210011 [gr-qc]`.

[77] H.-J. Matschull, "On the relation between (2+1) Einstein gravity and Chern-Simons theory," *Class. Quant. Grav.* **16** (1999) 2599–2609, `arXiv:gr-qc/9903040 [gr-qc]`.

[78] E. Buffenoir and K. Noui, "Unfashionable observations about three-dimensional gravity," `arXiv:gr-qc/0305079 [gr-qc]`.

[79] B. Farb and D. Margalit, *A Primer on Mapping Class Groups*. Princeton Mathematical Series. Princeton University Press, 2011.

[80] G. V. Dunne, "Aspects of Chern-Simons theory," `arXiv:hep-th/9902115 [hep-th]`. Les Houches Lectures 1998.

[81] S. S. Chern and J. Simons, "Characteristic forms and geometric invariants," *Ann. of Math. (2)* **99** (1974) 48–69.

[82] R. Dijkgraaf and E. Witten, "Topological gauge theories and group cohomology," *Commun.Math.Phys.* **129** (1990) 393.

[83] F. Warner, *Foundations of Differentiable Manifolds and Lie Groups*. Graduate Texts in Mathematics. Springer, 1971.

[84] S. Deser, R. Jackiw, and S. Templeton, "Three-Dimensional massive gauge theories," *Phys.Rev.Lett.* **48** (1982) 975–978.

[85] D. Birmingham, M. Blau, M. Rakowski, and G. Thompson, "Topological field theory," *Phys. Rept.* **209** (1991) 129–340.

[86] G. 't Hooft, "Quantization of point particles in (2+1)-dimensional gravity and space-time discreteness," *Class.Quant.Grav.* **13** (1996) 1023–1040, arXiv:gr-qc/9601014 [gr-qc].

[87] M. Banados, C. Teitelboim, and J. Zanelli, "The Black hole in three-dimensional space-time," *Phys.Rev.Lett.* **69** (1992) 1849–1851, arXiv:hep-th/9204099 [hep-th].

[88] D. Brill, "Black holes and wormholes in (2+1)-dimensions," in *Mathematical and quantum aspects of relativity and cosmology*, pp. 143–179. 1998. arXiv:gr-qc/9904083 [gr-qc].

[89] J. Louko, "Witten's 2+1 gravity on R x (Klein bottle)," *Class. Quant. Grav.* **12** (1995) 2441–2468, arXiv:gr-qc/9505026 [gr-qc].

[90] G. Rham, *Differentiable manifolds: forms, currents, harmonic forms*. Grundlehren der mathematischen Wissenschaften. Springer-Verlag, 1984.

[91] R. Bott and L. W. Tu, *Differential forms in algebraic topology*, vol. 82 of *Graduate Texts in Mathematics*. Springer-Verlag, New York, 1982.

[92] T. A. Murdoch, *Twisted calibrations and the cone over the Veronese surface*. PhD thesis, Rice University, 1988.

[93] G. T. Horowitz, "Exactly Soluble Diffeomorphism Invariant Theories," *Commun.Math.Phys.* **125** (1989) 417.

[94] C. Misner, K. Thorne, and J. Wheeler, *Gravitation: Charles W. Misner, Kip S. Thorne, John Archibald Wheeler*. Gravitation. W. H. Freeman, 1973.

[95] S. Axelrod, S. Della Pietra, and E. Witten, "Geometric quantization of Chern-Simons gauge theory," *J. Diff. Geom.* **33** (1991) 787–902.

[96] A. Y. Alekseev, H. Grosse, and V. Schomerus, "Combinatorial quantization of the Hamiltonian Chern-Simons theory," *Commun.Math.Phys.* **172** (1995) 317–358, arXiv:hep-th/9403066 [hep-th].

[97] A. Y. Alekseev, H. Grosse, and V. Schomerus, "Combinatorial quantization of the Hamiltonian Chern-Simons theory. 2.," *Commun.Math.Phys.* **174** (1995) 561–604, arXiv:hep-th/9408097 [hep-th].

[98] A. Y. Alekseev and V. Schomerus, "Representation theory of Chern-Simons observables," arXiv:q-alg/9503016 [q-alg].

[99] M. Dehn, *Papers on group theory and topology*. Springer-Verlag, New York, 1987. http://dx.doi.org/10.1007/978-1-4612-4668-8. Translated from the German and with introductions and an appendix by John Stillwell, With an appendix by Otto Schreier.

[100] D. Mumford, "Abelian quotients of the Teichmüller modular group," *J. Analyse Math.* **18** (1967) 227–244.

[101] W. B. R. Lickorish, "A finite set of generators for the homeotopy group of a 2-manifold," *Proc. Cambridge Philos. Soc.* **60** (1964) 769–778.

[102] B. Wajnryb, "A simple presentation for the mapping class group of an orientable surface," *Israel J. Math.* **45** no. 2-3, (1983) 157–174. http://dx.doi.org/10.1007/BF02774014.

[103] W. B. R. Lickorish, "Homeomorphisms of non-orientable two-manifolds," *Proc. Cambridge Philos. Soc.* **59** (1963) 307–317.

[104] D. R. J. Chillingworth, "A finite set of generators for the homeotopy group of a non-orientable surface," *Proc. Cambridge Philos. Soc.* **65** (1969) 409–430.

[105] S. Gukov, E. Martinec, G. W. Moore, and A. Strominger, "Chern-Simons gauge theory and the AdS(3) / CFT(2) correspondence," `arXiv:hep-th/0403225 [hep-th]`.

[106] C. Meusburger and B. Schroers, "Mapping class group actions in Chern-Simons theory with gauge group G x g*," *Nucl.Phys.* **B706** (2005) 569–597, `arXiv:hep-th/0312049 [hep-th]`.

[107] M. Bos and V. Nair, "U(1) Chern-Simons theory and c=1 conformal blocks," *Phys.Lett.* **B223** (1989) 61.

[108] M. Manoliu, "Abelian Chern-Simons theory," *J.Math.Phys.* **39** (1998) 170–206, `arXiv:dg-ga/9610001 [dg-ga]`.

[109] A. P. Polychronakos, "On the quantization of the coefficient of the Abelian Chern-Simons term," *Phys. Lett.* **B241** (1990) 37.

[110] P. Peldan, "Large diffeomorphisms in (2+1) quantum gravity on the torus," *Phys.Rev.* **D53** (1996) 3147–3155, `arXiv:gr-qc/9501020 [gr-qc]`.

[111] J. S. Birman and H. M. Hilden, "On the mapping class groups of closed surfaces as covering spaces," in *Advances in the theory of Riemann surfaces (Proc. Conf., Stony Brook, N.Y., 1969)*, pp. 81–115. Ann. of Math. Studies, No. 66. Princeton Univ. Press, Princeton, N.J., 1971.

[112] J. S. Birman and D. R. J. Chillingworth, "On the homeotopy group of a non-orientable surface," *Proc. Cambridge Philos. Soc.* **71** (1972) 437–448.

[113] B. Szepietowski, "A presentation for the mapping class group of a non-orientable surface from the action on the complex of curves," *Osaka J. Math.* **45** no. 2, (2008) 283–326. `http://projecteuclid.org/getRecord?id=euclid.ojm/1216151101`.

[114] B. Szepietowski, "A presentation for the mapping class group of the closed non-orientable surface of genus 4," *J. Pure Appl. Algebra* **213** no. 11, (2009) 2001–2016. http://dx.doi.org/10.1016/j.jpaa.2009.02.009.

[115] R. Potts, "Some generalized order - disorder transformations," *Proc.Cambridge Phil.Soc.* **48** (1952) 106–109.

[116] P. C. Whitford, J. K. Noel, S. Gosavi, A. Schug, K. Y. Sanbonmatsu, and J. N. Onuchic, "An all-atom structure-based potential for proteins: Bridging minimal models with all-atom empirical forcefields," *Proteins: Structure, Function, and Bioinformatics* **75** no. 2, (2009) 430–441. http://dx.doi.org/10.1002/prot.22253.

[117] J. K. Noel, P. C. Whitford, K. Y. Sanbonmatsu, and J. N. Onuchic, "Smog@ctbp: simplified deployment of structure-based models in gromacs,". http://nar.oxfordjournals.org/cgi/content/short/38/suppl_2/W657.

[118] F. Wu, "The Potts model," *Rev.Mod.Phys.* **54** (1982) 235–268.

[119] R. Baxter, "Potts model at critical temperature," *J.Phys.* **C6** (1973) L445–L448.

[120] J. Noel and J. Onuchic, "The many faces of structure-based potentials: From protein folding landscapes to structural characterization of complex biomolecules," in *Computational Modeling of Biological Systems*, N. V. Dokholyan, ed., Biological and Medical Physics, Biomedical Engineering, pp. 31–54. Springer US, 2012. http://dx.doi.org/10.1007/978-1-4614-2146-7_2.

[121] M. S. Challa, D. Landau, and K. Binder, "Finite size effects at temperature driven first order transitions," *Phys.Rev.* **B34** (1986) 1841–1852.

[122] J. Rowlinson and B. Widom, *Molecular theory of capillarity*. The international series of monographs on chemistry. Dover Publications, 2002.